Project report TTK4551

Magnus Steinstø

Design Report NTNU – Drillbotics 2021 Phase I - Cybernetics

Trondheim 15.12 2020

NTNU
Norwegian University of Science and Technology

Norwegian University of Science and Technology
Department of Geoscience and Petroleum

Design Report NTNU - Drillbotics 2021 Phase I

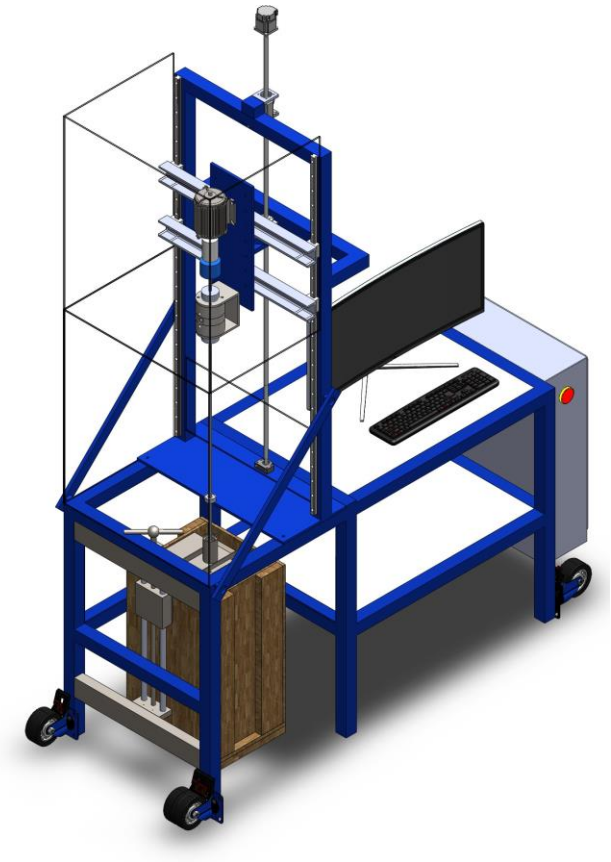

Written by:
Gaute Hånsnar
Benedicte Gjersdal
Magnus Steinstø
Trygve Mikal Viga Skretting

Date:
December 15, 2020

Preface

This report is with special permission from supervisor written in collaboration with the other members of the NTNU Drillbotics student team. The team is required to submit a Phase I report of the planned implementation to the Drillbotics committee to be accepted into Phase II of the competition. To minimize report writing in Phase I, this report is written to the specifications of the Drillbotics committee. The format of this report will therefore differ from a traditional project report.

This subject is credited 7.5 points, half the the traditional project report. The sections 5.6, 9.1,1, 9.1.3, 9.2-9.6, 10, and 11 are to be evaluated. I have also participating in writing Executive Summary, Acknowledgments, Competition Objectives, Finance, Conclusion, and Future Work. My background is a Bachelor's degree in Computer Science.

Executive Summary

The oil and gas industry is one of the leading industries for innovative solutions and recent years solutions have focused on digitization of drilling and production data. Complete automation of drilling processes has been a desired goal of many engineers. However, the technology has not achieved the attention it needs in order to convince oil companies to implement it in the their drilling operations. Petroleum students from around the world are challenged to design and build a small-scaled autonomous drilling rig in the SPE/DSATS Drillbotics competition. Fully autonomous drilling requires a sophisticated control system, where petroleum and cybernetics students must work together to overcome challenges across disciplines.

This report presents phase I of II in the Drillbotics competition. It investigates the competition guidelines and from them, the team has tried to create a concept for a mechanical drilling rig that can meet the competition objectives. Previous teams has used a Positive Displacement Motor (PDM) to achieve directional drilling. This years team will instead implement a concept similar to casing drilling, where a rotating rod inside the drill pipe drives the drill bit. Investigation of the new change of concept with respect to the mechanical design and materials required has been done. The team designed a mechanically robust drilling system by changing the material alloy of the drill pipe from Aluminium 6061-T6 to Aluminium 7075-T6. This enables the rig system to drill a maximum inclination of 30 °and azimuth of 15 °without damaging the drilling equipment. A gearbox and motor will allow for azimuth change by rotating the drill pipe. The hydraulic system was modified such that circulation of fluid downhole is possible with a rotating rod inside the drill pipe. A new Bottom Hole Assembly (BHA) was designed to transmit rotational torque from the rotating rod to a drilling bit with an outer diameter of 1.5 in. The drilling rig has undergone many modifications to fit the new drilling concept and the changes made will allow for a mechanically stable and predictable system, such that the control system can be optimized accordingly. The developed software does a cost-analysis for each target, continuously optimizing the well path in order to reach the target in the best possible manner. The system takes into consideration drilling parameters such as; time, Rate of Penetration (ROP), Weight On Bit (WOB), bending, buckling, twisting, tension and compression of drilling equipment.

In the next phase, the main focus will be to build the rig with all its modifications and perform extensive test drilling to see whether the rig require further modifications. Furthermore, control algorithms for best well path will be created and modified based on data obtained during test-drilling. After investigating possible drilling concepts to achieve the competition requirements, the team concludes with a design that uses a rotating shaft to drill the desired well path.

Acknowledgments

This report is submitted as a specialization project, a part of a Master of Science degree in Petroleum Engineering and Industrial Cybernetics at the Norwegian University of Science and Technology (NTNU) in Trondheim. We would like to thank our supervisors Alexey Pavlov, Lars Struen Imsland, Sigbjørn Sangesland, and Tor Berge Gjersvik for allowing us to work on this project within our field of interest. Your knowledge, guidance, ideas, and support has been invaluable while working on this project and report.

We would also like to thank our lab engineers Noralf Vedvik and Steffen Wærnes Moen for contributing with technical help, ideas, support, interpretation of experimental data, and general guidance. Your knowledge and experience has helped us with numerous challenges throughout the first phase of this project.

Furthermore, we want to call attention to IGP and ITK at NTNU for allowing us to work together and execute such a comprehensive project across the disciplines of drilling and cybernetics. We strongly believe that the collaboration is of great benefit to both parties.

We want to recognise the Drilling System Automation Technical Section (DSATS) of Society of Petroleum Engineers (SPE) for providing a competition and platform that allows us to work with technical and practical challenges that are highly relevant for our education.

Lastly, we thank the people behind the BRU21-program (Better Resource Utilization in the 21st century) for funding our project so far and thus showing their devotion to further development of technology and innovative solutions within drilling automation.

Contents

Abbreviations

ADC Analog-To-Digital Converter.

API American Petroleum Institute.

API Application Programming Interface.

BHA Bottom Hole Assembly.

CIP Common Industrial Protocol.

CL Course Length.

DAQ Data acquisition.

DD Directional Drilling.

DLS Dogleg Severity.

DOF Degree Of Freedom.

DOP Depth of Cut.

DP Drill Pipe.

DSATS Drilling System Automation Technical Section.

DTH Down the Hole.

DTM Downhole Turbine Motor.

EMM Electrical Miniature Motor.

ERD Extended Reach Drilling.

GPM Gallons Per Minute.

GUI Graphical User Interface.

HMI Human Machine Interface.

HSE Health, Safety & Environment.

IGP Department of Geoscience and Petroleum.

IMU Inertial Measurement Unit.

IP Internet Protocol.

ITK Department of Engineering Cybernetics.

KOP Kick-Off Point.

MD Measured Depth.

MPC Model Predictive Control.

NCS Norwegian Continental Shelf.

NTNU Norwegian University of Science and Technology.

OD Outer Diameter.

ODE Ordinary Differential Equation.

OSI Open Systems Interconnection.

PCB Printed Circuit Board.

PD Proportional-Derivative.

PDC Polycrystalline Diamond Compact.

PDM Positive Displacement Motor.

PI Proportional-Integral.

PID Proportional-Integral-Derivative.

PLC Programmable Logic Controller.

POI Point of Interest.

PPE Personal Protective Equipment.

PPG pounds-per-gallon.

RC Radius of Curvature.

ROP Rate of Penetration.

RPM Revolutions Per Minute.

RSS Rotary Steerable System.

SF Safety Factor.

SPE Society of Petroleum Engineers.

TCP Transmission Control Protocol.

TD Top Drive.

TVD True Vertical Depth.

UDP User Datagram Protocol.

USB Universal Serial Bus.

USD United States dollar.

WOB Weight On Bit.

List of Figures

List of Tables

1 Introduction

For decades, complete automation of drilling processes has been a common desired goal of many engineers. However, until recently the technology has not received the attention it needs in order to convince oil companies to implement it in the their drilling operations. Systems that are operated without human intervention has become more prevalent in our everyday life. Advancements such as self-driving cars has proven that autonomous technology has reached a level of maturity where autonomous systems are capable of advanced decision making in safety critical systems. Implementing autonomous systems in the oil an gas industry can potentially minimize risk of injuries and system failure, improve execution quality, and increase capacity and efficiency [58].

Drilling operations has since the beginning been dirty and dangerous workplaces. Mishandling of petroleum equipment can have fatal consequences. Autonomous drilling minimizes the risk of human errors related to drilling operations, and simultaneously increase productivity, quality and reduce costs. The petroleum industry has for a long time been regarded as a conservative industry, but has started to see the benefits of automation. The ultimate goal to reduce time, cost and risk would be to have a fully autonomous, remotely operated drilling rig that can operate consistently and in a safe manner.

The *Drilling System Automation Technical Section (DSATS)* was established in 2008 by *Society of Petroleum Engineers (SPE)* to make progress in terms of drilling automation. *"The purpose of DSATS is to accelerate the development and implementation of systems automation in the well drilling industry by supporting initiatives which communicate the technology, recommend best practices, standardize nomenclature and help define the value of drilling systems automation"*. The *DSATS* committee established the Drillbotics competition in 2014 as an initiative to achieve this [10]. The Drillbotics team from Norwegian University of Science and Technology (NTNU) will in 2021 be its fifth consecutive team to participate in the competition. Because the two previous years met some challenges on their path to the competition, it is desirable to regain the great results from 2017 and 2018. To achieve this, this years team will aim to develop a new design that is mechanically robust and more predictable to create a safer and more efficient working environment.

The team has decided to change the mechanical concept and has made major progress on the required rig modifications. This reports presents the current setup, planned implementation, design considerations, comparisons, and discussion around different design alternatives.

1.1 Purpose and Focus of This Report

This report is a part of a specialization project at Norwegian University of Science and Technology (NTNU) and aims to give a better understanding of the autonomous systems applied in drilling operations. The report presents the work behind creation of a downscaled drilling rig and investigates how autonomous technology can be implemented in order to drill to target without any human intervention. It is based upon the research and work done by the previous and current Drillbotics team from Norwegian University of Science and Technology (NTNU) in 2020-2021 and is the report of phase I of II in the Drilbotics Competition. The overall goal in this specialization is for the team to investigate and implement the technology needed to automatize a small drilling rig and later theoretically transfer the concept to a full scale operation.

- **Chapter 2** describes the background and purpose of this report.
- **Chapter 3** describes the organizational work done by the group and discusses the drillbotics teams structure and challenges.
- **Chapter 4** describes safety moments and hazards during the drillbotics project and challenges related to Health, Safety and Environment (HSE).
- **Chapter 5** gives an overview of the drillbotics competition's objective and guidelines.
- **Chapter 6** gives a theoretical background for directional drilling, bit steering, drill string mechanics, drilling circulation and an introduction to various controllers and filters.
- **Chapter 7** presents the previous and current design parameters, limits and uncertainties related to well trajectory, drilling equipment and hydraulics and introduces the competitions requirements.
- **Chapter 8** gives an overview of the mechanical design, therein rig system, drill string design, downhole power design.
- **Chapter 9** gives an overview of the hydraulic system.
- **Chapter 10** presents the electrical system and instrumentation.
- **Chapter 11** describes the autonomous system and its control design.
- **Chapter 12** presents the digital twin of the rig.
- **Chapter 13** examines the risk related to the project and provides an analysis of such.
- **Chapter 14** presents the teams budget and finance.
- **Chapter 15** will present a conclusion for the objective of this report.
- **Chapter 16** will present future work.

2 Organization

The Drillbotics competition is a project that requires teamwork and collaboration across disciplines to a large extent. The Drillbotics committee advice to gather a team of students from different disciplines to solve engineering challenges towards a goal set by requirements related to the competition. Because the project is complex and time-consuming, it will require a well-structured and organized team with good planning and scheduling. This section cover the team members from Norwegian University of Science and Technology (NTNU) in the 2021 Drillbotics competition, presenting delegation of roles and responsibility, as well as the chosen project management approach and strategy.

2.1 Team

The 2021 NTNU Drillbotics team consist of four members, three from the Department of Geoscience and Petroleum (IGP) and one from Department of Engineering Cybernetics (ITK), all depicted in Figure 2.1. In addition to the students, the team is supported by five supervisors; four from IGP and one from ITK, respectively. Two laboratory engineers support the team with technical challenges that may occur. Figure 2.2 illustrates an organizational chart of the team.

Figure 2.1: 2021 NTNU Drillbotics© Team.

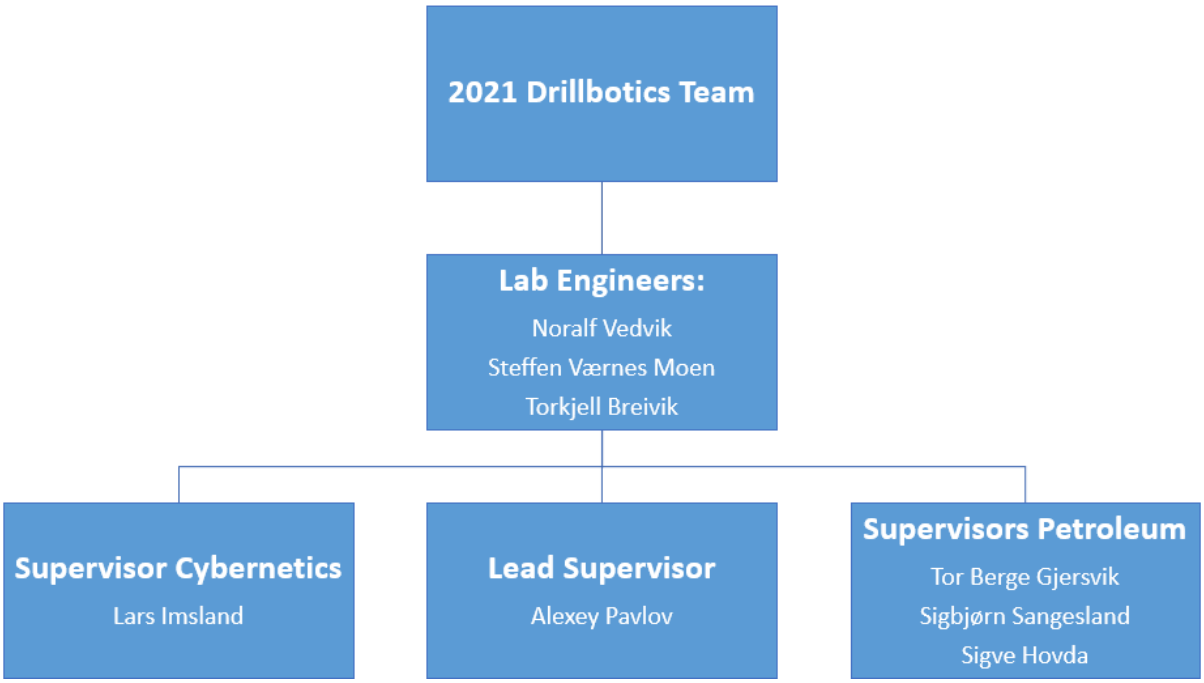

Figure 2.2: Team system for the 2021 NTNU Drillbotics© Team.

2.2 Roles

Specific roles and areas of responsibility for the project was assigned to different team members to ensure an efficient workflow throughout the project. This is important to establish early because this years team was not able to recruit five members. The team quickly gathered to brainstorm the 2021 Drillbotics© competition [52] as soon as the team members were presented and the semester had begun. The team mapped the required areas of expertise required to succeed in the challenge by discussing their relevant experience, background and interests. By doing this the team had the best possible pre-requisites to assign tasks and areas of responsibility to people with the best expertise and knowledge of the subject. Although roles were assigned to each member, problems were discussed in plenary and all the challenges were solved with close collaboration between the team members, as well as the supportive members. The team roles are presented in Figure 2.3.

The role of the supervisory team will guide and give feedback during the project. To ensure continuous information flow and close collaboration, the team has set up a meeting schedule of every two weeks with everyone in the hierarchy described in Figure 2.2. The lab engineers are based in the same building and floor as the Drillbotics team, and serve as the closest discussion partner within lab work and experience from previous years.

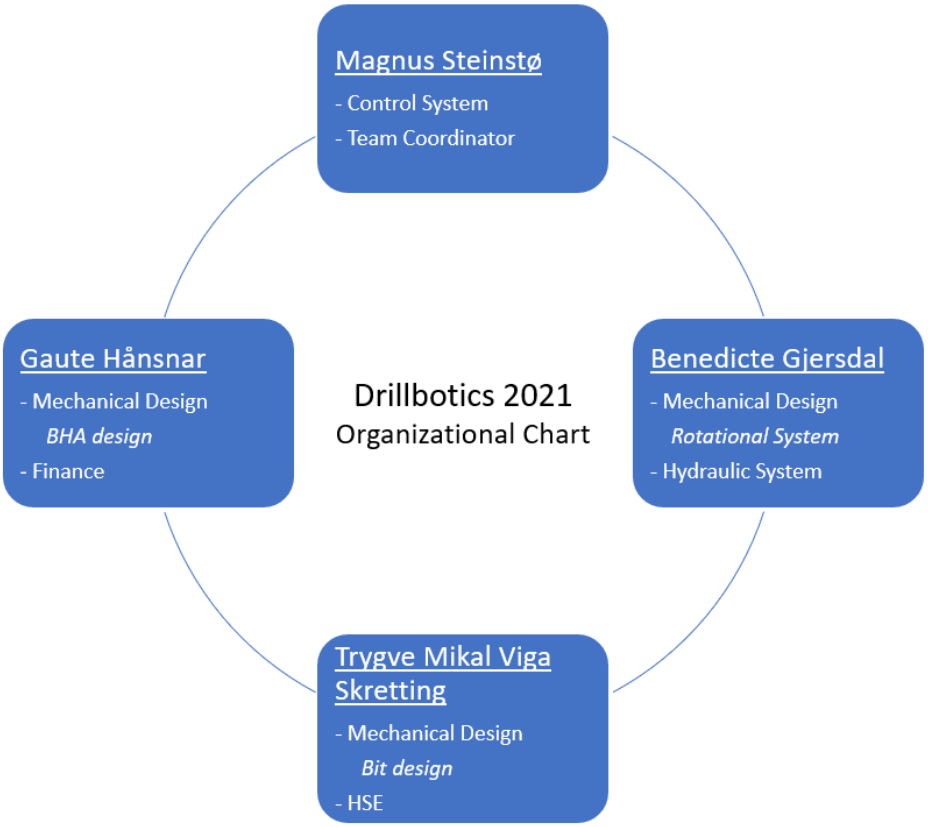

Figure 2.3: Student team organization chart.

2.3 Project Management

The team set up a precise work strategy in order to work according to planned schedule over time. The teams expectations and ground rules in the project were presented at the first meeting with the supervisors. Afterwards, the team had a new meeting where expectations and guidelines where discussed between the different members. This was done to avoid time consuming misunderstandings within the team. Figure 2.4 illustrates the Kanban-structure providing each member a understanding of what is being done by at any time. This made it easy keep track of what has been done and what is left to be done. Weekly meetings held on Mondays and Fridays presented the work done and focused on updating the Kanban.

A shared office was quickly established close to the partners involved in the project. This office made room for low-threshold day-to-day discussions and collaboration. Based on previous experience with project management in other projects, the team decided to use Microsoft Teams as a platform for storing and sharing documents. Data from Kanban and budget and scripts are kept in the Teams-channel. To work efficiently with the report, Overleaf were used to make it possible for everyone to work in the document simultaneously.

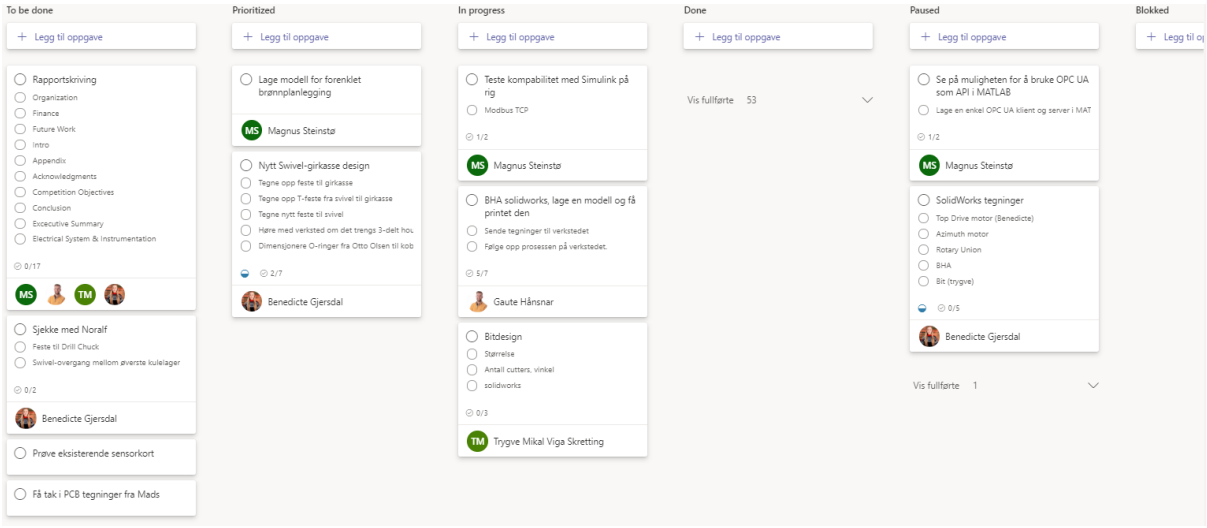

Figure 2.4: Kanban-structure.

3 Health, Safety and Environment (HSE)

The top priority for this project is to ensure that the work done in relation to the Drillbotics competition is performed in a safe manner. The team shall avoid endangering the people involved and minimize environmental exposures. The project HSE is based on HSE regulations at PTS (Petroleum Technical Center) at NTNU with advisories specifically related to this project. The team has investigated the general mindset of HSE in the petroleum industry on the Norwegian Continental Shelf (NCS).

The mechanical drilling rig in the Drillbotics project is greatly down-scaled set aside to the drilling rigs in the industry. Although the risk, safety hazards and consequences are smaller in this project, they are still present and must therefore not be ignored. The team aims to implement similar HSE regulations as found in the Norwegian petroleum industry such that every operation and rig component shall be designed and implemented with its primary focus on HSE.

All team members are responsible to ensure that everyone involved in the project is familiar with the HSE rules and follow them correctly at all times. This is especially relevant for use of proper Personal Protective Equipment (PPE) in the different scenarios that can be encountered. This is achieved with a mandatory HSE course taken by each team member before project start. After the HSE course, the team members perform a safety walk-through in the workshop with trained personnel. These pro-active exercises will ensure that the team members have understood how to handle environmental waste, use the correct PPE, how to react in the event of an emergency and other local rules and recommendations for the workshop.

Potential risks are important to establish early in the project to avoid any dangerous situa-

tion. Equation 3.1 defines risk as a function of probability and consequence. For example, the probability for a fire to occur may be unlikely but because the consequences can be severe this is an important risk to consider.

$$Risk = Probability \cdot Consequence \tag{3.1}$$

Figure 3.1 presents the risk assessment performed for health, environment, material assets and reputation related to the project. The ”X” marks the evaluated level of risk the team would encounter during the project. All categories are placed within the green field because the potential risks are low.

Figure 3.1: Risk assessment of the Drillbotics Project

3.1 Safety Hazards

To sustain a good HSE standard during the project, it is important to be aware of the hazards present present during different operations and at all times. The team must identify all possible hazards involved when starting a new task. A new potential hazard this year is the risk of getting infected with the corona virus. In the following section, hazards related to this project are presented.

- **Infection hazards** are related to situations eith a risk of getting infected with the Corona virus. Although the corona virus is the most important virus to mitigate, a bonus is that the measures will help promote good hygiene and possibly mitigate the spread of other seasonal viruses. An infection would result in a pause in the project work flow due to quarantine-regulations. Although the student can work from home, he/she might not be in shape to work with the project. Also, should the students get quarantined, they would not have access to the physical rig. The team members could infect other people affiliated with the project and university, thus increasing the risk hazard.

- **Hazardous energy** generated by electrical and hydraulic power can be present when the rig is in operation mode. To ensure that personnel are not exposed to uncontrolled hazardous energy, it is important that the equipment is properly installed, designed and

maintained. Consequences of not following operating procedures could be cutting, electrical shock and other types of lacerations. Additionally, it can potentially lead to damage on the rig equipment.

- **Machine hazards** related to mooving parts of the rig are relevant and potential risk of endangering team members. Moving parts on the rig are the drill string and the top assembly. Machine defect could lead to personnel getting stuck, pinching, cutting and crushing.

- **Chemical hazards** are not used in this project. However, there will be a potential health risk present related to the cement used for making rock samples for test drilling. The cement cuttings are flushed out of the drilled rock sample and insufficient washing could lead to cuttings remaining on the floor. This will eventually dry out and be exposed to unaware personnel potentially whom might kick up dust and thus inhaled. This results in a potentially increase risk for future lung diseases for the personnel involved.

- **Ergonomic hazards** is related to injuries such as back problems, muscle strains and shoulder injuries as a result form pushing, pulling and heavy lifting in an non-ideal body positions or doing the same task repetitively.

3.2 Protective Measures and Mitigation

To ensure that is the primary priority for the Drillbotics project, the team will implement protective measures to mitigate the presented potential hazards. All team members will have a stop work authority such that if a team member encounters an unsafe situation, the work can and shall be stopped. The work will not continue before the hazard is handled.

The team will use necessary PPE such as safety goggles and additional PPE if it is stated on the PPE board in the workshop. For mixing cement, all team members shall wear a dust mask for the intended use. Additional PPE could be a helmet, protection gloves and safety shoes. The team members will also ensure that there is no loose clothes or hair. Furthermore, the team will establish protective measures for the rig. Figure 3.2 illustrates the Drillbotics rig with a protection glass in front of the rock sample, the drill string and the top assembly. This will ensure that none of the team members are exposed to moving parts, rock cuttings and drilling fluid when the rig is in operational mode. There is also an emergency button to stop an unwanted situation. The button will break the electrical circuit to all rig components and the operation will cease immediately. The team ensures that there is always one person close to the button while operating the rig.

Operating limits for the rig indicates that pressure inside the drill pipe should be kept below the burst pressure to avoid complications while drilling. Another aspect of drilling safety that is

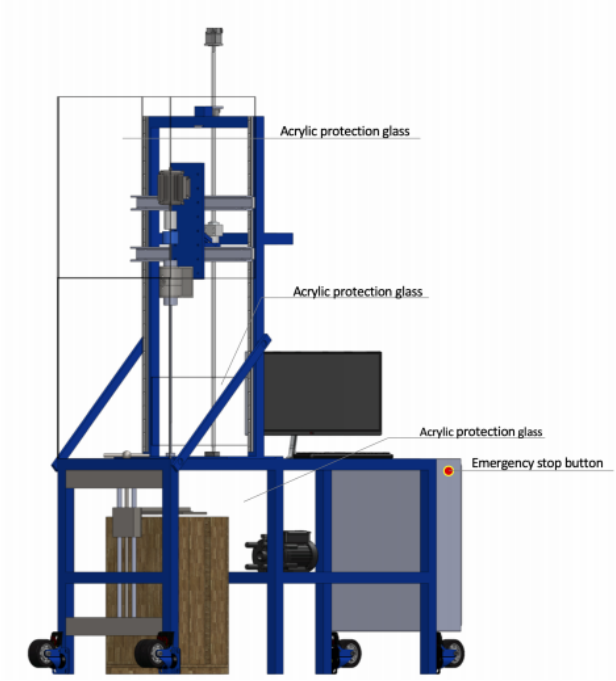

Figure 3.2: Protective measures on rig in operating mode [5]

considered is the vibrations and pipe stresses in the system. They will be kept at a level where there is minimal risk of twist-off or buckling of the aluminum rod or the drill pipe.

The rig consist of a complex electrical equipment system in which can be considered as a potential fire hazard. Protective measures to mitigate this hazard is to know where the location of fire extinguishers and fire hoses. The team must also have understanding of the different type of fire extinguishers and how to act if a fire should arise. Because the electrical equipment is quite complex, modifications will only be done by qualified personnel.

Furthermore, the team have considered ergonomic hazards when handling heavy rock samples. The risk will be reduced by using a jack trolley when moving samples. It will be necessary perform some tuning when placing the rock sample on the floor to ensure that the rock is horizontally w.r.t. to the rig, not the floor. The team have considered making smaller rock samples because those previously drilled weighs approximately 180 kg (397 lbs). Operations performed with the rock sample also involves a risk of pinching hands and feet. It will be necessary to use appropriate PPE such as proper gloves and footwear. Lastly, to avoid the chemical related to cementing, the area will be washed thoroughly and assured that there is minimum cuttings remaining around the rig.

3.3 Corona Virus

A new hazard to this years project is the corona virus. The team has designed the infection control with inspiration from helsenorge.no. This is Norway's official information page about the corona virus. The main takeaways from this page are as following [28]:

- If you are ill, stay at home.
- Avoid coughing or sneezing directly onto others.
- Keep a distance of at least one metre to others.
- Cough / sneeze into a paper tissue that you then dispose of. You should then wash your hands.
- Cough / sneeze into the crook of your elbow if you do not have tissues available to avoid spreading droplets into the air.
- Wash hands frequently and thoroughly with soap and luke-warm water, especially when you have been in contact with other people.
- You can also use an alcohol-based disinfectant if soap and water is not available.
- Find alternatives to shaking hands and hugging.

The group will follow these guidelines strictly. To avoid the use of different PPE, each team member will be assigned personal PPE equipment. Staying at home in case of any symptoms is the most important measure to minimize the risk of infection for all team members. There is a low threshold for working from home. The team members shall correct each other if recommended social distancing is not complied.

4 Competition Objectives

Drillbotics is an international drilling competition arranged by the Drilling System Automation Technical Section (DSATS). The focus of the 2021 Drillbotics competition is to simulate a real directional drilling operation in lab-scale. The team will receive a rock sample and shall drill and reach three pre-selected targets.. This must be done with an autonomous system. The Kick of Point (KOP) shall find place after a 4 inch deep, 1.5 inch wide vertical pilot hole has been drilled on the upper face of the provided rock sample, located at the center of the sample. Dimensions of the main drilling components are given in section 4

Part	**Dimensions[in]**	**Material**	**Additional Comments**
Drill bit	1.5 (OD)	Steel	Provided by DSATS
Drill pipe	0.375 (OD)	Aluminium	Can be provided by DSATS
Rock Sample	12W x 24L x 24H	Sandstone	UCS provided in spring 2021

The main challenges are:

- Designing a BHA to obtain the desired inclination by choosing correct angle on the bent sub.
- Choose and design a new drilling concept that can reach all three targets accurately.
- Implement a sensor sub for closed-loop control of the drilling rig.
- Choosing drilling material to withstand the forces acting on the drill string to prevent plastic deformation of the system.
- Estimate the current bit position throughout the drilling operation.
- Generate a reference well path based on the 3 provided targets.
- Autonomously follow the pre-planned reference well path inside the rock and intersect targets with minimal deviation.

The complete version of the guidelines for the Drillbotics Competition can be found at: `https://drillbotics.com/`

5 Theoretical Background

Theoretical background related to this years competition will be covered in this section to build a foundation for further discussion and proposal of the final design.

Disclaimer: The contents of this section will be partially similar to the similar section from last years report [5] because the goals of the competition are the same.

5.1 Directional Drilling

The concept of directional drilling (DD) was introduced to the Drillbotics competition in 2019. In previous years, change in inclination has been the only requirement. The competition held in 2021 presents a novel challenge ; the team is required to adjust both inclination and azimuth simultaneously. The following sections presents and examine the additional research of the the applications and theory of DD necessary to choose the best possible well path.

5.1.1 Applications of Directional Drilling

Arguments for applying DD varies with both the access and restrictions related to reservoir location in a field. A particular desired well paths and depletion patterns can also affect application of DD in a drilling project. Some applications of DD are [3]:

- Geo-steering.
- Drilling multiple wells from a single location.
- Drilling multiple wells from the same wellbore, also called multi-lateral wells.
- Bypassing challenging formations and geological structures, e.g. salt domes and faults.
- Accessing reservoirs below urban areas or lakes.
- Correcting unwanted deviations in the well path.
- Increase depletion area, because vertical permeability and drainage area often increase with horizontal patterns vs. vertical.

5.1.2 Well Path

As illustrated in Figure 5.1, the team has categorized the different well paths into three main types. The proposed design for this years drilling rig will be based on a type III well. However, because the well path on competition day is unknown, the rig shall be capable to drill all mentioned types.

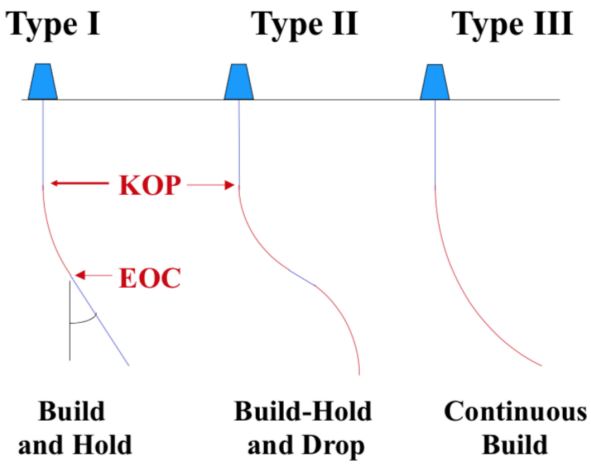

Figure 5.1: Types of well paths. [4].

At the day of competition, the competing teams will be given a set of X/Y/Z coordinates where the objective is to reach these targets as accurately as possible. The competition score is based on evaluation criteria target such as e.g. accuracy and time. To achieve an accurate well path that reaches the desired target, a control system that can understand and control both inclination and azimuth must be implemented. To better understand inclination and azimuth, the expressions are defined below.

- Inclination is irrespective of the compass direction and is the deviation from the vertical at a certain point. More specifically it is the angle between a vertical line and a tangent to the well path.

- Azimuth is the compass direction of a directional survey, more specifically the angle between the well path and North axis measured clockwise from North in the plane view.[3]

Well location and change in drilling direction are measured with reference to a known fixed point located on the drilling rig. The fixed point will have the coordinates $\{X, Y, Z\} = \{0, 0, 0\}$ which in field terminology corresponds to $\{0°$North, $0°$East, 0 m TVD$\}$. Well paths are developed from a reference point to the desired target(s) and all operations are initiated with vertical drilling until reaching a formation strong enough to handle the extra strain from building a deviated well. The point where building inclination starts at a measured depth is called the Kick-Off Point (KOP). Building a change in compass direction is called turn rate. The calculated well path is created in a 3D plot and the curve corresponding to the well path cannot be composed into inclination and azimuth separately because of turning and building. To present the well path without producing inaccurate coordinates, it is given in dogleg angle (ϕ) or Dogleg Severity (DLS). DLS $[°/m]$ is calculated using the following equation:

$$DLS = \frac{\phi}{CL} \tag{5.1}$$

Where $CL[m]$ is the course length and $\phi[^\circ]$ is the dogleg angle. The dogleg angle can be attained by using one out of many possible survey calculation methods.

5.1.3 Survey Calculation Methods

Survey calculation methods predict the wellbore position relative to the surface [3]. Accepted methods are:

- Balanced tangential
- Minimum curvature
- Tangential method
- Average Angle
- Radius of curvature

For simplicity, the *radius of curvature* method will be used in this project. This method is based on the assumption that the curve between two points is estimated by the curve of a cylinder. The radius of the cylinder can then be expressed as:

$$\begin{aligned} \frac{I_2 - I_1}{360} &= \frac{CL}{2\pi RC} \\ RC &= \frac{180CL}{\pi(I_2 - I_1)} \end{aligned} \tag{5.2}$$

Where I_2 and I_1 are the angles at two survey points. An equation for CL can be found from Equation 5.2.

$$CL = \frac{RC\pi(I_2 - I_1)}{180} \tag{5.3}$$

Radius of Curvature (RC) [m] is calculated separately for azimuth and inclination angle.

$$\begin{aligned} RC_A &= \frac{(180)(30)}{\pi B}, \\ RC_I &= \frac{(180)(30)}{\pi T} \end{aligned} \tag{5.4}$$

Where B is build-up rate and T is turn rate. Relevant parameters for creating a well path such as inclination, azimuth and dogleg angle (ϕ), are illustrated in Figure 5.2.

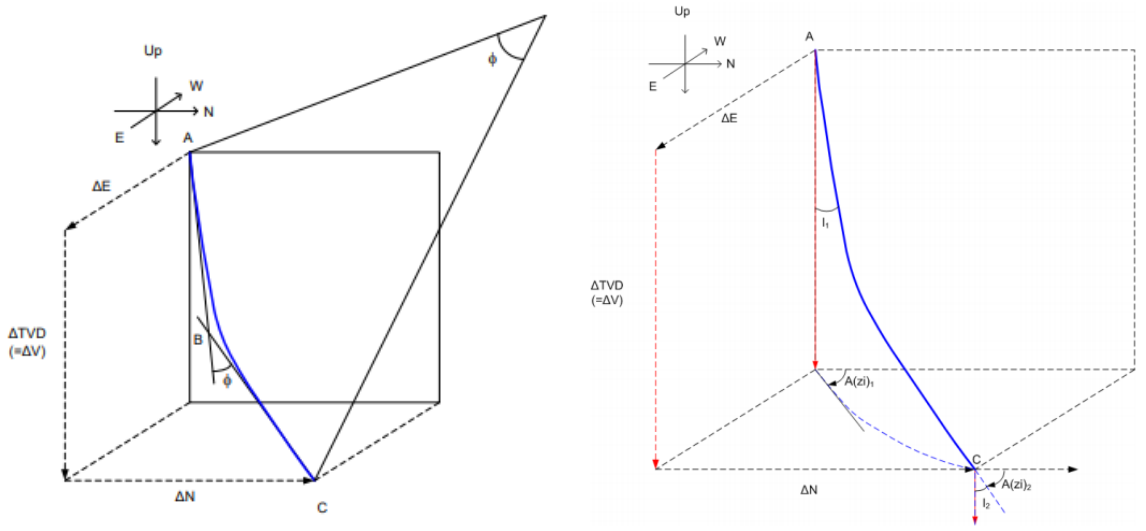

(a) Dogleg Angle (ϕ)

(b) Inclination (I) and Azimuth (A)

Figure 5.2: Relevant parameters for development of a well path [3].

5.2 Bottom Hole Assembly (BHA)

The design of the Bottom Hole Assembly (BHA) is one of the most critical factors as to whether the proposed solution is mechanically sustainable or not. This section will cover the basics for further discussion and theory that the final proposed design is based upon.

5.2.1 Directional Steering

The BHA design affects the trajectory of the wellbore, hence obtaining directional control to match planned trajectory is a important part of the BHA design. Direction is usually acquired using one of the following BHAs [3]:

- Traditional assemblies
- Steerable motor assemblies
- Rotary Steerable System (RSS)

Generally, traditional assemblies use a bent sub in combination with a straight motor. This would mean that the drill string does provide rotation to the drill bit and is thus dependent on a mud motor to cut the formation rock. This restriction limits the ability of the assemblies to create curvature and are only applicable in cases with larger hole sizes [21].

The ability to control direction changed significantly with steerable motor assemblies. Steerable motor assemblies consists of a mud motor with bent sub or bent housing. Compared to the traditional assemblies, the steerable motor assemblies are more versatile and sustainable with its ability to kick off and build angle, drill tangent sections and provide accurate directional

control. When drilling challenging formations, this technology is often applied to increase the drilling performance.

Rotary Steerable System (RSS) is considered a novel technology within directional control and is usually preferred among operators because is possesses the ability to rotate and steer the drilling bit simultaneously. However, RSS is complex and expensive, and can lead to the solution not being economically feasible. The RSS can be divided into two concepts; push the bit and point the bit, both discussed in further detail in section 5.2.6.

5.2.1.1 Dogleg Severity Based on BHA Configuration

Equation 5.1 is a method to calculate the DLS. Another alternative method is to calculate DLS based on BHA configurations [3]:

$$DLS = \frac{2\theta}{L_1 + L_2} \tag{5.5}$$

Where $\theta[^\circ]$ is the bit tilt, $L_1[m]$ is the distance from the upper stabilizer to the bend and $L_2[m]$ is the distance from the bend to the bit. Figure 5.3 illustrate the parameters.

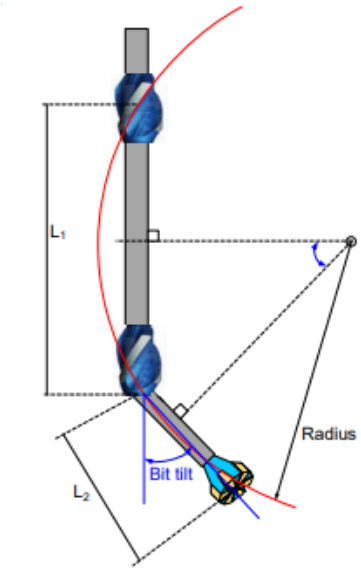

Figure 5.3: Dogleg Severity parameters based on BHA configurations [3].

5.2.2 Positive Displacement Motor (PDM)

As mentioned previously in this section, a steerable motor assembly consists of a bent housing or bent sub and a mud motor. Two variations of mud motors are common in steerable motor assemblies; Positive Displacement Motor (PDM) and Downhole Turbine Motor (DTM). Out of these, the PDMs are most commonly used.

A standard PDM is made up of three components, respectively a power section, an adjustable bend, and a bearing section as shown in Figure 5.4.

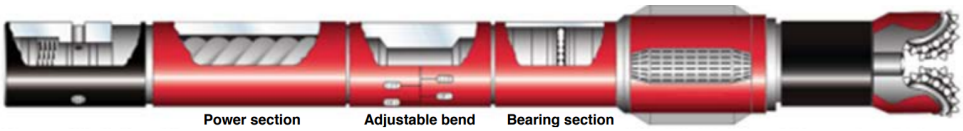

Figure 5.4: Components in a standard PDM assembly [3].

5.2.2.1 Power Section

The power section of a PDM is based on the Moineau principle to transfer hydraulic energy into mechanical energy for a driveshaft to rotate. This driveshaft is connected to the bit, hence the bit Revolutions Per Minute (RPM) will be dependent on the motor performance and configuration. The power section in simply made up of two components, a rotor and a stator. These components are quite similar, but difference in number of lobes as shown in Figure 5.6 where the rotor has one less lobe than the stator. The Moineau principle states that the helical rotor rotates eccentrically when mud flows over the cross-section of the PDM, given that the stator has more lobes than the rotor [3] (See Figure 5.5).

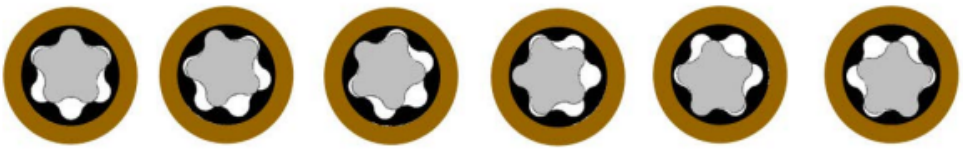

Figure 5.5: Horizontal cross-section of PDM at different depths [3].

The total number of lobes and the relationship of lobes between the rotor and the stator affects the RPM and torque. Figure 5.6 illustrates how these parameters change with lobe configuration.

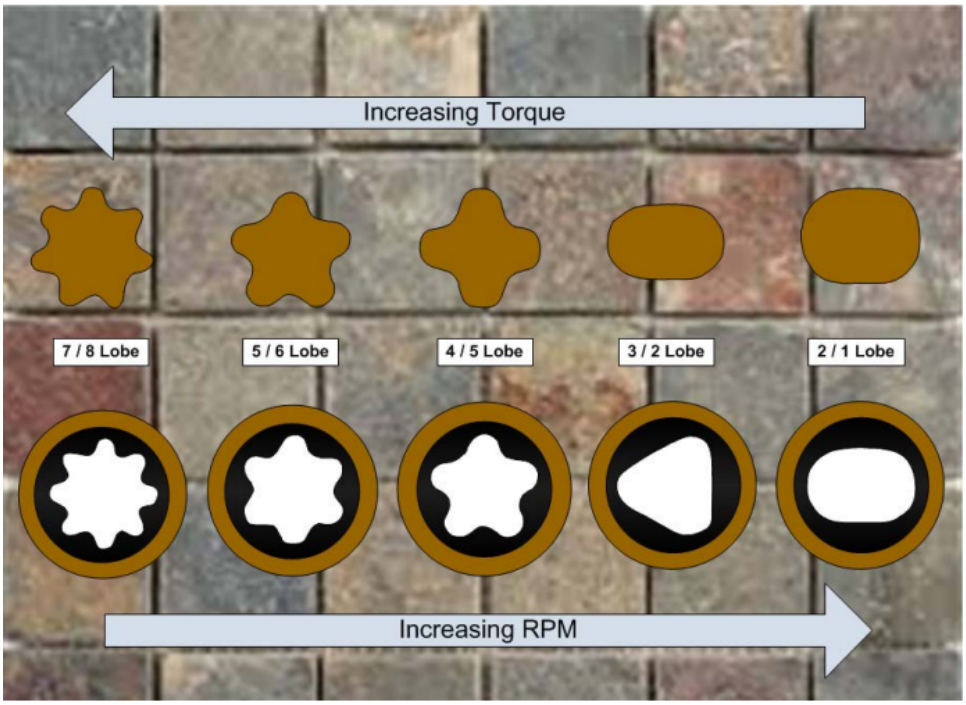

Figure 5.6: Relationship between lobe configuration and Torque RPM [3].

5.2.3 Bent Housing

The bit tilt illustrated in Figure 5.3 is accomplished using a bent housing. There are two possible solutions for bent housing; adjustable angle or fixed angle. A fixed angle bent sub, illustrated in Figure 5.7, is made of steel in a fixed bit tilt.

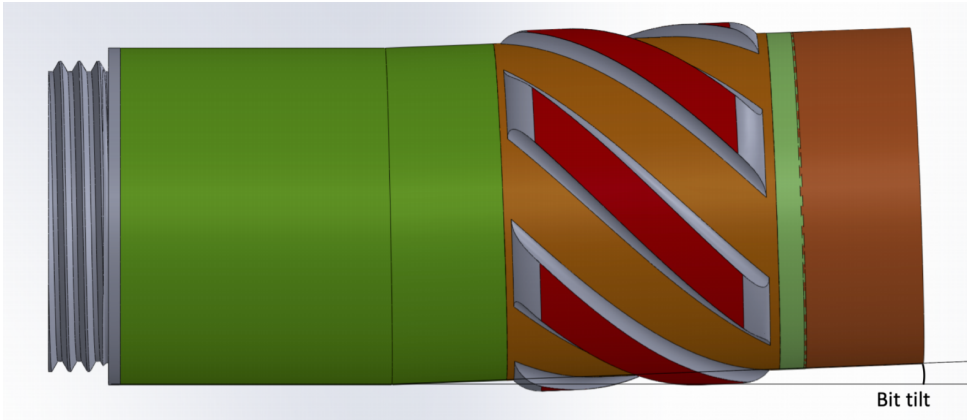

Figure 5.7: Fixed bent sub.

Surface adjustable bent sub consist of a double pin, lock housing, adjusting sleeve and offset housing. Figure 5.8 illustrates the angle adjusting sequence, performed as described:

1. Uncrew the lock housing and disengage the sleeve from its gear teeth.

2. Adjust the preferred angel.

3. Tighten the lock housing to detain the wanted angle.

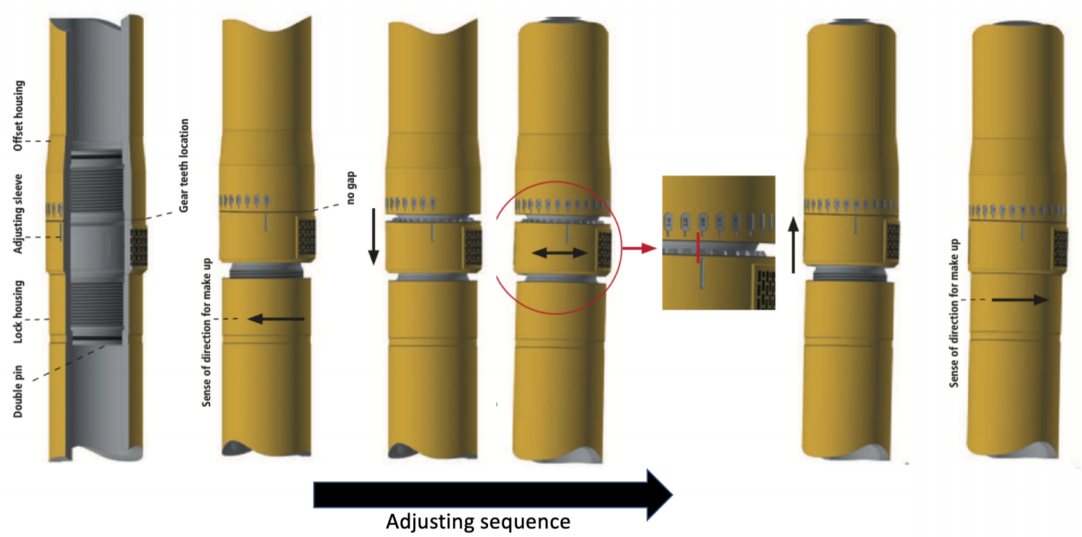

Figure 5.8: Adjustable bent sub.[19]

5.2.4 Transmission Section

Concentric rotation is generated from eccentric rotation through the transmission section. The torque and RPM from the power section is transmitted to the bearing section. There are two methods of doing this; flexible rod and universal joints [3]. Although lateral bending is limited, flexible rods are preferred in the industry because it does not require lubrication and and maintenance costs are usually low. Figure 5.9 illustrated methods of using flexible rod and universal joints.

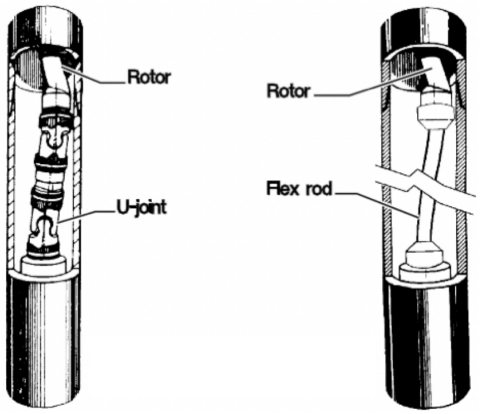

Figure 5.9: Transmission joints; universal joint and flexible joint respectively [3].

5.2.5 Bearing Section

The bearing section that transmit torque and RPM to the drill bit from the transmission shaft also acts as radial and axial support in the drilling system. Normally, the system supporting on and off bottom load and hydraulic thrust consist of three sets of bearing, two radial and one axial bearing.

Figure 5.10 illustrates how fluid flow through the drive shaft. Some of the fluid will divert into the bearings and thus cool and lubricate them. The flow diverted through the bearings generates hydraulic thrust downwards to increase the bearings lifetime this must be balanced with the upwards thrust from the Weight On Bit (WOB). [24].

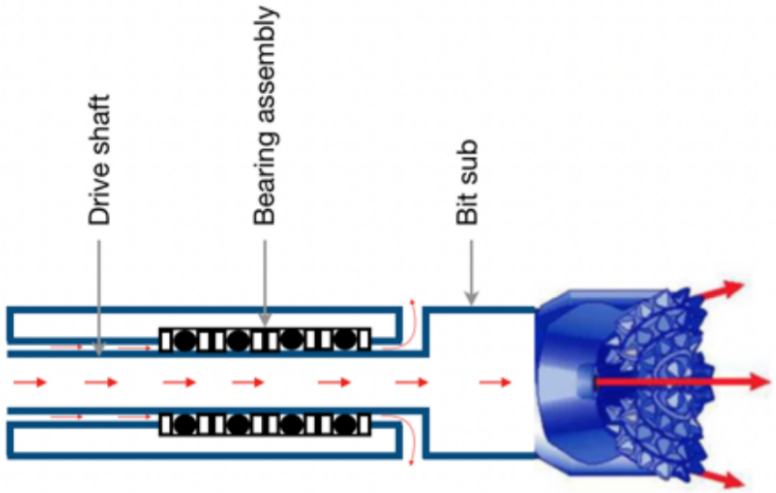

Figure 5.10: Bearing section showing flow paths in red [5].

5.2.6 Rotary Steerable System (RSS)

The rotary steerable system is a relatively new technology that improves directional drilling by solving the challenges related to steerable motors and conventional rotary assemblies. The RSS's improves penetration rate by allowing for continuous drill string rotation while steering the bit. Other beneficial aspects ofthe RSSs are improved hole quality, lower torque and drag and better hole cleaning. To provide directional control, this system utilizes a three-point contact principle, respectively the bit, a near-bit stabilizer and upper stabilizer. The two methods of RSS are:

- **Push the bit.** Motorized pads are mounted on the outer part of the middle geometric contact. The pads are activated by drilling fluid and pressed against the borehole wall to build direction.
- **Point the bit.** Motorized mechanism points the bit in desired direction. This is unlike the mud motor that has to manually orient the drill string. The general concept is the same; bit have an offset from its center axis.

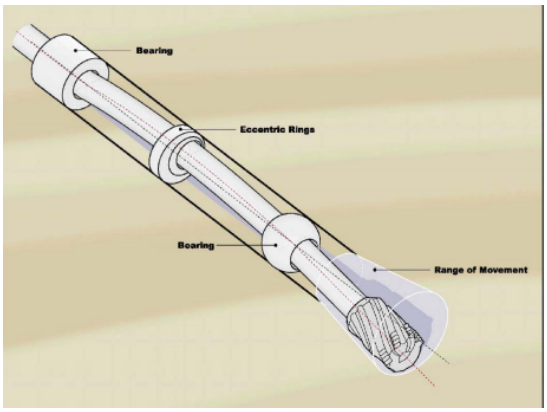

(a) Point the bit.

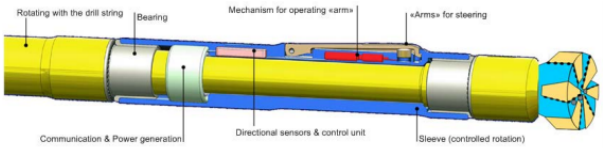

(b) Push the bit.

Figure 5.11: The two methods of RSS [3].

RSS provides constant drilling parameters, which results in more efficient control and management of the weight transfers and vibrations issues. With decreased tortuosity, the well path tends to be smoother. Although the advantages with RSS are many, the technology is complex and expensive both mechanically and electronically. As a result, the usage is limited to complex operations such as Extended Reach Drilling (ERD) or complex profiles for designer wells.

5.3 Drill String Mechanics

Awareness of mechanical limits during drilling is critical in order to prevent drill string failure. This section presents some foreseen challenges encountered during drilling operations and formulas associated with them.

5.3.1 Buckling

Buckling of drill string appear in two stages, sinusoidal and helical [8]. The first stage, sinusoidal buckling, occurs when compressive loads in the drilling system increase. In such scenarios, the string will resemble a sinus wave or a two-dimensional waveform. This results in the drill string winding back and forth against the wellbore. When additional compressive load is applied to the string, the deformation will enter the second stage known as helical buckling. The string will move along the wellbore in a helix shape. Maintaining constant WOB will thus require more axial load because the contact area between drill string and borehole wall increases and will further increase the drag. Figure 5.12 illustrates the two stages of buckling.

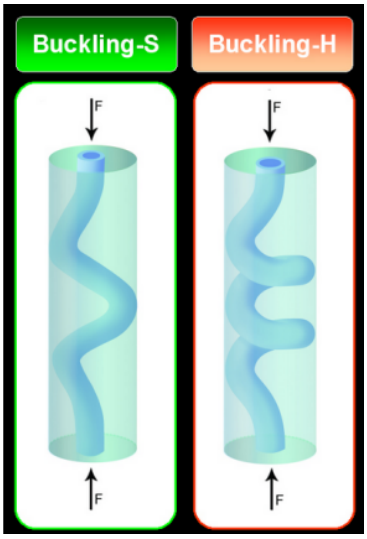

Figure 5.12: Illustration of first and second stage of buckling respectively [55].

The drilling string will buckle in the event of an axial compressive force exceeding its critical value. From Euler's column formula for long columns[17], the critical buckling limit can be predicted:

$$\sigma_{cr} = \frac{F_{cr}}{A} = \frac{\pi^2 E}{\left(K\frac{L}{r_g}\right)^2} \tag{5.6}$$

Where $\sigma_{cr}[Pa]$ is the critical buckling load, $E[Pa]$ is the modulus of elasticity, $L[m]$ is the unsupported pipe length and radius of gyration is given by $r_g[m]$. K is the effective length factor

determined by end condition of the column, which can be seen in Table 5.1.

The radius of gyration, representing the distance from a centroid at which all of the area could be concentrated without affecting the moment of inertia [18]:

$$r_g = \sqrt{\frac{I}{A}} \tag{5.7}$$

$$I = \frac{\pi}{64}(OD^4 - ID^4) \tag{5.8}$$

Where $I[m^4]$ is the second moment of area for a pipe, $A[m^2]$ is the cross-sectional area of the pipe and $OD[m]$ and $ID[m]$ is the outer and inner diameter of the pipe respectively.

Table 5.1: Effective Length Factor,K, for different end conditions [17]

End condition	**Pinned-pinned**	**Fixed-fixed**	**Fixed-pinned**	**Fixed-free**
Illustrations				
Theoretical K	1	0.5	$1/\sqrt{2}$	2
Recommended K	1	0.9	0.9	2.1

The relation L/r_g in Equation 5.6 is referred to as slenderness ratio, R_s:

$$R_s = \frac{L}{r_g} \tag{5.9}$$

The slenderness ratio increases with the length of the column, and longer columns are therefore more susceptible to buckling.
Equation 5.6 is valid for long columns while intermediate columns are calculated with Johnson formula [17], where $\sigma_{ys}[Pa]$ is the material yield strength:

$$\sigma_{cr} = \sigma_{ys} - \left(\frac{\sigma_{ys}KL}{2\pi r}\right)^2\left(\frac{1}{E}\right), \quad \frac{L}{r_g} \leq \left(\frac{L}{r_g}\right)_{cr} \tag{5.10}$$

The critical slenderness ratio is the decisive factor to whether or not the Euler's or Johnson's formula can be used to predict buckling limit for a given column with certain end conditions. Critical slenderness ratio is calculated as follows:

$$\left(\frac{L}{r_g}\right)_{cr} = \sqrt{\frac{2\pi^2 E}{K^2 \sigma_{ys}}} \tag{5.11}$$

From the critical compression load estimated with Equation 5.6 or Equation 5.10, maximum WOB can easily be estimated:

$$F_{max\ WOB} = \sigma_{cr} A \tag{5.12}$$

5.3.2 Burst

Burst of pipe can occur as a result of the internal pressure exceeding the strength of the pipe. For a long time, Barlow's equation has been used as standard for burst calculations in the industry. However, the equation is proven to be too conservative for thick-walled pipes [1]. The American Petroleum Institute (API) burst-pressure equation (Equation 5.13) is based on Barlow's equation, but takes into account the uncertainties concerning wall thickness by adding a reduction factor of 0.875 [2].

$$P_{burst} = 2\frac{0.875\sigma_{ys} t}{OD\ SF} \tag{5.13}$$

Where $t[m]$ is the material thickness and SF is a safety factor, equals to 3 and 2 when drilling and tripping respectively.

5.3.3 Pipe Twist-Off

Induced shear stress caused by a high torque, may exceed shear strength of the pipe and cause the pipe to twist off. Because twist-off is a result of the applied torque, it will be a limiting factor for torque allowance on the drill pipe. Maximum allowable torque is defined by Equation 5.14 assuming thin wall, constant $\tau(r)$ and mean radius [55]:

$$T_{max} = \tau_{max} \frac{\pi}{16}\big(OD^2 - ID^2\big)\big(OD + ID\big) \tag{5.14}$$

Further on, τ_{max} is found using the Von-Mises criterion with the assumptions that $\sigma_{23} = \sigma_{31} = 0$ and $\sigma_{12} = \tau_{max}$:

$$\tau_{max} = \sqrt{\frac{2\sigma_{ys}^2 - [(\sigma_z - \sigma_\theta)^2 + (\sigma_\theta - \sigma_r)^2 + (\sigma_r - \sigma_z)^2]}{6}} \tag{5.15}$$

Equation 5.16 and 5.17 are used to calculate radial and angular stresses [33]. They indicate that the internal pressure is the only cause for radial and angular stresses. The total axial stress on the drill string is a sum of axial stresses from bending, pressure and WOB, and can be predicted with Equation 5.18, 5.19 and 5.20.

$$\sigma_r = \frac{\left(\frac{ID}{OD}\right)^2 - \left(\frac{ID}{2r}\right)^2}{1 - \left(\frac{ID}{OD}\right)^2} p \tag{5.16}$$

$$\sigma_\theta = \frac{\left(\frac{ID}{OD}\right)^2 + \left(\frac{ID}{2r}\right)^2}{1 - \left(\frac{ID}{OD}\right)^2} p \tag{5.17}$$

$$\sigma_z^p = \frac{\left(\frac{ID}{OD}\right)^2}{1 - \left(\frac{ID}{OD}\right)^2} p \tag{5.18}$$

Where $r[m]$ is the distance from center of pipe to Point of Interest (POI).

$$\sigma_z^{WOB} = \frac{WOB}{A_{cs}} \tag{5.19}$$

5.3.4 Pipe Bending

Bending stress is the axial stress induced by the drill pipe. For a beam, bending stress is given by Equation 5.20. The equation is valid under the assumption that the cross-section perpendicular to the neutral axis of the beam remains constant [33]. A pipe will be thicker where it is in compression and thinner on the stretch side when bent [7].

$$\sigma_z^b = \frac{E}{RC} r \tag{5.20}$$

5.3.5 Stresses in Rod

Induced shear stress will be a limiting factor for torque allowance on the rod. For a solid, cylindrical shaft, the shear stress is defined by Equation 5.21 [35]:

$$\tau_s = \frac{M_s}{W_p}; \quad W_p = \frac{\pi}{16} d^3 \tag{5.21}$$

Where M_s is the applied torque, W_p is the polar moment of inertia and *d* is the diameter of the rod.

A rotating rod that is bent and exeriencing axial stress and the bending stress for a solid, cylin-

drical shaft is given by Equation 5.22 [35]:

$$\sigma_b = \frac{M_b}{W_x}; \quad W_x = \frac{\pi}{32} d^3 \tag{5.22}$$

Where M_b is the applied torque and W_x is the second moment of area.

Equation 5.23 describes the comparative stress, σ_c, which is the effective stress when both axial stress and shear stress is induced on the rotating rod simultaneously [35]. This stress will be the overall limiting factor for the rod.

$$\sigma_c = \sqrt{\sigma_b^2 + 3\tau_s^2} \tag{5.23}$$

Where σ_c is the comparative stress, σ_b is the bending stress, and τ_s is the shear stress.

5.3.6 Fatigue

Fatigue is one of the most common and expensive failures during drilling. Repeated stress applied to the drill string can create micro-cracks in the drill pipe and can with time develop into macro-cracks. This cyclic stress in combination with corrosion will shorten the expected lifetime of a drill string significantly.

Normally, fatigue occurs when the drill string rotates while being axially curved. The curved section will experience one stress cycle per revolution [8]. The cyclic stress relates to the bending stress generated from the curvature because the amplitude of stress is proportional to the degree of curvature.

Bending stress that is predicted with Equation 5.20, will represents the cyclic stress. The relationships shown in this equation indicated that the bending stress will increase with increasing Outer Diameter (OD). To minimize fatigue damage in wells with large DLS, smaller OD drill string might be preferable.

The fatigue limit of a certain material is indicated by its correlating S-N (stress-cycle) curve. The limit is found where bending stress is equal to endurance stress limit in the fatigue (S-N) curve. This is because the drill string is not limited to a number of rotations, hence the bending stress should not exceed the endurance stress limit. If a material reaches its plastic regime because of too high appliance of stress, fewer stress cycles are needed to break the material.

5.4 Drill bit

To achieve efficient drilling and accurate steerability, a custom drill bit design will be advantageous. In order to design a proper bit, there are many parameters that affect bit properties that has to be introduced. These will be covered in this section.

There are two main types of drill bits; Roller cone bits, and fixed-cutter bits.
Fixed-cutter bits consists of a fixed cutter blade with sharp ”teeth” as an integral part of the body. The drill bit body, also called ”matrix body”, consists either of steel or infiltrated Tungsten carbide - a chemical compound containing equal parts of tungsten and carbon atoms [62].

General Electric invented the first fixed cutter bits in 1955 as an application to electrical motors. 15 years later, in 1970, fixed cutter bits were applied in petroleum drilling operations. The three main types of fixed cutter bits are: natural diamond, fishtail and PDC bits. The most popular drill bit in the Norwegian oils and gas sector are the PDC bits. On the PDC bit, the tooth is called a cutter and consists of a bonded layer of poly-crystalline or tungsten carbide. The cutters are divided into inner and outer rows on the bit. The inner rows take up two-thirds of the bit radius while the rest consist of the drill bits outer rows. The main components of the fixed cutter bits are: cone, nose, taper, shoulder and gauge, all are illustrated in Figure 5.13 [59].

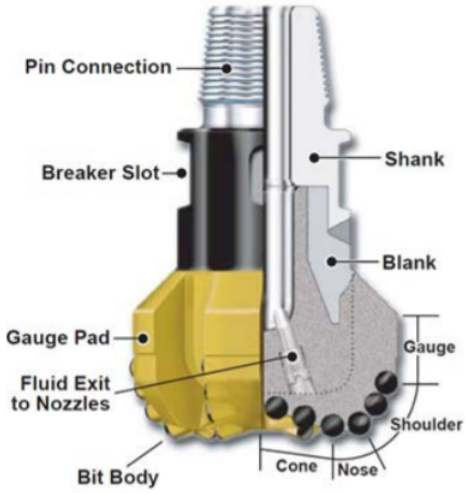

Figure 5.13: Overview of fixed cutter bit [59].

Unlike the roller cone bits, the PDC bit will remove rock by inducing shear stress failure on the rock. PDC bits require less WOB than roller cone bits because the energy needed to reach plastic limit for rupture by shear stress is less than the limit for compressive stress. Figure 5.14 shows why this is a positive feature. The need for less WOB is beneficial for the drill string

[59].

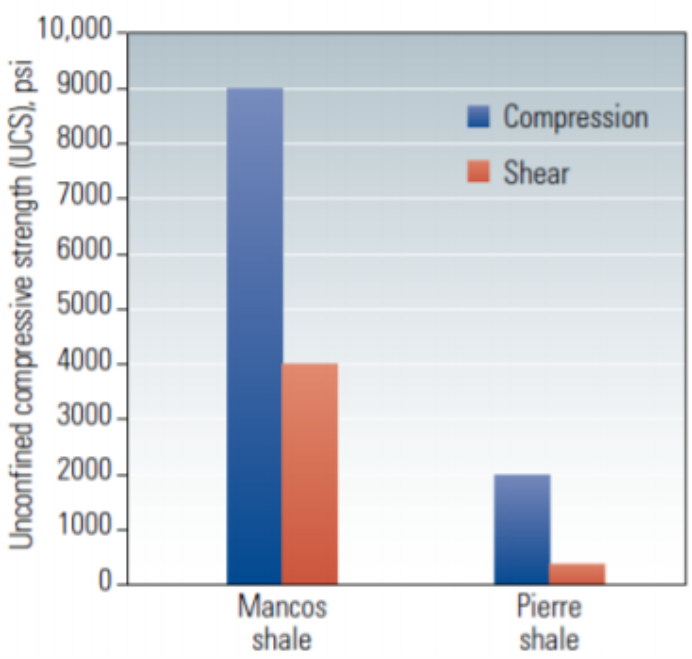

Figure 5.14: Energy required to fail (drill) two different formations [59].

5.4.1 Bit profile

The cone angle and overall bit profile are important bit properties. Figure 5.15 illustrates deep ($\approx 90°$), medium($\approx 120°$ - $140°$) and shallow($\approx 150°$) cone angles from a side view. A deep cone angle will promote high bit stability because there will be cuttings inside the inner rows shaped like a cylindrical cone centreing the bit. It also gives a possibility for more cutters at the center. A shallow cone angle will lead to increased steerability, better bit cleaning and increased aggressiveness. The cone angle can often be considered a trade-off. Figure 5.16 shows the four different bit profile types, from flat to long parabolic shape. The same figure indicates that a flat bit profile is optimal for hard formations and enhances the ability to steer the bit. Low ROP is a result of drilling with a flat bit profile. This is analogous, parabolic bit profile yieldings higher ROP. Besides hig ROP, long parabolic bit profile creates a more suitable bit for soft and abrasive formation containing shales, clays or/and mudstones. section 5.4.1 illustrates the different bit profiles and their properties. Flat profiles give the best durability for the drill nose, but the long parabolic profile is best for the shoulder durability. A bit profile between long and flat profile is often chosen to get as good as possible bit properties [22]

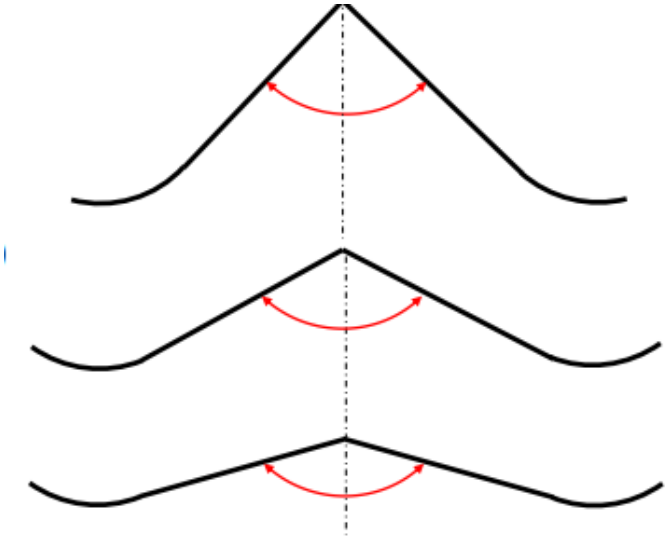

Figure 5.15: Deep($\approx 90°$), medium($\approx 120°$ - $140°$) and shallow($\approx 150°$) cone angles [22].

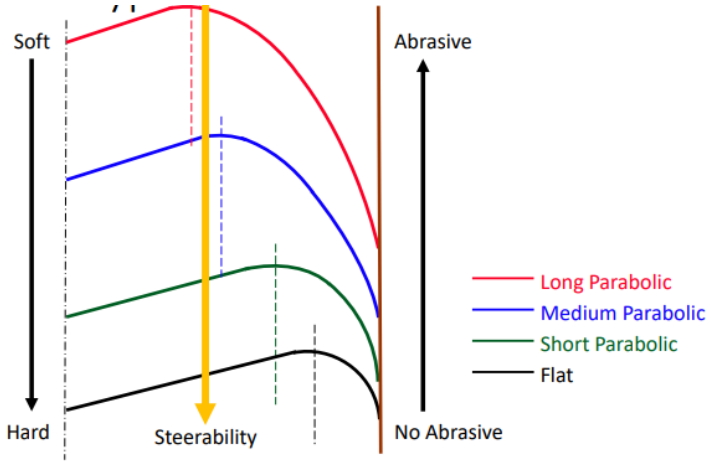

Figure 5.16: Different bit profiles and their properties [22].

5.4.2 Cutter Design

The size and number of cutters is relevant for the Depth of Cut (DOP) and ROP. Increasing the number of cutters will decrease the DOP and effectively decrease the ROP. A decrease in torque and increase of bit life is often observed when increasing number of cutters. The cleaning efficiency is however less effective. With fewer cutters it is possible to increase their and thus provide a higher DOP, and again results in a higher ROP and a more aggressive bit. The density of the cutters is also important. When increasing the distance from the cutters to the bit center, the cutters are exposed to higher velocity and will remove more rock cuttings. It is preferable to increase the cutter density towards the outer rows of the bit.

Furthermore, designing a suitable DOP can be done by effectively optimize the cutter orientation. The back rake angle, illustrated in Figure 5.17, is the angle of the cutter face perpendicular

to drilling direction. A back rake angle value of zero will provide the highest DOP. The bit will thus become more aggressive using lower back rake angles. Aggressive bits leads to higher ROP, but the cutters are subjected to more impact and the risk of damage is higher. Also could an aggressive bit be more exposed to changes in torque and leading to issues with the face control. The real ROP will still be higher with high back rake angles on the bit face because a more passive bit will avoid problems with the tool face. Normal values of back rake angle are 20°-2533° for the inner rows and 10° for outer rows. Figure 5.17 shows three back rake angles. The most aggressive angle, zero degrees, could be suitable for soft formations and then the angle should be increased for harder formations and directional drilling [59].

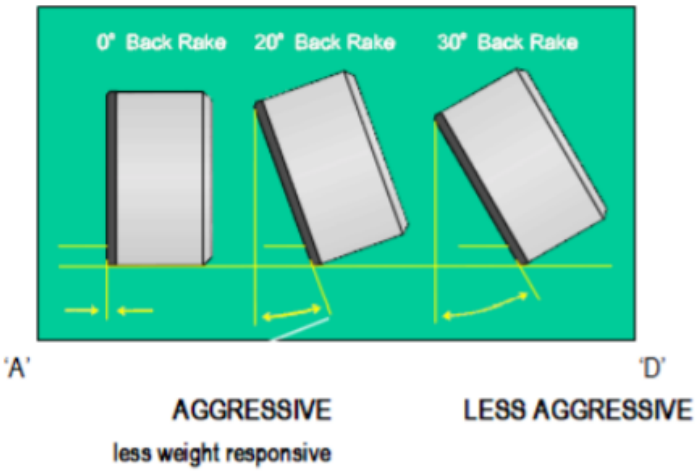

Figure 5.17: Different back rake angles [59].

Another drill bit angle important for cutter orientation design is the side rake angle. Figure 5.18 shows the side rake angle and it is defined as the angle perpendicular to the direction of rotation. The side rake angle aids hole cleaning because the cuttings is lead towards the outer parts of the bit with a positive side rake angle. It also gives a shear effect to the cutting action [59].

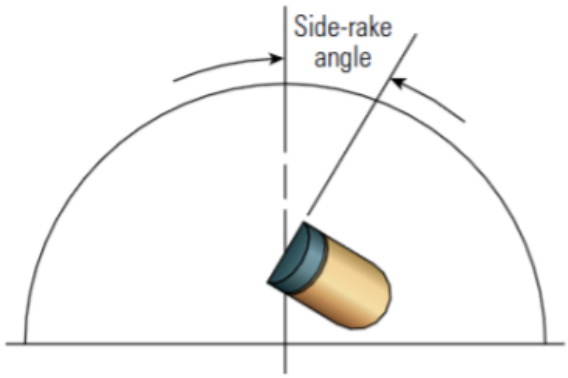

Figure 5.18: Side rake angle seen by looking down the hole [59].

The cutter layout is also an important bit property and is characterized by cutter orientation. There are two main layouts for placing the cutters. In Figure 5.19,the left illustration shows the ”single-set layout” of cutters. For this layout, none of the cutters are sharing the same radial or longitudinal position. This helps distributing the load even to all cutters. In the same figure, Figure 5.19, the right illustration illustrates the ”tracking cutter layout”, also called ”plural-set layout”. In this case, some of the cutters are overlapping eachother in radial and longitudinal position. This will lead to less distributed cutting [22].

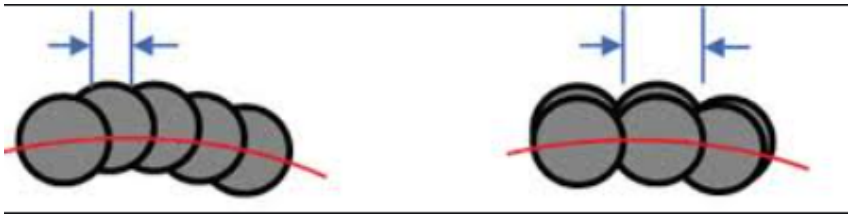

Figure 5.19: Single-set layout(left) and track-set layout (right) [54].

5.5 Drilling Hydraulics

To achieve sufficient drilling performance, a sufficient hydraulic system is crucial. The system is especially important for hole cleaning which again has a great effect on the Rate of Penetration (ROP). The drilling fluid has several properties that contributes to sufficient drilling performance[3]:

- Transport cuttings from bottom to surface.
- Maintaining wellbore stability, keep the system overbalanced.
- Cooling and lubrication of bit and drill string components.
- Produce mud cake, to prevent fluid loss to natural or induced cracks.
- Transfer of information by mud pulse telemetry.

5.5.1 Hole cleaning

ROP is an important drilling parameter because it is a measure of the time consumed during the drilling operation. Achieving the desired ROP and cutting costs is greatly dependent on sufficient hole cleaning.

Transportation of cutting varies with inclination and is generally divided into three flow regimes:

- Vertical section - $[0° - 30°]$

- Tangent section - $[30° - 65°]$
- Horizontal section - $[65° - 90°]$

Because the Drillbotics© competition requires a total maximum of 30° inclination, the focus will lay within hole cleaning in vertical section. Derivation of the equations presented in this section can be found in Appendix B.

Slip velocity of cutting particles in a laminar flow regime is given by:

$$v_{sl} = \frac{d_s^2 g(\rho_s - r\rho_f)}{18\mu f} \tag{5.24}$$

Where $d_s[m]$ is diameter of cuttings, $\rho_s[kg/m^3]$ is density of cuttings, $\rho_f[kg/m^3]$ is fluid density and $\mu_f[Pas]$ is fluid viscosity.

Not all the fluid flow in the system can be described by a laminar regime and slip velocity has to be expressed for all flow regimes as in Equation 5.25.

$$v_{sl} = \sqrt{\frac{4(\rho_s - \rho_f)g d_s^2}{3f\rho_f}} \tag{5.25}$$

where f is a friction factor determined from Figure 5.20.

The process of calculating the final slip velocity is as follows: Estimate v_{sl} with Equation 5.24, calculate the Reynolds number, estimate the friction factor with Figure 5.20 and then calculate v_{sl} with Equation 5.25.

After finding the slip velocity, required flow rate can be calculated using Equation 5.26:

$$q = A_{cs}\frac{v_{sl}}{1 - R_t} \tag{5.26}$$

5.5.2 Pressure Losses

Pressurised fluid is taken into the system from a water tap and transported to the swivel through a hose. The swivel pass the fluid down to the bit through the drill pipe. Because there is friction between the drilling fluid and each component, there will be a continuous pressure loss throughout the system. By decomposing the pressure loss into losses over components the required pressure can be estimated:

$$P_{req} = \Delta P_{hose} + \Delta P_{swivel} + \Delta P_{DP} + \Delta BHA + \Delta P_{nozzle} + \Delta P_{ann} \tag{5.27}$$

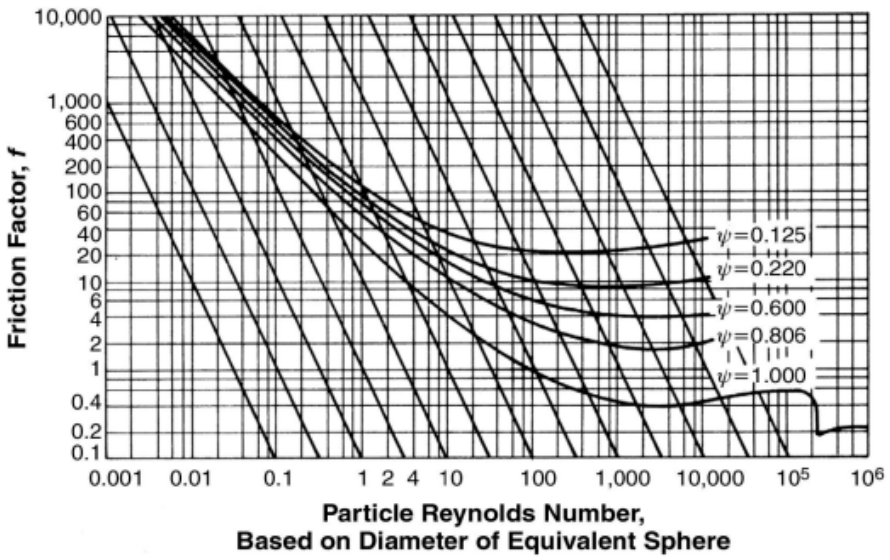

Figure 5.20: Relationship between *Re* and f for settling particles in Newtonian fluids [2].

Only major pressure losses are taken into account in Equation 5.27, and minor pressure losses are neglected. To compensate for this, a safety factor is usually added to the required pressure.

5.5.2.1 Pipe Pressure Losses

Pressure losses in the system must be estimated for both the flow inside the drill pipe and the annular flow outside the drill pipe. This can be estimated using Equation 5.28. Where D_h is the inner diameter of the BHA and drill pipe when calculating the pressure losses inside the pipe. For the annular flow, the diameter is: d_h = OD_{hole} - $OD_{DP/BHA}$.

$$\Delta P_i = f_i \frac{L_i}{dh,i} \frac{\rho_f v_i^2}{2} \tag{5.28}$$

Where ΔP is the pressure loss, L_i[m] is the length of the part where the pressure loss occur, ρ_f is the fluid density and v_i[m/s] is the velocity of the fluid. The last parameter, f_i, will vary depending on the type of flow regime. The flow regime is dependent on the Reynolds number calculated in Equation B.7. If the Reynolds number is less than 2300, the flow is laminar and above 2300 the flow is turbulent. If the flow is turbulent, Equation 5.29 and 5.30 are used. The value of f will then be the average between the two formulas output.

$$\frac{1}{\sqrt{f}} = -1.8log[(\frac{\epsilon/D}{3.7})^{1.11} + \frac{6.9}{Re}] \tag{5.29}$$

$$f = \frac{0.25}{[log(\frac{\epsilon/D}{3.7} + \frac{5.74}{Re^{0.9}}]^2} \tag{5.30}$$

If the flow is laminar, then the friction factor will be estimated using Equation 5.31. This formula is only applicable for laminar flow and pipe roughness that are not to extreme.

$$f = \frac{64}{Re} \tag{5.31}$$

5.5.2.2 Bit Pressure Losses

The fluid exiting the drilling bit nozzels must have a high velocity in order to sufficiently remove drilling cuttings from the bottom and out of the well. Because velocity is inversely proportional to cross-sectional area, high velocity is achieved by using nozzles with relatively small cross-sectional area. These small nozzles introduce a bit pressure drop. Fluid velocity through the nozzles, v_n can be estimated with Equation 5.32.

$$v_n = C_d \sqrt{\frac{2\Delta P_{nozzle}}{\rho_f}} \tag{5.32}$$

Where C_d is a discharge coefficient.
The discharge coefficient is usually equal to 0.95 obtained from experimental measurements showing that v_n is overestimated using Equation 5.32. By rearranging Equation 5.32 and expressing v_n as a function of flow rate and nozzle area, the pressure loss from the drilling bit can be obtained by:

$$\Delta P_{nozzle} = \frac{\rho_f q^2}{2A_n^2 C_d^2} \tag{5.33}$$

Where $q[m^3/s]$ is the flow rate and $A_n[m^2]$ is the total flow area of the nozzle(s).

5.6 Control Theory

To drill wells autonomously, a sophisticated control system is required. The general control objective is to use the inputs (u) to manipulate the states (x) towards a reference. Some states are measured through sensors while others may only be estimated using measurements of other states. An estimated state is denoted $\hat{x}$. Using measurements and estimated states to determine the new input to the system is called closed-loop control. Sensor measurements will always have some uncertainty, process noise is unpredictable and no system model is completely accurate. Closed-loop control is therefore essential for good control performance in complex systems.

5.6.1 PID Controller

Converging towards and maintaining a monovariable reference can in many control applications be achieved by using a PID-controller. A PID-controller is a closed-loop controller for

unmodelled control that monitors the deviation from the reference (P), accumulated error deviation (I), and rate of change of the error (D) [34]. Depending on the control application, a simpler PI or PD controller may be sufficient.

$$u(t) = K_P e(t) + K_I \int_0^t e(\tau)\, d\tau + K_D \frac{de(t)}{dt} \tag{5.34}$$

Where $e(t) = r(t) - y(t)$ is the difference between the reference r and the measured plant output y. K_P, K_I, and K_D are constants that can be tuned individually to obtain the desired control behavior. Typical considerations when tuning these parameters are stability and convergence rate. In theory, any stable system with a constant reference r and a greater than zero K_i will eventually converge towards the reference value. In practice, there are limitations to maximum system input.

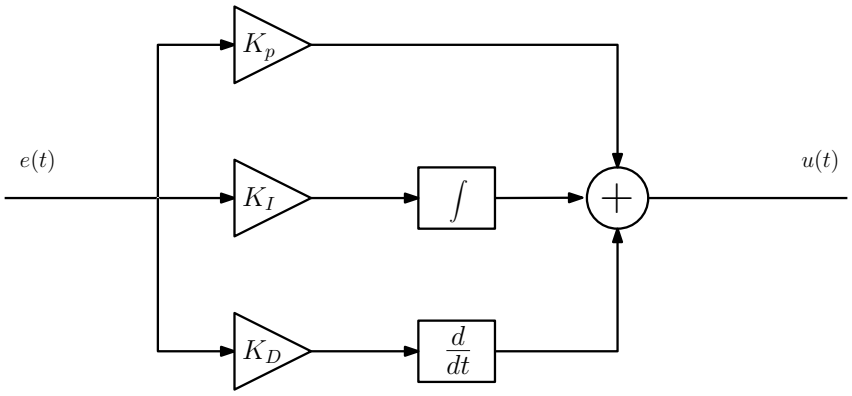

Figure 5.21: PID-controller diagram

5.6.2 System Model

Control performance can be improved if it is possible to make predictions of future states given the current states and inputs. The set of equations for predicting plant behavior is called a model. A model is obtained from physics equations and experimental data. Continuous systems may be modelled as a set of differential equations, while a discrete system models provide an estimate of the states at the next time-step. Using assumptions on how multiple states and inputs affect each other, models can be used for multivariable control. Multiple states can then be steered towards multiple state references. Models can also be used to simulate plant input response in software.

A convenient linear system matrix representation is the state-space form [34]. The state-space form is used directly in multiple control system algorithms.

$$\dot{x} = Ax + Bu, \quad y = Cx + Du \tag{5.35}$$

A and B are matrices that when multiplied with the state and input vectors x and u represent the full set of ODEs describing the system. C and D provide the system output vector given the current states and outputs. State-space form can also be used for discrete systems.

$$x_{k+1} = A_d x_k + B_d u_k, \quad y_k = C_d x_k + D_d u_k \tag{5.36}$$

Discrete state-space systems provide the state for the next time-step rather than the rate of change.

5.6.3 Optimal Control

When a system model is obtained, it is possible to attain an optimal input sequence to converge towards a desired system state. The input sequence can be formulated as a cost function were deviations from the reference, state values and input values can be penalized to achieve desired control performance. A common implementation is to use quadratic penalization with state weights Q and input weights R.

$$\min_{x,u} J = \min_{x,u} \sum_{k=0}^{N-1} (x_k^T Q x_k + u_k^T R u_k) \tag{5.37}$$

5.6.4 MPC

Model Predictive Control (MPC) does an optimal control optimization at every time-step with the current state as the initial conditions. The MPC predicts an input sequence of length N known as the prediction horizon, before applying the subsequent input to the system. The prediction horizon must be sufficiently long to allow system convergence towards the reference within the input sequence. A rule of thumb is that the horizon must be at least twice as long as the number of inputs required to converge towards the reference. Certain control applications will have significantly improvements in control performance, allowing highly accurate manipulation of states and enforcement of constraints on states and inputs. The high computational cost limits its use for certain control applications.

An approach to reduce the overall computational cost is to use different sized time-steps in the optimization. Smaller time-steps are generally used for the first part of the input sequence. The size of the time-steps are then increased to limit the computational cost. The rational is that the system requires less accurate control after it has already converged, and the states further into the future will be less accurate due to accumulated simulation error. This trade-off allows for longer predictions with smaller computational cost, at the expense of some long term planning capabilities.

5.6.5 Kalman Filter

A Kalman filter is a state estimator for stochastic systems [42]. All systems will have some process noise and measurement uncertainty. The Kalman filter can provide sensor fusion by combining a model estimate and multiple sensor measurements. Each estimate is weighted based on its covariance. Assuming that the noise has a Gaussian distribution, the Kalman filter can find the estimate with the smallest covariance, thus the optimal state estimate.

The Kalman filter is a model based observer were the estimate of the model is compared to the output of the system. The Kalman filter is based on the linear state-space model.

$$\hat{x}_k = A\hat{x}_{k-1} + Bu_k + K_k(y_k - C(A\hat{x}_{k-1} + Bu_k)) \tag{5.38}$$

The prediction of the filter is often written as a separate equation. $\hat{x}_k^-$ is called the prior estimate and is a prediction of the next state estimate.

$$\hat{x}_k^- = A\hat{x}_{k-1} + Bu_k \tag{5.39}$$

The predicted covariance of the state estimate is calculated based on the previous covariance, the system matrix, and the process noise covariance Q.

$$P_k^- = AP_{k-1}A^T + Q \tag{5.40}$$

The Kalman filter is an iterative algorithm that is updated each time-step. K_k is the Kalman gain and is calculated such that it minimizes the variance of the optimal state estimate. The Kalman gain is smaller for larger measurement noise covariance R.

$$K_k = \frac{P_k^- C^T}{CP_k^- C^T + R} \tag{5.41}$$

The new estimated state is calculated based on the prior estimate and the new measurement.

$$\hat{x}_k = \hat{x}_k^- + K_k(y_k - C\hat{x}_k^-) \tag{5.42}$$

The error covariance matrix of the current best estimate is calculated based on the predicted covariance and the Kalman gain.

$$P_k = (I - K_k C)P_k^- \tag{5.43}$$

The error covariance matrix can be used to monitor the expected deviation of the state estimate. Variance is the squared value of the expected deviation. The diagonal elements are the variances of the state estimates.

5.6.6 Extended Kalman Filter

A non-linear system cannot be implemented directly using the equations described in section 5.6.5 as non-linear systems can not be described by a linear state-space model. A non-linear system model can be written on the form [43]:

$$x_k = f(x_{k-1}, u_k) + w_k, \quad y_k = g(x_k) + v_k \tag{5.44}$$

The Kalman function requires a linear function to guarantee convergence. The Kalman filter requires all noise to have a Gaussian distribution. Passing a Gaussian distribution through a non-linear function will in general not give a Gaussian distribution output. w_k and v_k are noise values for the states and outputs at a specific time-step.

Some non-linear systems can be well approximated using linearization around a point. This is the case if the system is close to linear in a region around the linearization point. The Kalman filter can with this assumption use a linearized state-space model when making prior predictions. A general linearized system is described in Equation 5.45.

$$f(x) \approx f(\hat{x}) + f'(x)(x - \hat{x}) \tag{5.45}$$

The linear approximation can be used directly in the Kalman filter by calculating the Jacobians of the state and output functions.

$$F = \frac{\partial f}{\partial x}|_{\hat{x}_{k-1}, u_k}, \quad G = \frac{\partial g}{\partial x}|_{\hat{x}_k} \tag{5.46}$$

If either the states or outputs are linear, the state-space matrix can be used instead of the Jacobian approximation. If both states and inputs are non-linear a new Kalman compatible model can be estimated using the Jacobians.

$$\Delta x_k \approx F\Delta x_{k-1} + w_k, \quad \Delta y_k \approx G\Delta x_k + v_k \tag{5.47}$$

If the Jacobian can be computed analytically there is only a minimal additional computational cost when using an extended Kalman filter compared to a regular Kalman filter.

5.6.7 Coordinate Frames

Knowing relative positioning and orientation between frames is often useful in control theory. Different coordinate frames simplifies movement modelling because movements can be described relative to the moving object itself rather than relative to the inertial frame.

There are multiple methods of representing orientation in 3D. Euler angles represents any orientation as a set of 3 angle displacements from a frame, referred to as yaw (ψ), pitch (θ), and roll (ϕ) [50]. Position can be described in Cartesian coordinates, where every position is a displacement in x, y, and z relative to a frame.

Rotation matrices can be used to translate positions and movements between frames with different relative orientations. Combined with Cartesian position displacements, any position and orientation can be translated from one frame to another. The inverse of a rotation matrix is equal to its transposed value. The transposed rotation matrix inverses the original and destination frame. Rotation matrices can be sequenced together to translate from one frame to another using an intermediate frame. A rotation matrix will maintain scaling in any translation.

$$(R_a^b)^{-1} = (R_a^b)^T = R_b^a \tag{5.48}$$

$$R_b^c R_a^b = R_a^c \tag{5.49}$$

$$det(R_a^b) = 1 \tag{5.50}$$

The notation of a rotation matrix has a subscript variable denoting the original frame and superscript variable denoting the destination frame.

Euler angles have a set of rotation matrices for translating between two Cartesian coordinate frames based on their relative orientation.

$$R_z(\psi) = \begin{bmatrix} \cos\psi & -\sin\psi & 0 \\ \sin\psi & \cos\psi & 0 \\ 0 & 0 & 1 \end{bmatrix} \tag{5.51}$$

$$R_y(\theta) = \begin{bmatrix} \cos\theta & 0 & \sin\theta \\ 0 & 1 & 0 \\ -\sin\theta & 0 & \cos\theta \end{bmatrix} \tag{5.52}$$

$$R_z(\phi) = \begin{bmatrix} 1 & 0 & 0 \\ 0 & \cos\phi & -\sin\phi \\ 0 & \sin\phi & \cos\phi \end{bmatrix} \tag{5.53}$$

The position translation in a roll-pitch-yaw system is the sequence of the translation matrices described in Equation 5.51, 5.52, and 5.53.

$$R_b^a = R_z(\psi)R_y(\theta)R_x(\phi) \tag{5.54}$$

A consideration when using Euler angles is the possibility of gimbal lock. If the pitch is exactly 90°, the orientation can not be uniquely represented using Euler angles. Pitch must therefore be defined such that gimbal lock will not occur.

5.6.8 Angular Velocities

Movements in roll-pitch-yaw needs special consideration when translating between frames. A general translation of angular velocity between frames is described in Equation 5.55.

$$\omega_{ab}^a = \omega(\dot{\psi}) + R_z(\psi)\omega_y(\dot{\theta}) + R_z(\phi)R_y(\theta)\omega_x(\dot{\phi}) \tag{5.55}$$

Where $\omega(\dot{\psi})$, $\omega_y(\dot{\theta})$, and $\omega_x(\dot{\phi})$ are shorthand notations for angular velocity vectors.

$$\omega(\dot{\psi}) = \begin{pmatrix} 0 \\ 0 \\ \dot{\psi} \end{pmatrix}, \omega_y(\dot{\theta}) = \begin{pmatrix} 0 \\ \dot{\theta} \\ 0 \end{pmatrix}, \omega_x(\dot{\phi}) = \begin{pmatrix} \dot{\phi} \\ 0 \\ 0 \end{pmatrix} \tag{5.56}$$

6 Mechanical Rig Systems

In previous competitions, the NTNU teams has persisted to pursue the same drilling concept utilizing a down hole PDM motor to steer the drill bit in the desired direction. However, the NTNU team of 2021 decided to build an improved mechanical design based on a distinctive drilling concept, abandoning the PDM motor. The novel concept however, presents a similar rig design by recycling the rig framework and hoisting system. The goal was to build a robust mechanical design that can enhance the overall drilling efficiency and steering precision and ensuring an optimized drilling performance by providing a fail-safe design with sophisticated and intricate software solutions. This section will thoroughly present the alternations made to the mechanical design.

6.1 Previous Design

The miniature drilling rig to be used in the upcoming Drillbotics competition has inherited the framework and basic principles from the previous years. The remaining components have been replaced. Figure 7.1 illustrates the drilling rig from last year.

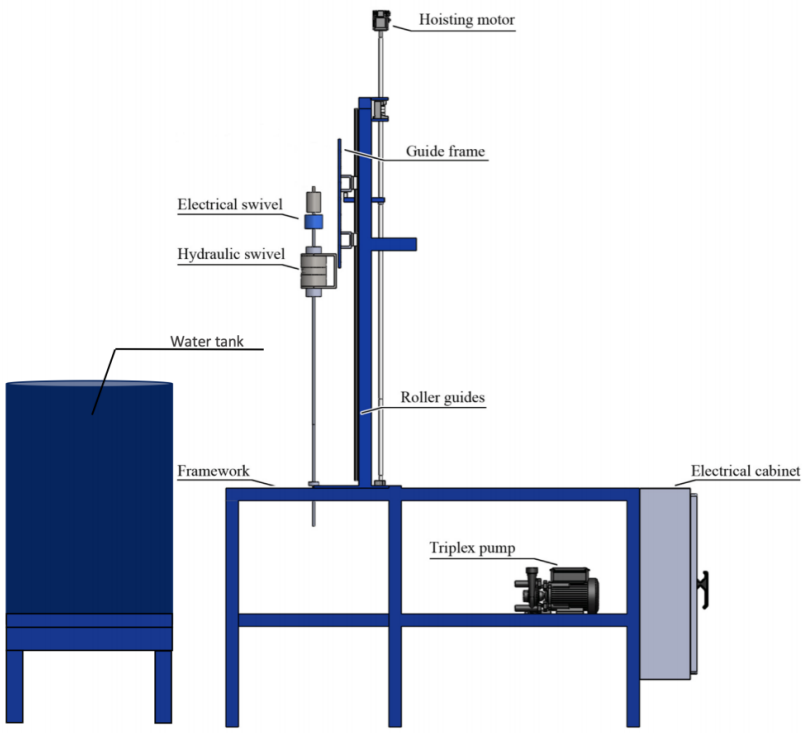

Figure 6.1: Original miniature rig from 2019.

The rig is designed in line with the Drillbotics Guidelines provided by the competition committee. The miniature drilling rig is supposed to resemble a full-scale drilling rig from the oil and gas industry. Focus areas of previous years was mobility, functionality, safety, versatility

and high precision drilling performance. The focus for the new mechanical design is primarily unchanged, although high precision in deviated drilling has been predominant. That being said, precision is of no use should the drilling operate in an unsafe manner.

The drilling rig framework consists of hollow yet robust steel beams mounted together with bolts and nuts as well as welded parts. The outline of the framework is constructed such that it easily and safely can house the mechanical equipment needed for the rigs drilling purposes. The total height of the rig is 285 cm (9.35 ft) and total width of 70 cm (2.3 ft). The rig has a total weight of approximately 100 kg (220.5 lbs). Castor wheels ensures mobility of the rig. 6.2, shows the derrick folded down, a design feature implemented to ease transportation of the drilling rig.

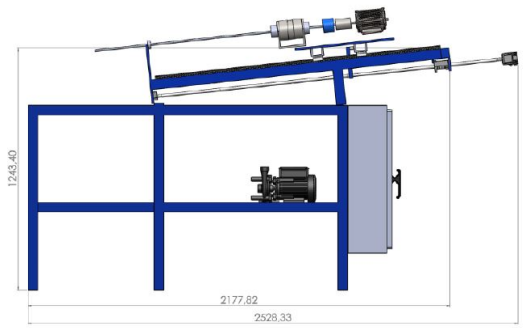

Figure 6.2: Rig design with the derrick folded down [5].

6.2 Rig Systems

The miniature drilling rig is a composite system with parts working in conjunction with each other to enhance the drilling operation. Each component is designed, built and tested in detail and the communication between the systems constitutes the complete drilling concept. In the following sections, each system and component is described in detail to give a full understanding of how the drilling rig is able to operate. For the sake of simplicity, the description is given in an order starting from the top of the rig and moving downwards for each rig component. Power consumption calculations for the rig system is found in Appendix D.

6.2.1 Hoisting System

In full-scale drilling rigs today, the vertical motion is provided using draw works raising and lowering a traveling block in which the top drive is attached to. Thus, the Weight On Bit (WOB) is only achieved by make-up (MU) of drill pipes and drill collars. For simplicity, the lateral motion of the top drive in the miniature rig is provided and controlled by a hoisting system consisting of a ball screw and a motor in which rotational motion is converted to vertical motion.

WOB is provided by the hoisting systems total weight which is controlled and registered by a load cell mounted on the hoisting system. The drill pipe and additional drilling components are mounted below an aluminium support block and the weight of the hoisting system is transferred to the lower systems through the aluminum block. The ball screw method from previous years was re-used because it provides an efficient way of applying WOB with high precision and step resolution. Dual roller guides fixed on the derrick enables vertical movement of the steel guide frame in which the top drive motor is attached. Figure 6.3 illustrate the roller guide system used. A servo motor is coupled onto a ball screw where a ball screw nut can move along the vertical axis. A set of this roller guide is mounted on each side of the derrick to guide the rig frame in vertical motion.

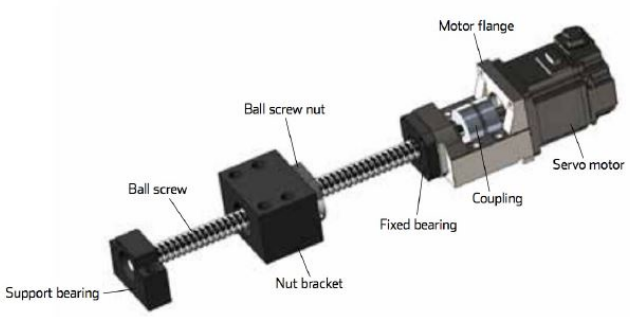

Figure 6.3: Dual roller guides allow for vertical motion of the drilling system [5].

A steel plate holding the complete drilling equipment is mounted to the guide frame. Figure 6.4 shows stop buttons on the roller guides that can be triggered by the moving frame. The buttons will break the circuit to the hoisting motor to prevent the guide frame from moving too high or too low.

Figure 6.4: Stop button installed on roller guides to break circuit to hoisting motor when moving too high or low[5].

The load cell is a hollow cylindrical cell welded onto the guide frame and connected to the nut bracket located in the middle of the ball screw. Figure 6.5 shows the placement of the load cell on the rig . The load cell and hoisting system is described in more detail in section 9.

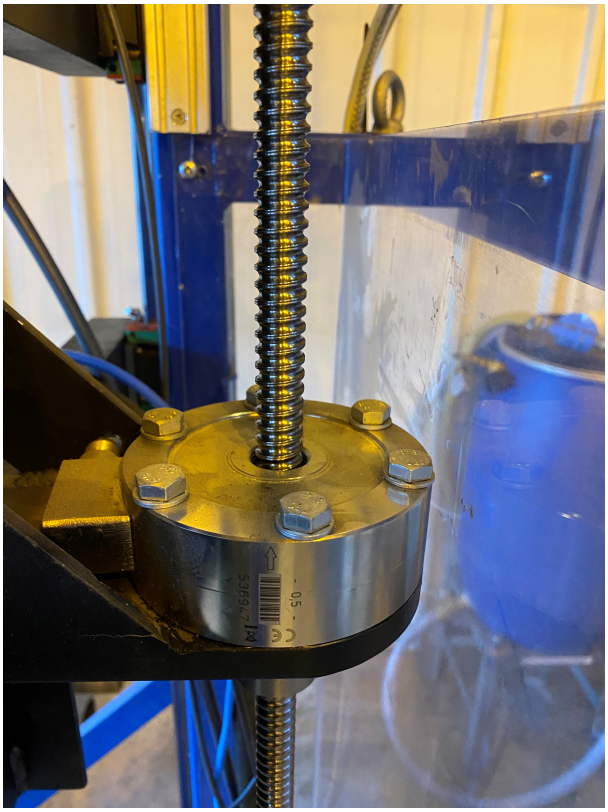

Figure 6.5: Load cell with a ball screw going through it.

6.2.2 Rotary System

The rotary system of a full-scale modern drilling rig is usually driven by a motor moving axially inside the derrick while at the same time providing rotational motion and torque to an attached drill pipe. The top drive motor transmits torque to the drill pipe and further down to the attached drilling bit. The rotational motion and torque is an important component for aiding with downhole cleaning in full-scale drilling operation. The rotary system used in this miniature drilling rig is based on the same concept of rotational torque transmission, however, in this case the torque is transmitted to an aluminium rod inside the drill pipe, not to the drill pipe itself. The pipe will slide during drilling with a thin cylindrical rod of 3.5 mm rotating inside it. The top drive, which consists of a robust servo motor of 0.75 kW, is able to provide a rotational speed of 3400 RPM and a torque of 45 Nm. The engine is mounted directly on a steel plate that moves laterally by the hoisting system. A drill chuck is latched to the top drive by means of a hollow cylindrical steel fastener.

6.2.2.1 Drill Chuck

A regular drill chuck that can be found on hand-held drills was implemented in the mechanical design in order to transfer the torque from the top drive to the rod while keeping the rod stable during rotation. The torque needed in this system is low enough such that a manual drill chuck was sufficient, thus reducing the overall mechanical cost. Figure 6.6 shows the drill chuck with fastening key and screw. The drill chuck enables easy and safe replacement of the aluminum rod.

Figure 6.6: Manual drill chuck to fasten rotating aluminium rod [9].

6.2.2.2 Azimuth Motor and Gearbox

In order to change the azimuth of the drill pipe while the internal rod is rotating, a separate motor with a hollow gearbox and a rotary table is implemented. The gearbox is a high precision spiral guide Hypoid Gear with a ration of 30:1 and permissible torque of 30 Nm. The gearbox is suspended from a solid aluminium plate attached to a steel plate following the motion of the hoisting system such that the weight applied to the bit is not projected onto the slim rotating rod. Although the axial load will be transferred directly from the hoisting system to the drill pipe via the hydraulic swivel system below, the gearbox system can withstand up to 300 N in axial load should the system below fail. The Figure 6.7 shows the gearbox suspended from aluminium block with DC motor attached on the right side.

Figure 6.7: Gearbox suspended from aluminium block with DC motor attached [30].

6.2.3 Hydraulic System

The hydraulic system is kept as simple as possible. It consists of a water-supply, water hose and a hydraulic swivel. The swivel illustrated in Figure 6.8, is located below the gearbox and provides fluid down through the drill pipe to exit the drilling bit. The hydraulic system allows for cooling and lubrication of the drill bit in addition to transporting cuttings out of the well.

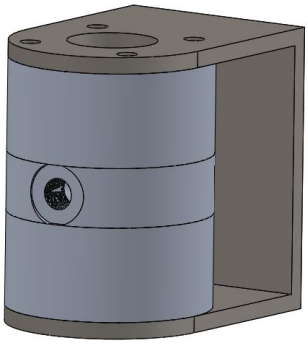

Figure 6.8: Hydraulic swivel housing

The main changes done to the hydraulic swivel was hollow driving shafts allowing the rod inside to rotate freely without fluid leaking out. The drill pipe is connected directly beneath the swivel. Because the azimuth is changed above the swivel, it was important to design fixed threads in the shafts located inside the swivel housing. A detailed description of the hydraulic system is described in section 7.

6.2.4 Drilling System

6.2.4.1 Drill Pipe

The guidelines allows both stainless steel and aluminum as drill pipe material. Careful considerations and calculations has been made to make sure the best possible material is chosen. The most significant difference in performance between the two is pipe bending as described in section 8.2.1. This limitation alone rules out stainless steel as material for the drill pipe, as it surpasses its yield strength significantly and will go way into its plastic regime for this years requirements. Disregarding stainless steel as an option, leaves aluminum as the only option. The team have decided to use aluminum 7075-T6 alloy as material for the drill pipe based on calculations shown in section 8.2.1.

6.2.4.2 Tool Joint

The drill pipe will be connected with the same Vertex tool joint used by previous teams from NTNU. This joint, shown in Figure 6.9, will be used to connect the pipe to both the BHA and the hydraulic swivel. The joint has proven to work extraordinary, hence it will be used again this year.

6.2.4.3 Rod

The rotating rod extends from the top drive, through a hollow gearbox and down into the swivel and further down to the drilling bit. The rod has an OD of 3.5 mm (0.138 in.) and is the same material as the drill pipe, aluminium 7075-T6.

Figure 6.9: Vertex tool joint.

6.2.4.4 Stabilizers

The drilling system has two stabilizers mounted to improve performance and workload limits. Stabilizers will reduce effective length, which then minimize the risk of buckling the pipe, as well as reducing the lateral vibrations in the system. The upper stabilizer is mounted 95 cm (37.4 in) above the floor surface at the drill floor, while the lower stabilizer is mounted in the riser right above the rock sample as shown in Figure 6.10. Both the stabilizer are roller bearings with an inner diameter equal to the outer diameter of the drill pipe, 9.525 mm (3/8 in). By separating the two stabilizers at a certain distance, the drill pipe is divided into parts with a minimum effective length to raise buckling limit as much as possible.

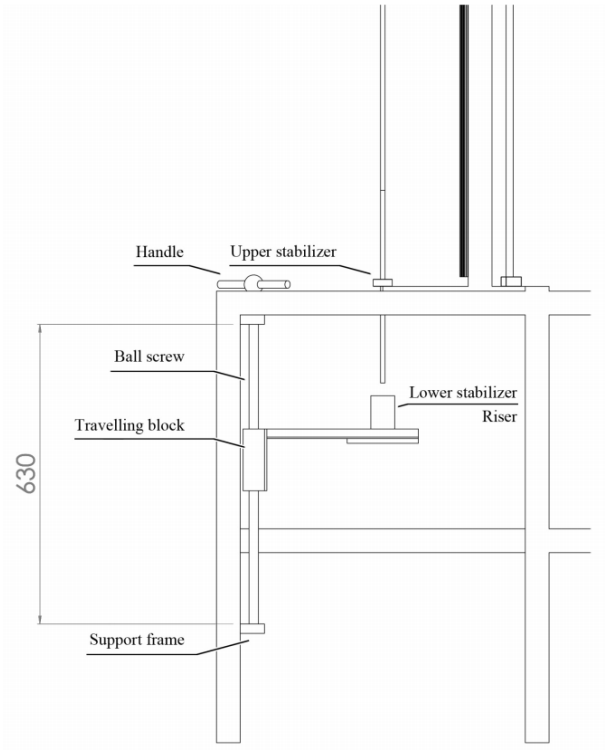

Figure 6.10: Lower setup of the rig with stabilizer locations [5].

6.2.4.5 Riser Element and Bell Nipple

A hollow cylinder in aluminium is placed beneath the drill floor simulating a drilling riser. It will stabilize and guide the drill pipe and BHA down to the rock sample below. An attached bell nipple prevent drilling fluid to leak out of the hole through the top of the riser. In Figure 6.11 the bell nipple is the golden attachment.

Figure 6.11: Hollow cylindrical riser element with golden bell nipple [5].

6.3 Downhole Power Design Alternatives

When drilling deviated wells its is important to provide sufficient power to the bit. Choosing a proper power design for the BHA can be challenging but crucial in order to meet the competition objectives. This rig design use a bent sub with a fixed angle to reach the desired inclination. However, there are other alternative directional systems that can be more suitable. Investigation of the most efficient and realizable alternatives and its feasibility, cost, relevance to the industry and robustness should be performed. This section investigates the different downhole design to drill deviated wells.

6.3.1 Adjustable Bent Sub Angle

Another alternative to the bent sub with a fixed angle is to implement an adjustable angle in the BHA or to build a RSS to drill the directional well path. However, both concepts implies a complex mechanical design. Adjustable bent sub angle would also require a hydraulic system to activate pins that would adjust the angle on the bent sub. Because the team aimed to not use a pressurized system, the idea was not further investigated.

6.3.2 Hammer Drilling

An interesting drilling method considered was hammer drilling. Hammer drilling allows for efficient drilling in hard formations and is frequently used in the mining industry and groundwater extraction. There are two ways of performing hammer drilling."Down the Hole (DTH), and "Top Hammer drilling" [53]. DTH drilling is a method were the drill bit is driven by a hammering piston inside the drill pipe located behind the bit. This piston is driven by compressed air and allows for powerful penetration of the formation. The fact that the piston is located inside the drill pipe allows for straight guidance of the system. Top Hammer drilling is quite similar, but the hammering force is applied at the top and propagated to the bit through the drill pipes and collars. This method will however lead to vibrations and uncertainties in the system with respect to stability and direction. Hammer drilling is most applicable to drilling straight wells in hard formation and does not allow for steerability. Soft formation will not be able to absorb the impact and thus the idea of implemented hammer drilling was discarded [63].

6.3.3 Positive Displacement Motor

The teams from the past two years have focused on a miniature PDM design as their main downhole power input. The motor converts hydraulic energy from the drilling fluid to rotational force by the use of lobes as described in paragraph 5.2.2.1. The previous teams have put down a lot of work and research in developing a downhole PDM and their research proved that the *concept* is feasible. However, none of the teams have managed to make the developed PDM to work ideally. The main problem have been to design a PDM that delivers enough torque and RPM.

From experience obtained by previous teams, the PDM is stated as a high-risk factor in the project as the possibility of ending up with a non-functioning PDM is present, This is mostly because of the combination of a complex design and limited time and labor. The alternative is very interesting because the BHA and PDM will reflect a miniature version of the full-scale drilling operations. The concept of a BHA with a PDM is shown in Figure 6.12.

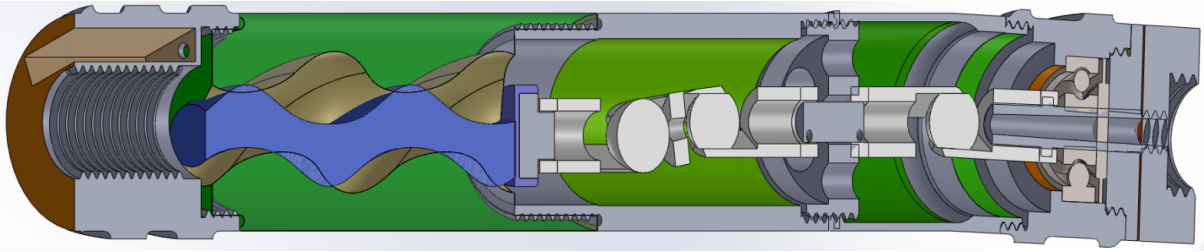

Figure 6.12: Concept design of BHA with PDM as power section.

Because the alternative is proven successful in the industry, there is a lot of information and

research about PDM and their motor sizes from the industry. The data available is not very applicable to the miniature drilling parameters. A solution to this is to create a graph from industry sized PDMs and extrapolate to relevant values for the miniature rig. The team investigated the motor length vs. the motors diameter and found that maximum motor diameter size would be approximately 33 mm (1.3 in.). To create the plot, relevant information was retrieved from Baker Hughes handbook for PDMs [13].

Figure 6.13 shows that using a PDM motor with OD 33 mm will require a motor length close to 185 cm (6 ft.). This is for a industry standard 5/6 lobe configuration. For the miniature drilling rig, the motor length is too big to implement. Past years experience together with the PDM solution and the data from Baker Hughes handbook, the team decided to not go further with the PDM alternative [13].

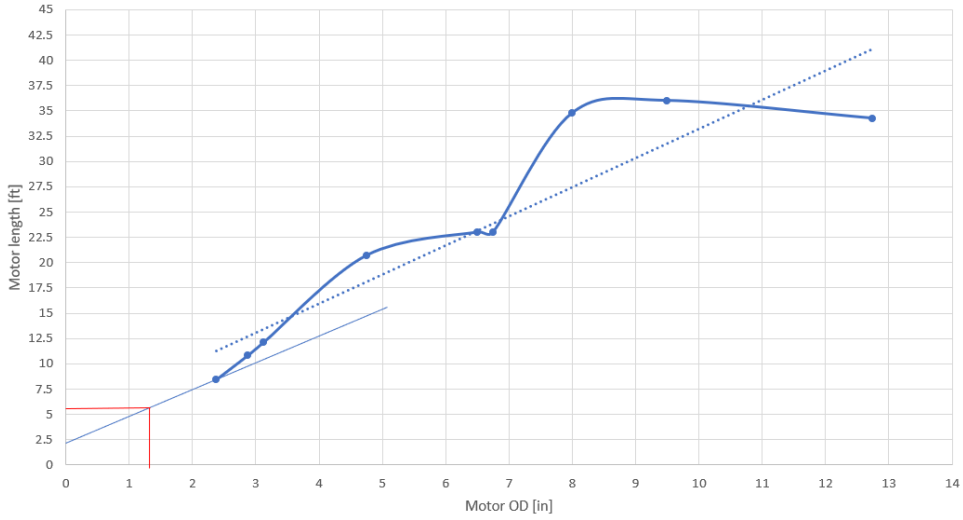

Figure 6.13: Different PDM lengths for increasing motor OD.

6.3.4 Turbine Motor

Another design considered for the BHA power section was a miniature Downhole Turbine Motor (DTM). Similar to the PDM, the DTM converts hydraulic energy from the drilling fluid to rotational force as shown in Figure 6.14. A turbine consists of a bladed rotor that rotates at a rate proportional to the speed of the drilling fluid flow. Sensors are often used to keep track of real-time rotation of the blade and thus monitor the flow rate of the drilling fluid. The turbine runs on high rotational speed and low torque values. Because the DTM requires a gear, it is considered a complex solution and a a comparison of the PDM and DTM was made to investigate whether the turbine performed better than PDM. A research has proven that a well designed PDM is much more energy-efficient and beneficial compared to a turbine motor for

drilling purposes [3].

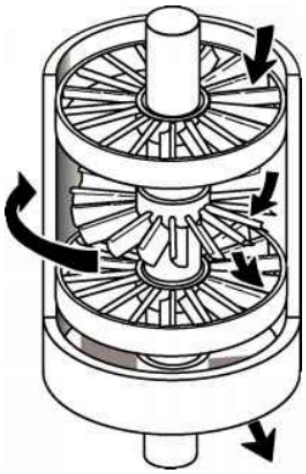

Figure 6.14: Concept of Downhole Tubine Motor [3].

Schlumbergers Neyfor Turbodrill Handbook [23] has been used when creating the relevant graphs for the turbine solution. Firstly, the team investigated the Gallons Per Minute (GPM) required for a turbine motor with OD 33 mm (1.3 in) to start rotating. The data points for Figure 6.17 were found from Figure 6.16 by drawing a line (black) from where 8.3 PPG would be, using a little shorter distance than between 10, 12, 14 and 16 PPG. Then the value for starting the rotation is read. The value of 8.3 PPG is used because the team will be drilling with non pressurized water. Doing this for different motor ODs and plotting it gave us a GPM of 35 to start rotating a turbine motor with OD 1.3 inches. Figure 6.15 shows that the maximal outflow from the pump is 6 GPM. Therefore this is indicating a problem for the turbine motor solution.

SPECIFICATIONS	U.S. Measure	Metric Measure
5CP6120		
Flow	6.0 gpm	23 lpm
Pressure Range	100 to 1600 psi	6.9 to 110 bar
Pump RPM*	1400 rpm	1400 rpm
Bore	0.787"	20 mm
Stroke	0.709"	18 mm
Weight	19.9 lbs.	9 kg

Figure 6.15: Pump specifications [14].

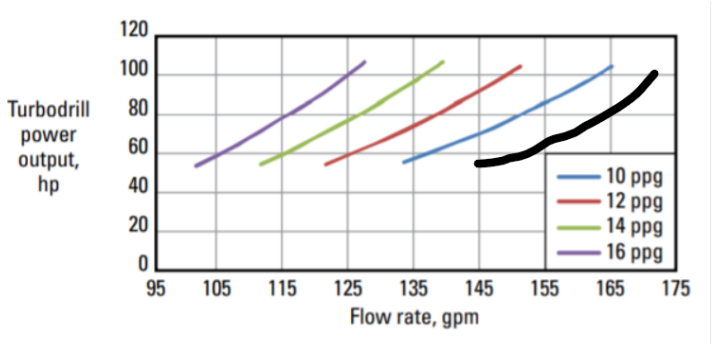

Figure 6.16: Flow rate for different fluid densities for turbine motor with OD 3.375 in. [23].

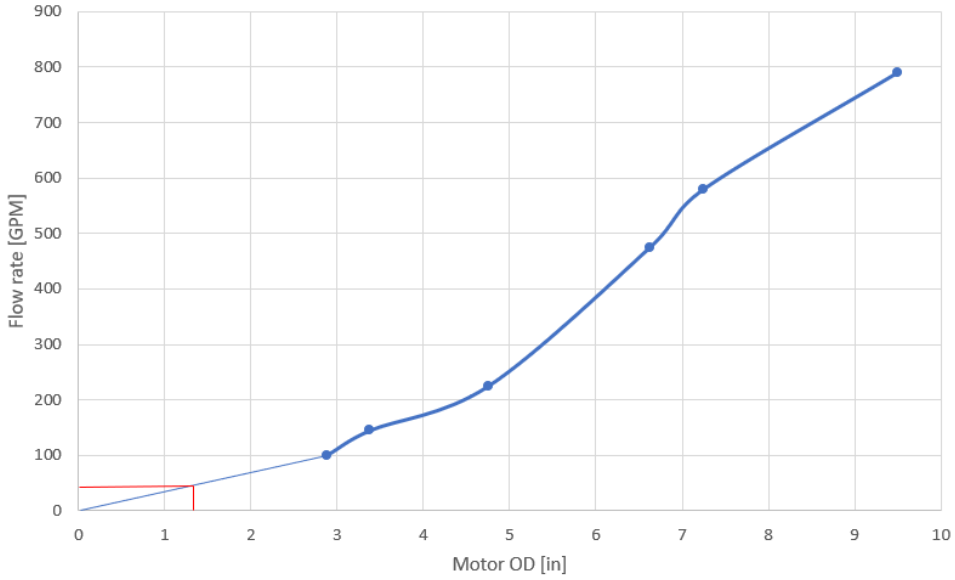

Figure 6.17: Flow rate for various motor ODs. [23]

The required GPM and Figure 6.18 indicates a spatial limitation for the turbine solution. This graph is created in the same way as for the PDM alternative. The plot indicates a length of 335 cm (11 ft.) for the turbine which is longer that the entire drilling rig. Because of these requirements for the turbine solution the team decided not to go forward with this alternative.

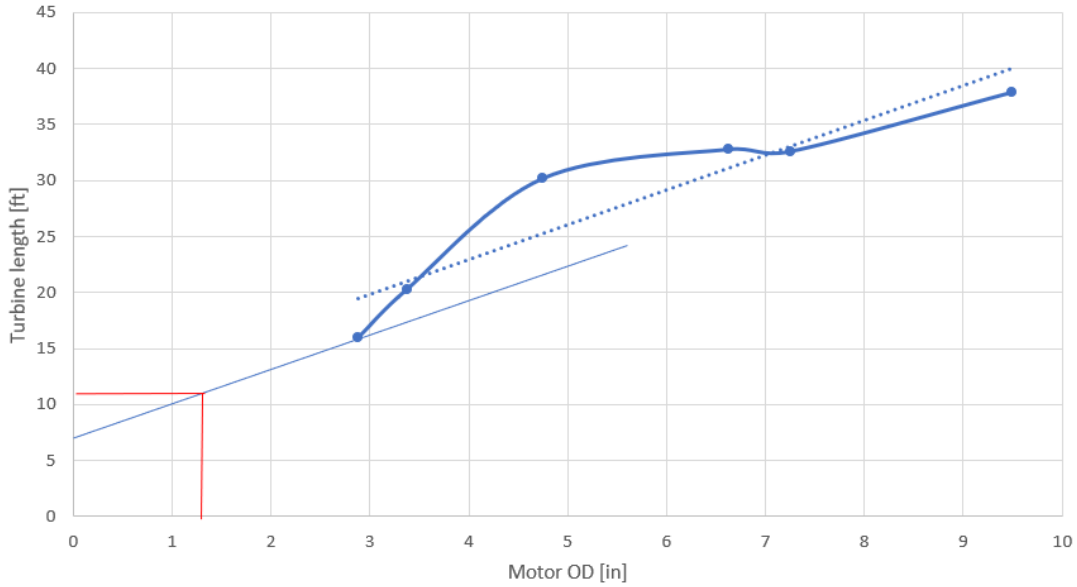

Figure 6.18: Turbine length for different motor OD. [23]

6.3.5 Electrical Miniature Motor

The use of an Electrical Miniature Motor (EMM) has been a back-up option the past two years. It has been a reasonable plan B because it requires relatively small changes to the BHA to make it compatible with the BHA when a PDM was used to drive the bit. Although this years design would require major changes to the system, the team decided to keep the EMM as a redundancy. The BHA design would need significant changes and the electrical wiring with the electric swivel has to be reintroduced. This is not be a complex issue because all the required components are present and familiar to the drillbotics team.

EMMs have specified data sheets which results in simple estimations of maximum output power. The main challenge with an EMM is its vulnerability when exposed to water. This requires a sufficient sealing mechanism which has proven to be difficult to obtain. In addition, if the EMM stalls out it may not give expected outputs when it has peaked its performance. The concept of a BHA with an EMM as power section is shown is Figure 6.19.

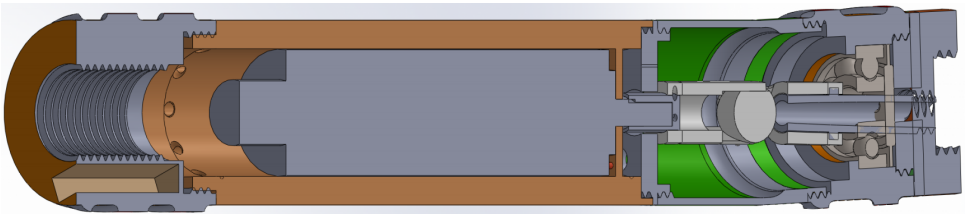

Figure 6.19: Concept of BHA with EMM as power section.

6.3.6 Solid Rod

The concept of using a solid rod as power to the bit is a mechanical concept inspired by the string trimmer and similar tools where rotating string inside the drill pipe transfers torque and RPM from the Top Drive (TD) to the drill bit.

The team found this solution interesting because it is a relatively predictable system in which is fully mechanical. The most prominent downside is that the design requires big modifications to the already existing drilling rig. They are however very possible to implement with respect to the teams time constraint and budget. In consultation with the supervisory team, the solid rod concept was decided to be used. One of the main reasons to step away from the PDM concept was mainly that it has not been successful. Trying another concept to accomplish the competition requirements seems interesting and motivated the team. A proposed design with rotating rod is illustrated in Figure 6.20.

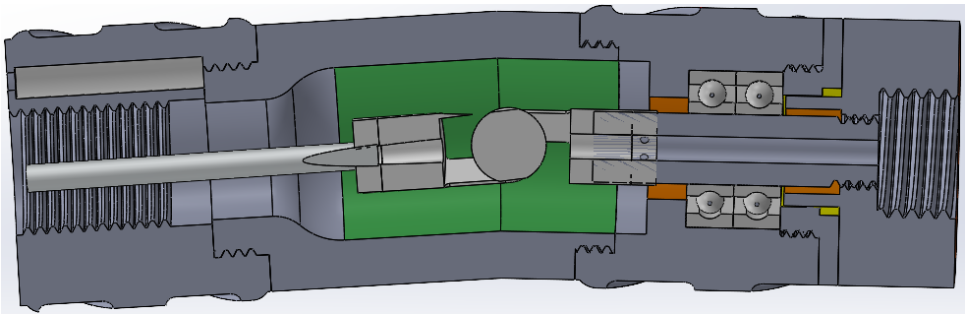

Figure 6.20: Concept of BHA with rotating rod.

6.4 Bottom Hole Assembly Design

The BHA design is key for a rotary system's function, and therefore highly prioritized in this year's project as directional drilling is a part of this years contest. The BHA is made up of a bit sub, bearings, a drive shaft, a bent housing, stabilizers, and an universal joint. This section will present the different parts, as well as bit design and further plans on that matter.

6.4.1 Stabilizers and Sensor Sub

The BHA design from last year consisted of two stabilizers, one near-bit, lower stabilizer, and one upper stabilizer located at the top of the BHA. Stabilizers are meant to reduce vibrations, stabilize drill string and bit, and ensure directional control [3].

The upper stabilizer houses the sensor card in a socket as shown in Figure 6.21b. This stabilizer is the uppermost part of the BHA and will from now on be referred to as sensor sub. In addition to housing the sensor card, the sensor sub will serve as a connection between the BHA

and the DP. The lower stabilizer is the lowermost part of the BHA and is located below the bent sub, making sure directional control is intact. The stabilizers are made up of thick walled steel and will therefore unlikely be damaged during normal drilling. The sensor sub is the weakest out of the two, since the sensor socket takes up a lot of space in the wall, hence this stabilizer is most likely the one to fail if such an incident were to occur.

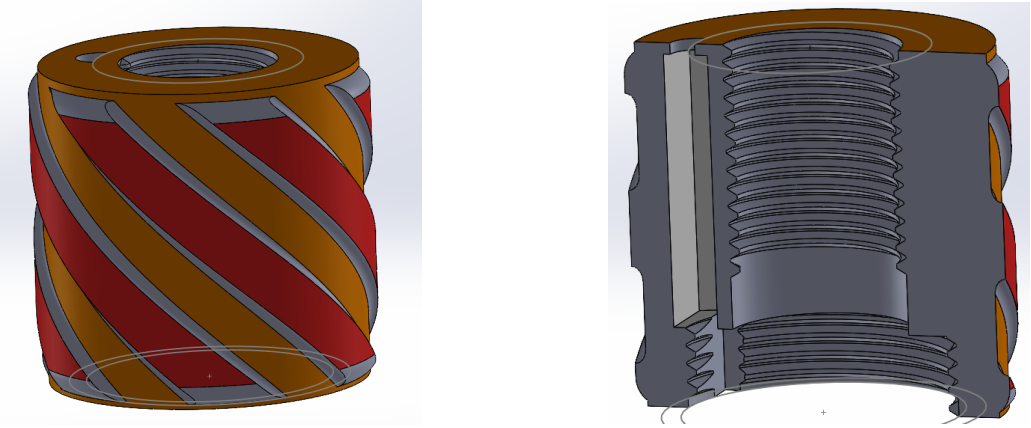

(a) Upper stabilizer. **(b)** Cross-section of upper stabilizer.

Figure 6.21: Upper stabilizer housing the sensor card.

The stabilizer design from the previous team has proven to work as intended, and there is no reason not to build a stabilizer design upon the previous work. An improvement made, is to design thicker walls and threads, hence reducing risk of fracturing or breaking the equipment. A challenge with last year's design was that the cables had to be pulled through the lower end of the sensor sub, making the sensor card potentially exposed to water and hard to install and remove. This year the electric swivel will be removed and pulling electric cables on the inside of the DP will not be necessary. Another challenge with pulling the cables through the DP is the rotating rod occupying a lot of space and slamming against the walls as a result of vibrations. For these reasons the electric conductors will be pulled in a spiral shape around the outside of the DP. This improves the sensor sub design by pulling cables out of the top of the stabilizer instead of through it.

6.4.2 Bent Housing

The bent housing is located between the two stabilizers. The bent sub will have a fixed angle based upon the maximum dogleg severity required to meet the requirements. As calculated in section 8.3.4 the maximum required bit tilt will be 4.57°.

The bent housing will also house the transmission section, consisting of a universal joint. Torque and RPM will be transmitted from the top drive, through the aluminum rod and transmission section, towards the bit. The transmission section will be made up of a single universal

joint. As with the sensor sub, the overall size of the bent housing has been increased in radial direction. This is mainly to increase strength of threads as they have proven to be to weak. The proposed bent housing design is shown in Figure 6.22.

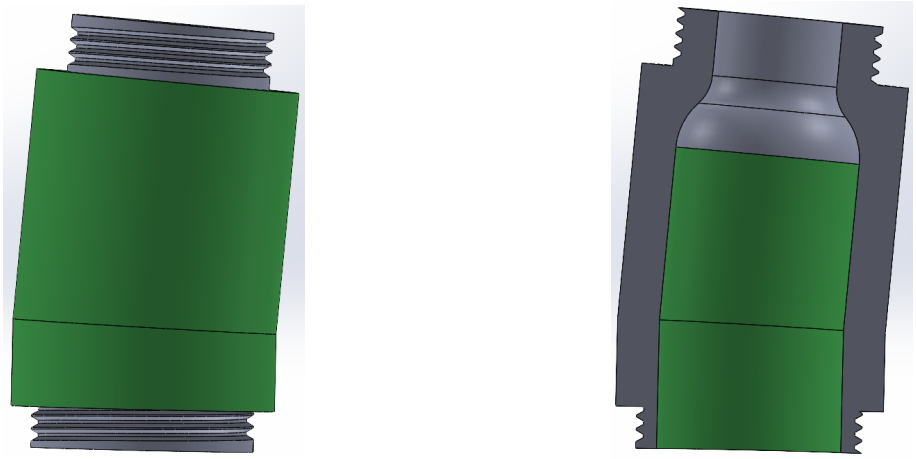

(a) Bent housing.

(b) Cross-section of bent housing.

Figure 6.22: Proposed bent housing design with an angle of 4.57 °.

6.4.3 Bearing Section

The bearing section houses the drive shaft and the bearing assembly. The drive shaft transfers torque and RPM from the universal joint to the bit sub where the drill bit is directly connected. The bearing assembly, as explained in section 5.2.5, consists of a set of radial bearings. These bearings are held in place by a bearing packer. The radial bearings are located inside the near-bit stabilizer, such that this stabilizer acts as a protection. The axial bearings used last year proved to be hard to maintain. Sand accumulation turned out to be a huge problem, as the ball bearings were not able to rotate as a result of this. This is solved by having a metal-to-metal connection between the bearing housing and the bit sub. The bearing assembly is illustrated in Figure 6.23.

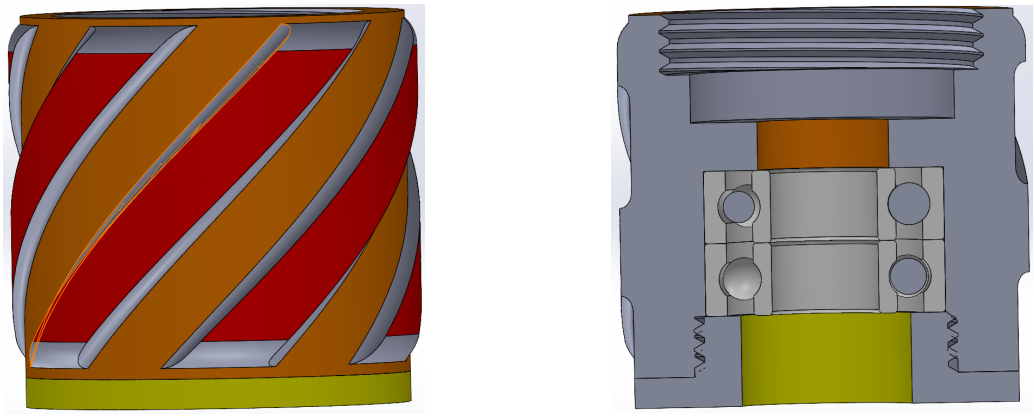

(a) Bearing assembly.

(b) Cross-section of bearing assembly

Figure 6.23: Lower stabilizer with radial bearings held in place by bearing packer.

Drilling fluid flows through the drive shaft, as well as a small percentage flowing through the bearings for lubricating purposes as shown in Figure 5.10. Optimizing the life of the axial bearings is highly dependent on balancing the hydraulic downward force created by fluid flow with the upward force created by applying WOB [24].

6.4.4 Bit Sub

The bit sub will be the connection between the drill bit and the rotating system. It will be connected to the drillbit in one end and the rotating shaft in the other as shown in Figure 6.24. It will have direct contact with the bearing packer in the bearing assembly, and as a result of this it will be made in brass and lubricated to allow for rotation. The bit sub has been scaled up in both axial ad radial direction to strengthen the connections, as they have were to weak last year.

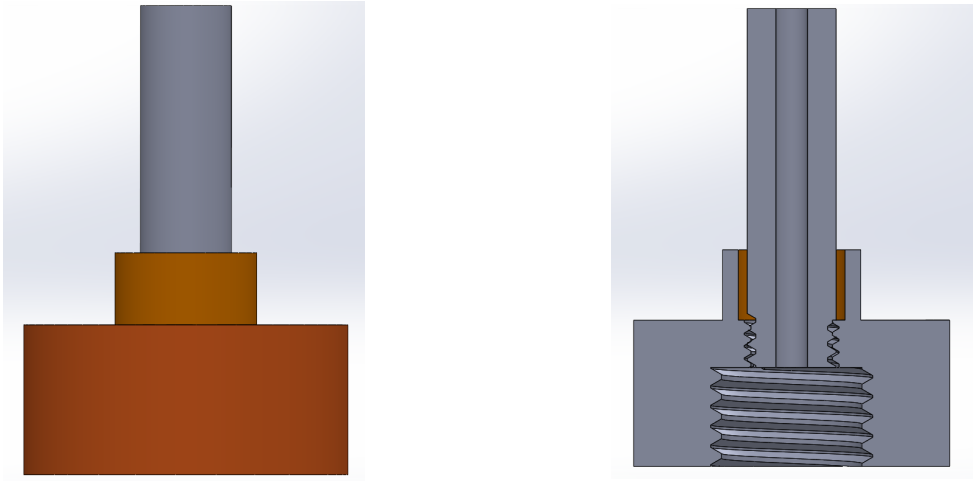

(a) Bit sub assembly.

(b) Cross-section of bit sub assembly.

Figure 6.24: Bit sub with drive shaft connected.

The final proposed BHA design with all the components is shown in Figure 6.25.

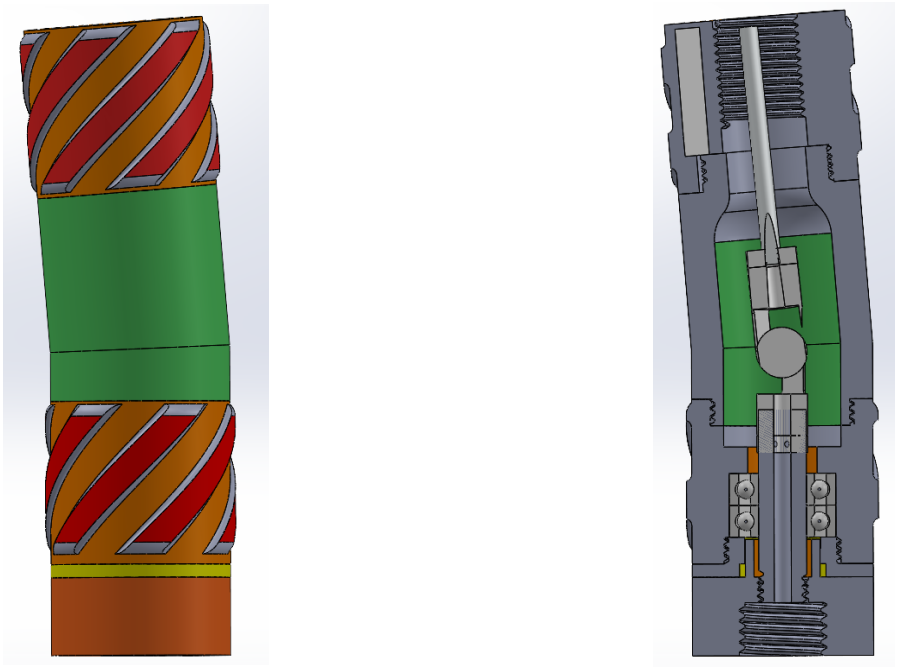

(a) Bottom hole assembly. **(b)** Cross-section of bottom hole assembly

Figure 6.25: Proposed design of bottom hole assembly.

6.5 Drill Bit

DSATS will provide a drill bit from Baker Hughes if desired. To make sure the best possible bit is utilized, multiple bits in addition to the provided one will be tested. The collaboration with Lyng Drilling from the last three years is continued and a NTNU drill bit design will be designed in Solidworks to later be proposed to Lyng Drilling. When approved and optimized, the bit will be produced by Lyng. This design process is beneficial because it allows for optimization of a drill bit with respect to the competition requirements. The goal is to design two different bits with different gauge properties. In addition to the provided bit and the designed bit from Lyng, two different drill bits from Alibaba has been ordered. In total eight bits with three of one type and five of the other type. Figure 6.26 shows the different bits. The first bit to the left is an Alibaba type 2 bit, the second and third bits are the old Lyng bits consisting of type 1 with long gauge pad and type 2 consisting of short gauge pad respectively, forth is the provided DSATS bit witout inserts, and the fifth bit is type 1 from Alibaba.

Figure 6.26: The 5 different bits. The two in blue from Lyng Drilling is 1.25" and represents how the new will look.

6.5.1 Steering and stability design considerations

The required well path to meet the competition requirements, will expose the bit to a lot of lateral and axial forces that can lead to a lateral deviation in the hole. B_s from Equation 6.1 is called bit steerability and reflects the potential the bit has to start a lateral deviation. D_{lat} is called lateral drillability and is defined as the lateral displacement per bit revolution. The same applies for axial drillability (D_{ax}) [45].

$$B_s = \frac{D_{lat}}{D_{ax}} \tag{6.1}$$

Whit respect to PDC bits the B_s factor is normally in the range of 0.001 to 0.1. To achieve a high B_s the D_{lat} needs to be high. D_{lat} is dependent on the gauge aggressiveness. A way to design the gauge aggressive is to choose back rake angles for the cutters on the gauge that ensures some side cutting action. A negative consequence of too low back rake angles might be ledges, spiraling and hourglass features along the borehole. One could say that the bit profile, active gauge and gauge pad is the most important steering design parts. These parts are in contact with the formation and are shown in Figure 6.27 [45].

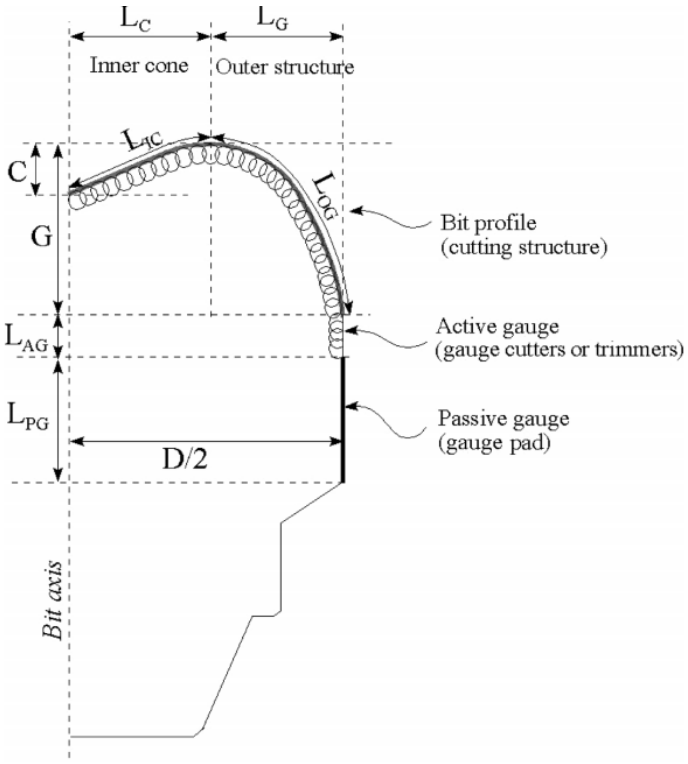

Figure 6.27: 2D drawing of PDC bit and the three important steering parameters bit profile, active gauge and passive gauge [45].

In addition to steerability, the bit should be stable. If bit stability is poor it might experience more vibrations. By decreasing the gauge length the steerability increases, but it reduces the stability. In other words, there is a trade-off between steerability and stability when deciding the length of the gauge. For this reason the team will design two drill bits with different gauge lengths to decide the optimal properties with respect to the competition. In addition to the gauge length, a deep cone angle will be positive for the bit stability as mentioned in section 5.4.1.

6.5.2 Drill Bit Specifications

The bit provided by DSATS is a generic directional PDC micro-bit from Baker Hughes. The OD will be 1.5 in. and it will be possible to insert tungsten carbide elements on the gauge pads and bit face. The lyng bits will also have an 1.5 in. OD and the properties will be scaled up from the 1.25 in. OD designs from previous years. The two Alibaba bits will have an 1.5 in. od and two blades. The main difference on the the two bits from Alibaba is that type 2 has one and a half PDC cutters on each blade while type 1 has one pdc cutter on each blade. The bit specifications are found in Table 6.1. Changes in the bit specifications may occur in phase II due to feedback from Lyng Drilling or other uncertainties.

Table 6.1: Bit specifications for different bits.

Bit type	DSATS bit	Lyng bit 1	Lyng bit 2	Alibaba bit 1	Alibaba bit 2
Bit Diameter	1.5”	1.5”	1.5”	1.5”	1.5”
Length	1.35”	1.56”	1.56”	1.5”	1.5”
Blade number	4	4	4	2	2
Cutter number	4	12	12	2	1.5x2
Cutter diameter	0.323”	0.236”	0.236”	0.532”	0.532”
TSP inserts	0	3	0	0	0
TC inserts	5	0	0	0	0
Nozzles	4	4	4	1	1

6.6 Downhole Power Output

6.6.1 EMM Power Output and Specifications

The main design, being the rotating rod inside the drillpipe, requires a back-up solution in case it does not work out as intended. As a temporary solution to this, an EMM has been chosen as power source in the BHA as introduced in section 6.3. To decide what type of EMM to utilize, it is important to take into account the space constraints in the BHA. Calculations to decide size and specifications are done below, but is subject to change during the project development.

Given a bit diameter of $1.5” = 38.1mm$, the width of the EMM has to be limited within this diameter to avoid a stuck BHA. The stabilizers will have a 2mm shorter OD than the bit, and the pads on the stabilizers will have a width of 1mm resulting in a diameter of 1mm x2 = 2mm. With these size reductions, the OD of the EMM housing can be given as:

$$\begin{aligned} OD_{housing} &= D_{bit} - \Delta D_{bit-stabilizer} - D_{pads} \\ OD_{housing} &= 38.1 - 2 - 2 = 34.1mm \end{aligned} \tag{6.2}$$

By picking a DCX 26 L Graphite Brushes, DC motor Ø26 mm motor, it leaves a housing thickness of 34.1-26 = 8.1mm. This thickness should both protect the EMM and divert water flow downhole.

The data sheet for the chosen EMM can be found in Appendix G. With its voltage of 48 V, it can provide a nominal RPM of 9370. By combining this motor with a gear with a reduc-

tion ratio of 1:138, the following performance can be expected.

The reduction ratio of the gear will reduce the nominal RPM from 9730 to $\frac{9730}{138} = 70RPM$. The torque on the other hand will increase from 59.1 mNm to $59.1 \cdot 10^{-3} \cdot 138 = 8.2Nm$. With a motor efficiency of $\eta_{emm} = 91\%$ and a gear efficiency of $\eta_{gear} = 60\%$, the maximum torque output possible is $8.2 \cdot 0.91 \cdot 0.6 = 4.5Nm$. These estimates of RPM and torque meets the requirements calculated in section 8.3.2.

7 Hydraulic Design

A drilling process in general is dependent on a customized hydraulic system to meet the required drilling parameters. This section will present the modifications done to the hydraulic system from previous years. The current drilling concept does not involve a PDM to rotate the drill bit and the hydraulic system will therefore not be of such an importance as in past competitions. The previous rig system with the hydraulic components is shown in Figure 7.1 below. However, the team of 2020 did not implement the hydraulic system before the competition was cancelled, hence the original setup in Figure 7.1 is the 2019 setup [27].

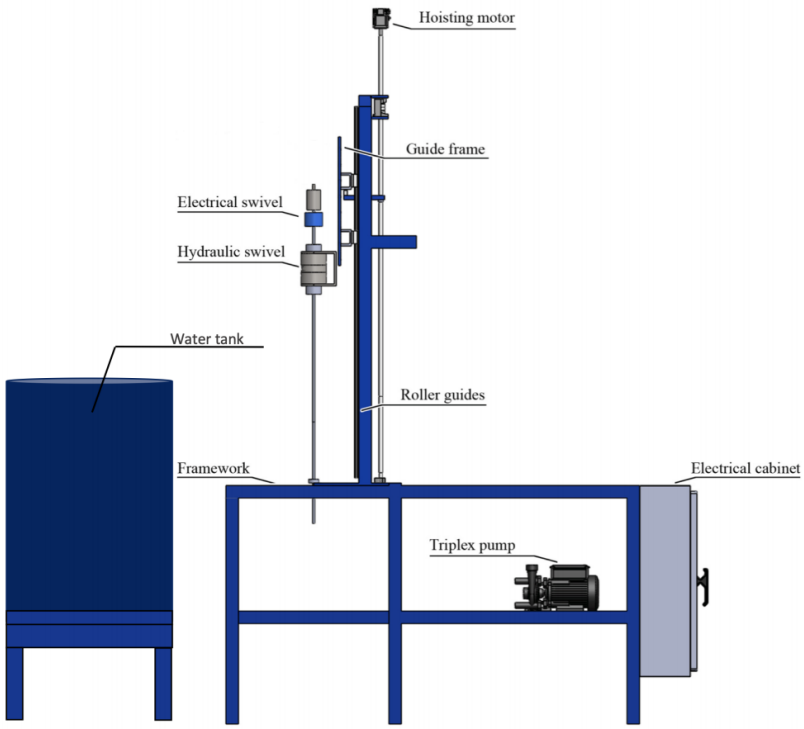

Figure 7.1: Original miniature rig from 2019 [5].

7.1 Water Supply and Fluid Flow

In full-scale drilling operations, it is the hydraulic system that powers the drilling bit. Because this rig uses a mechanical method to drill, the hydraulic system does not need pressurized fluid. The design has been modified accordingly. Instead of using a water tank and triplex pump to circulate the system, water will be supplied directly from a tap or similar on-site water supply through a quick-connect hose and in to a hydraulic swivel. This will provide the system with a constant flow of water. The fluid will enter the a swivel from the water hose connected to the side. From the hydraulic swivel, water is transferred down to the drill pipe, through the BHA and exiting the bit nozzles. Fluid will transport cuttings out of the borehole and flush out on the top of the rock sample. Water have previously been used as drilling fluid for all

NTNU teams, including the 2020 team. For this rig-scale, water has proved to be sufficient with regards to cuttings transportation, hole cleaning and system cooling. The system is not a closed circulating system because water and cuttings does not pose any hazards for the team or environment.The idea to change the drilling fluid from water to a chemical fluid was quickly abandoned because it would require a closed system for cuttings to be filtered out in order to re-use the fluid.

7.2 Hydraulic Swivel

The hydraulic swivel is a key component of the this years fluid system. The new drilling concept requires a swivel to circulate water down the drill pipe with the rotating rod inside it. The rod extends from the top drive, through a hollow gear box and down through the swivel. The drill pipe is connected to the bottom of the swivel. The rotational part of the swivel is connected to the drill pipe and has been designed to direct the water flow downwards while sealing around the rotating aluminum rod.

7.2.1 Fixed Housing

The housing of the hydraulic swivel is attached to a fixed steel plate. The steel plate is attached to the hositing system such that the swivel can follow its vertical motion. A set of bearings are located inside the housing in the top and bottom and are hold in place by two shafts. Figure 7.2 illustrates the housing of the hydraulic swivel. The design is similar to previous years except for the removal of the two channels for oil-based mud.

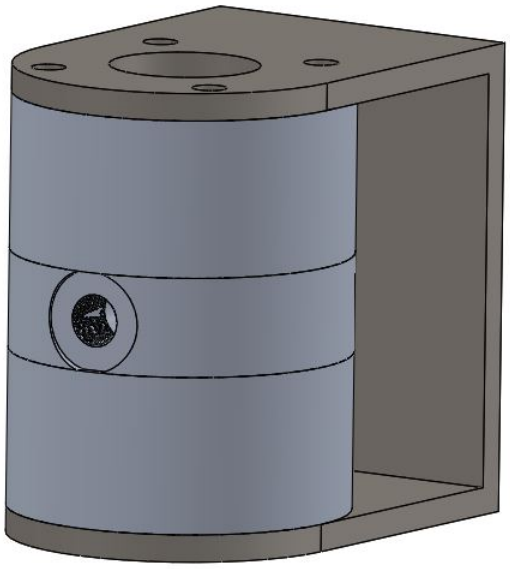

Figure 7.2: Hydraulic swivel housing

7.2.2 Rotating Swivel Shafts

The previously used shafts for electric cables was discarded because the cables for communication between the downhole sensor and computer will be installed beneath the swivel. A T-shaft, illustrated to the right i Figure 7.3, is connected to the gearbox above the swivel. Another shaft will be located inside the swivel housing and is connected to the T-shaft above it. The swivel design allows both shafts to rotate clockwise and counter-clockwise in order to control the azimuth. The azimuth rotation is provided by a motor attached to the gearbox from which the T-shaft is fixed to. Mounting the T-shaft beneath the suspended gearbox allows for easy inspection of the sealings on the inside of the T-shaft from above the hollow gearbox. This method also places a potential leakage further away from the gearbox, which has an IP-grade of 40, i.e. only protected against larger particles and not water. Both shafts are hollow so that the rod powering the drill bit can rotate inside the swivel. All threads in the swivel must be designed to avoid the parts from disassembling when rotating counter-clockwise.

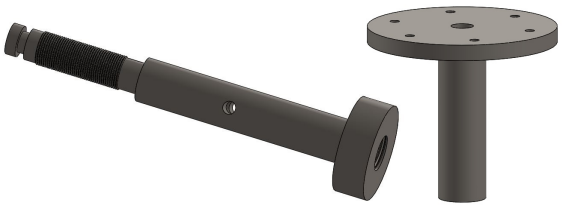

Figure 7.3: Hollow swivel shafts that can rotate inside the swivel housing.

The swivel housing has a hole in the front where a water hose can be connected. The rotating shaft allows the water to flow from the housing and into the shaft and down the drill pipe below. O-rings inside the T-shaft ensures that water only flows downwards even though there is a rotating rod inside. The location of this sealing is desirable to be as far away from the gearbox as possible. However, a plastic plate will be installed above the hydraulic swivel to protect the gear box from water damage.

8 Design Limits and Uncertainties

Design limits and uncertainties of this system is calculated in this section using the parameters presented in Table 8.1. The values are scaled up compared to previous designs from NTNU in order to meet the requirements of this year's competition.

Table 8.1: Relevant parameters.

Variable	Symbol	Value	Unit
OD DP	OD_{DP}	9.525	mm
Wall Thickness	t_{DP}	1.24	mm
Length DP	L_{DP}	91.44	cm
Diameter Rod	d	3.5	mm
Length Rod	L_{rod}	1.5	m
Elasticity Modulus (Stainless Steel, AISI316) [16]	E	200	GPa
Elasticity Modulus (Aluminium 6061-T6) [11]	E	68.9	GPa
Elasticity Modulus (Aluminium 7075-T6) [12]	E	71.7	GPa
Elasticity Modulus (Beryllium Copper UNS C17200) [38]	E	125	GPa
Material Yield Strength[1][16]	σ_{ys}	196	MPa
Material Yield Strength[2][11]	σ_{ys}	276	MPa
Material Yield Strength[3][12]	σ_{ys}	503	MPa
Material Yield Strength[4][38]	σ_{ys}	965	MPa
Fatigue Strength[5] (Aluminum 7075-T6) [12]	σ_{ys}	159	MPa
OD BHA	OD_{BHA}	36.07	mm
ID BHA	ID_{BHA}	26.42	mm
Length BHA	L_{BHA}	120.14	mm
ID Swivel + Hose	$ID_{Swivel+Hose}$	11.94	mm
Length Swivel + Hose	$L_{Swivel+Hose}$	2.50	m
Fluid Density	ρ_f	1000	kg/m^3
Solid Density	ρ_s	2650	kg/m^3
Fluid Viscosity	μ_f	1	cP

[1] Stainless Steel, AISI316
[2] Aluminium 6061-T6
[3] Aluminium 7075-T6
[4] Beryllium Copper UNS C17200
[5] 5000,000,000 cycles completely reserved stress

8.1 Well Path

The objectives for the well path that this years competition requires are similar to the previous year and are provided in the guidelines appendix [52]. The team is participating in group B, developing a mechanical rig. The objectives are:

- *Hit one or more targets at one or more vertical depth(s) and X/Y coordinates.*
- *For the Group B competition, the starting directional plan to hit the targets will not require wellbore inclinations in excess of 30° from vertical, 15° change in azimuth, or 10" displacement (departure from the vertical axis at well center). The max displacement/inclination/azimuth are total/accumulated from the start to the end of the well path.*

Interpreting the guidelines, there will be a requirement of a maximum 30° inclination from vertical or 25.4cm (10 in) horizontal displacement. To determine the limiting factor, further examination has to be conducted. The dimensions of the competition rock sample are 12in x 24in x 24in. A pilot hole has to be drilled in advance and shall not be less than 10.16 cm (4 in.) long in the vertical direction before starting to build inclination. Figure 8.1a illustrates this requirement.

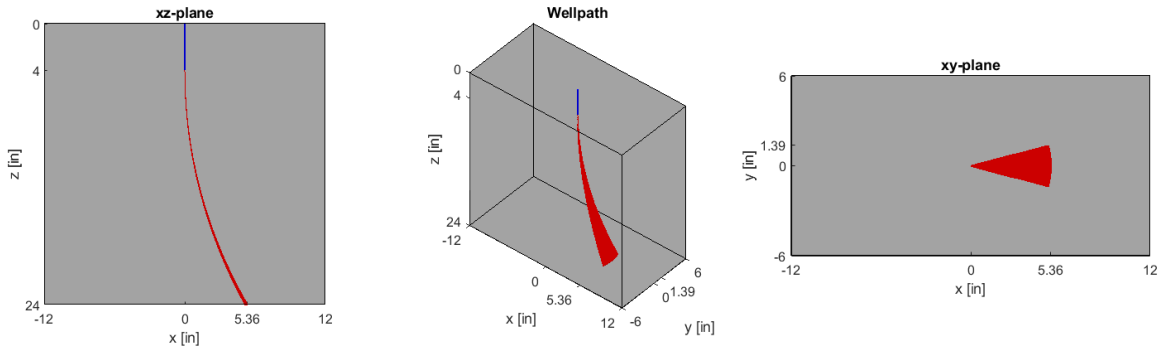

(a) Well path in xz-plane. **(b)** 3D-view of well path. **(c)** Well path in xy-plane.

Figure 8.1: Theoretical possible well path inside given rock dimensions, 12in x 24in x 24in.

The possible well path within the design limits is shown in Figure 8.1, assuming constant build up rate. From Figure 8.1a it is illustrated that an exit-angle of 30° will result in a maximum vertical displacement of 13.61cm (5.36 in) in x-direction and 3.53cm (1.39in) in y-direction.

8.2 Drill Pipe and Rotating Rod

There are multiple factors and design parameters influencing the choice of Drill Pipe (DP) and rod material such as bending, rotation and pressure. Careful considerations and calculations has to be conducted to ensure the best choice of material to withstand the applied forces in the system. The guidelines allows for use of either stainless steel or aluminum as drill pipe material.

8.2.1 Pipe Bending

Ensuring that the drill pipe operates within its elastic limits is crucial in order to hit multiple targets at different coordinates in the {X,Y} plan. Pipe bending is a results from axial stresses and the transition between elastic and plastic zone is where the total axial stresses equals the yield strength of the material chosen. Therefore, it is important to keep the total axial stresses acting on the pipe abundantly lower than the yield strength of the material.

Because there are two possible materials to choose from; stainless steel or aluminum, it is necessary to investigate the differences between them. Teams of previous years at NTNU have compared *stainless steel grade 316* with *aluminum 6061-T6* and the differences are illustrated in Figure 8.2 and 8.3. The total axial stress is calculated using Equation 5.18, 5.19 and 5.20, and the results are plotted in Figure 8.2 with input parameters from Table 8.1.

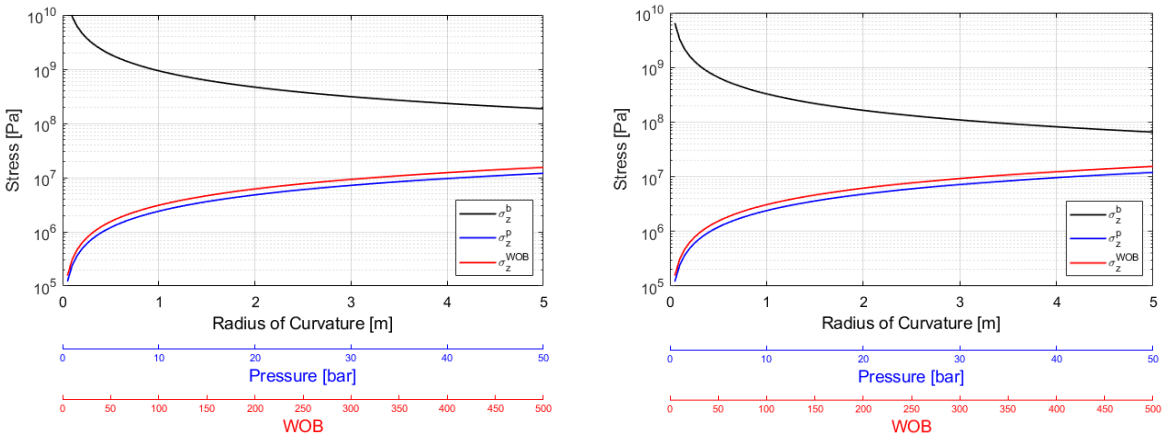

(a) Stainless steel, grade 316.

(b) Aluminum 6061-T6.

Figure 8.2: Axial stresses on pipe for different values of *RC*, *P*, and *WOB*.

Illustrated in Figure 8.2, the axial stress from bending is significantly greater than the contribution from pressure and WOB for both materials. The minimum allowable Radius of Curvature (RC) for drill pipe within the limits of elastic zone is attained by comparing the axial stress contribution from bending with the material yield strength.

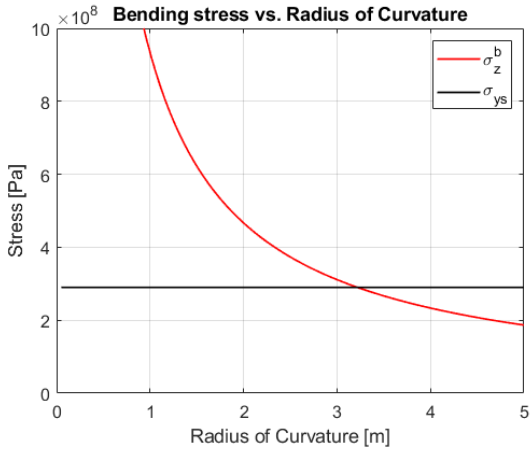

(a) Stainless steel, grade 316.

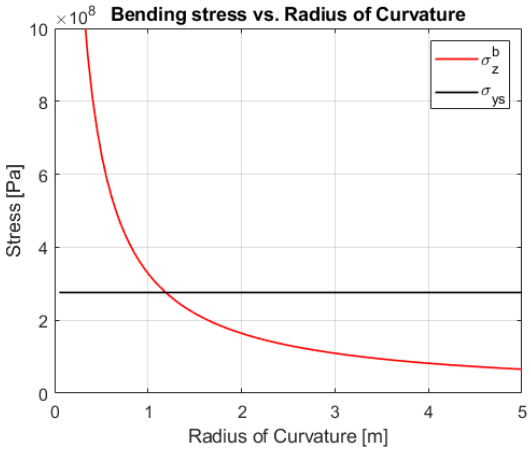

(b) Aluminum 6061-T6.

Figure 8.3: Contribution of axial stress from bending illustrated for different values of *RC* compared with material yield strength.

Figure 8.3a shows that the minimum allowable RC to keep a pipe of stainless steel within the elastic zone is 3.23m (10.6 ft.) which will result in a horizontal displacement of 3.99 cm (1.57 in.). However, utilizing an aluminum drill pipe, it is possible to obtain a minimum RC of 1.19m (3.9 ft.) resulting in a displacement of 11.38 cm (4.48 in.). This is illustrated in Figure 8.3b. Because aluminum drill pipe gives superior performance, stainless steel 316 drill pipe is ruled out. However, the performance of the aluminum 6061-T6 drill pipe is not sufficient to meet the requirements obtained in section 8.1. Therefore, another aluminum alloy has been considered as drill pipe material in order to achieve the sufficient inclination and horizontal displacement. Figure 8.4 illustrates the axial stresses and performance of a *aluminum 7075-T6* drill pipe.

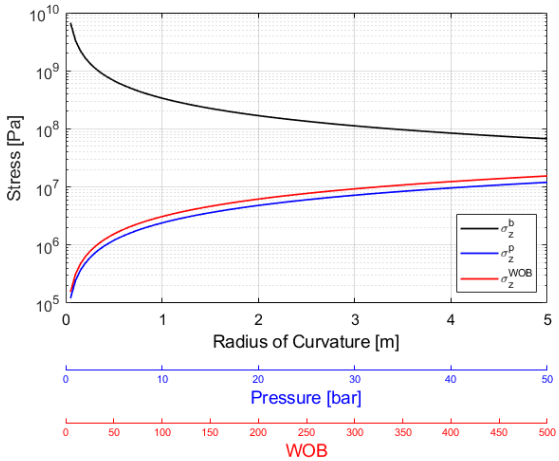

(a) Axial stresses on pipe for different values of *RC*, *P*, and *WOB*.

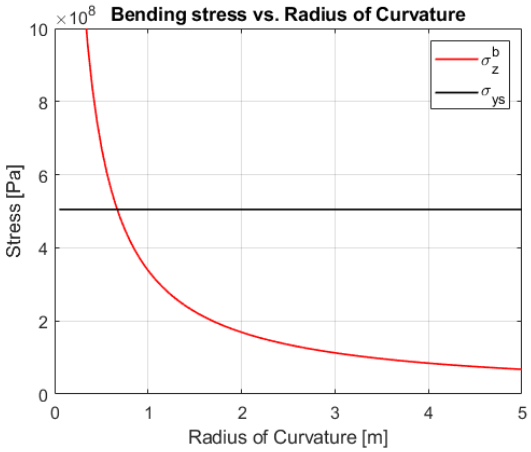

(b) Axial stress from bending for different values of *RC*, compared with material yield strength.

Figure 8.4: Performance of aluminum 7075-T6 drill pipe.

From Figure 8.4a, which illustrates the axial stress from WOB and pressure, it is still negligible compared to axial stress from bending. As shown in Figure 8.4b, the minimum allowable RC for this aluminum alloy is 0.76 m (2.49ft.). This will result in a horizontal displacement of 23.14 cm (9.11 in.) which is greater than the requirement of 13.61 cm (5.36 in.).

The displacement of 13.61 cm (5.36 in.) will result in a RC of 1.02m (3.35 ft). The axial stress from bending at this RC is 334 MPa (48.44 ksi), in which yields a safety factor of $\frac{505}{505-344} = 3.14$. Based on these examinations, a drill pipe of material Aluminum 7075-T6 is chosen.

8.2.2 Rod Stresses

In theory, the rotating rod inside the drill pipe will only experience axial stress from bending and shear stress from rotational torque and those will be the limiting factors. The stresses are calculated by Equation 5.21 and 5.22 with input values from Table 8.1. To better illustrate the effect the stresses have on the rod, they are calculated as a comparative stress with Equation 5.23. Figure 8.5 shows the results for different materials.

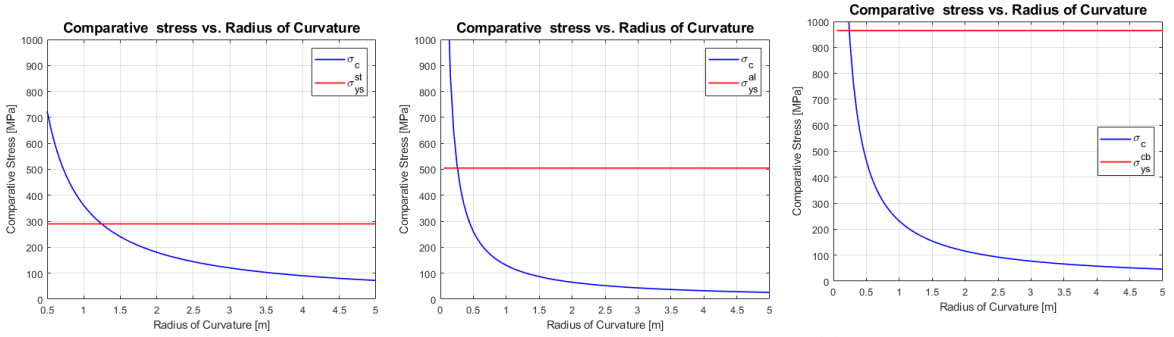

(a) Stainless Steel, grade 316. **(b)** Aluminum 7075-T6. **(c)** Cobber Beryllium UNS C17200.

Figure 8.5: Comparative stress from bending and twisting for different values of *RC* compared with material yield strength.

Figure 8.5 shows the comparison of three different materials performance. Both an aluminum rod and copper beryllium rod will meet the requirement of this years competition. Using a stainless steel rod however, does not provide sufficient performance needed for this system. In addition, the copper beryllium alloy proved to be expensive and difficult to acquire. Therefore, the choice of material for the rotating rod is *Aluminum 7075-T6*, same as drill pipe.

8.2.3 Buckling

Critical buckling limit of the drill pipe is estimated with Equation 5.6 and 5.10. Because WOB is only subjected onto the drill pipe, the rod will not experience buckling effects. The drill pipe

has a diameter of 9.525 mm (3/8 in.) and wall thickness of 1.2446 mm (0.049in.) according to the guidelines, and calculations are performed w.r.t. to this requirement [52]. Table 5.1 present the possible end conditions with effective length factors (K) and Figure 8.6 shows the critical Weight On Bit (WOB) for different K values. The most representative end condition for the drill pipe will depend on which part of the system is described. For simplicity, the drill pipe is separated into three isolated sections from top to bottom: The length above the drill floor, the length between the drill floor and the riser and the length between the riser and the Bottom Hole Assembly (BHA).

Because the drill pipe is fixed against radial movement, the two uppermost sections of the drill pipe will resemble a fixed-fixed scenario. The top section is fixed between the top drive connection and the drill floor stabilizer. The middle section is fixed between the drill floor stabilizer and the riser stabilizer. The lower section can be represented by a K value between fixed-free and fixed-pinned end conditions. It is conservative to estimate buckling limit as a fixed-free situation as the borehole wall will support the drill pipe when displacing in the horizontal plane. Therefore, it is more representative to investigate buckling at fixed-pinned for the lower section.

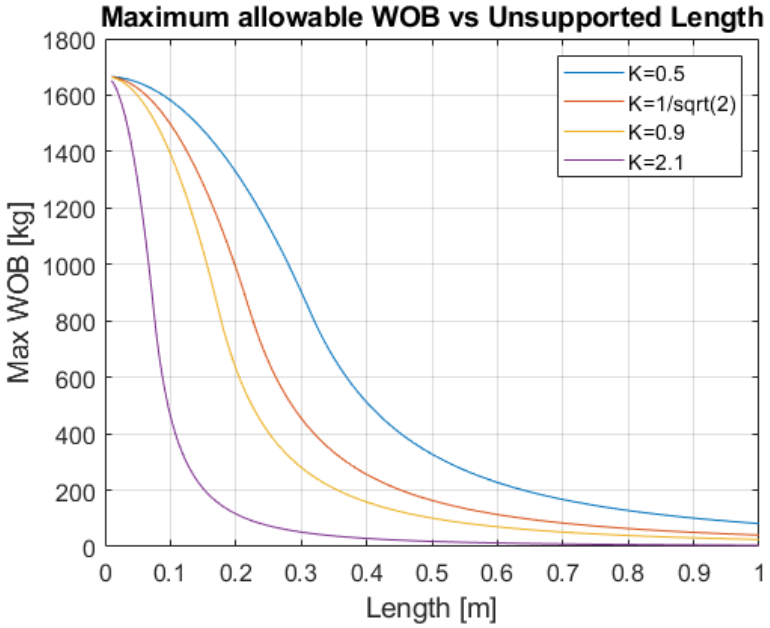

Figure 8.6: Buckling limit calculations for Aluminium DP.

Calculated results are presented in Table 8.2 and shows maximum WOB for the intended unsupported pipe lengths. Clearly, a fully unsupported pipe is not desirable because it will limit the maximum WOB to 5.6 kg (12.32 lbs). This demonstrates the necessity of stabilizers in order to limit the unsupported pipe length. The calculations for fixed-free situation will not be representative for real life drilling operations because the borehole will support the pipe and

the actual limit will thus be larger than the one presented in the far-right column. Additionally, the BHA will occupy a significant length of the hole, which further reduce the length of unsupported drill pipe.

Table 8.2: Buckling calculations for drill pipe.

		Fixed-Fixed		**Fixed-Pinned**		**Fixed-Free**
	K	0.5	0.9	$\frac{1}{\sqrt{2}} = 0.71$	0.9	2.1
	L [m]	**Maximum WOB [kg]**				
Drill pipe length	0.91	97.9	30.2	49.0	30.2	5.6
Rock height	0.61	220.3	68.0	110.2	68.0	12.5
Curved section	0.51	317.3	97.9	158.6	97.9	18.0
Length of pipe	0.3	878.7	272.0	440.7	272.0	50.0

As shown in Table 8.3, the WOB limit is increased when a BHA length of 16.2 cm (6.38 in.) is taken into account.

At the end of the drilling operation, the WOB will be limited to approximately 38 kg (83.8 lbs) if a fixed-free situation is considered. This is a conservative measure because the BHA has stabilizers and the borehole wall will support the drill pipe. This conservative number will however give sufficient WOB to meet the time constraint calculated in section 8.3.2.

Table 8.3: Buckling calculations with BHA length of 16.2 cm (6.38 in.).

		Fixed-Fixed		**Fixed-Pinned**		**Fixed-Free**
	K	0.5	0.9	$\frac{1}{\sqrt{2}} = 0.71$	0.9	2.1
	L [m]	**Maximum WOB [kg]**				
Well length - BHA	0.45	404.3	124.8	202.2	124.8	22.9
Curved section - BHA	0.35	668.4	206.3	334.2	206.3	37.9

8.2.4 Burst

Burst pressure for a thin-walled drill pipe is calculated with Equation 5.13. The resulting burst pressure while drilling is attained by inserting the material yield strength of the aluminium drill pipe and its dimensions presented in Table 8.1. Because burst is calculated while drilling, a

Safety Factor (SF) of 3 is used.

$$P_{burst} = 2\frac{0.875 \cdot 505MPa \cdot 0.049in}{3/8in \cdot 3} = 385 \cdot 10^5 Pa \tag{8.1}$$

8.2.5 Twist-Off

Twist-off calculations are made to determine the applied torque limit on drill pipe and rod during drilling. Equation 5.14 and 5.15 are used to calculate the twist-off for drill pipe. σ_r (Equation 5.16), σ_θ (Equation 5.17) and σ_z (sum of Equation 5.18, 5.19 and 5.20) are used as input.

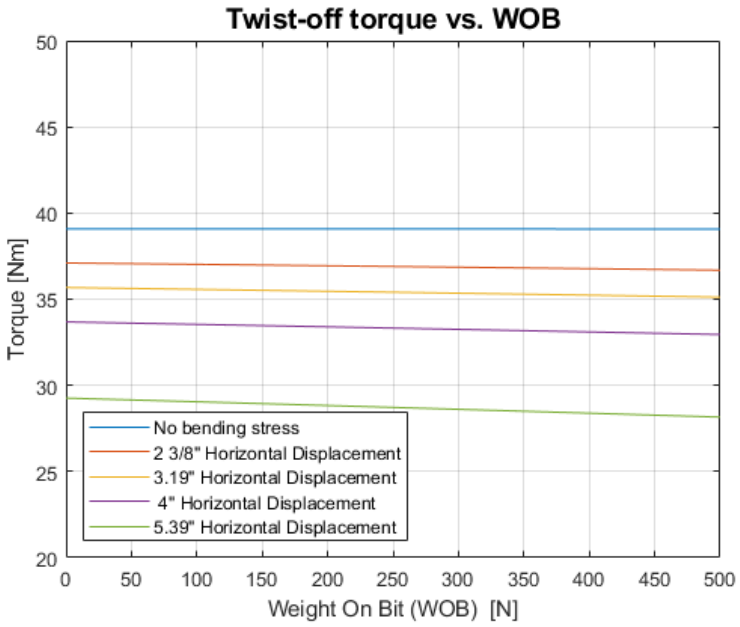

Figure 8.7: Twist-off torques on drill pipe for different bending cases and WOB.

Figure 8.7 shows the result of five twist-off calculations from no bending to maximum calculated horizontal displacement shown in Figure 8.1a. All stresses are calculated outside the pipe wall. Because the internal pressure of the drill pipe had a negligible effect on torque, it is calculated with a pressure of, $P = 100\ bar(1450psi)$. From Figure 8.7 the different torque limits can be extracted. These values are presented in Table 8.4 together with the same limits at 10 bar (145 psi), to illustrate the negligible difference.

Table 8.4: Twist-off limits for aluminum 7075-T6 drill pipe for different horizontal displacements.

Pressure	**Horizontal Displacement**				
	0”	**2 3/8”**	**3.19”**	**4”**	**5.39”**
10 bar	39.1-39.1 Nm	36.7-37.1 Nm	35.1-35.7 Nm	33.0-33.7 Nm	28.2-29.3 Nm
100 bar	39.1-39.1 Nm	36.7-37.1 Nm	35.1-35.7 Nm	33.0-33.7 Nm	28.2-29.3 Nm
Twist-off limit	***39.1 Nm***	***36.7 Nm***	***35.1 Nm***	***33.0 Nm***	***28.2 Nm***

Table 8.4 presented is the twist-off limit for the maximum horizontal displacement estimated in section 8.1 equal to 28.2 Nm (20.8 ft-lbs), which is sufficient. Twist-off calculation for the aluminum rod is straightforward because the angular and radial stresses equals to zero because of no internal pressure present. Radial stress will not be contributed by pressure and WOB because the rod will not experience any WOB. Therefore, the torque limit for the aluminum rod can be calculated directly using Equation 5.21 with τ_s being the shear strength of aluminum 7075-t6 alloy. This results in a twist-off limit of 2.8 Nm (2.06 ft-lbs). Compared to the required torque in section 8.3.2, this twist-off limit will be sufficient.

8.2.6 Fatigue

Fatigue has been experienced by previous teams from NTNU. Back in 2018 when there was only vertical drilling, the team experienced fatigue in terms of the pipe breaking as a result of twist-off at a much lower torque than expected from calculations and tests. With this years competition the pipe and rotating rod will also be subject to a significant bending stress. From the results in section 8.2.1, the bending stress of 344 MPa (49.89 ksi) at the curvature required to meet the competition specifications is more than twice the fatigue strength of the pipe. For the rotating rod, the stress experience is below the fatigue strength. In addition to this, the pipe will experience wear as a result of friction between pipe and wellbore. There will also be friction related wear between the pipe and the rotating rod, but this is minimized as a result of the two components being made up of the same material. These properties will be further tested in Phase II when the drill pipes and rods have arrived from the supplier.

8.3 Drilling Requirements

Selecting the components and equipment best suited for the performance of the rig is greatly dependent on the drilling requirements provided, especially with regards to powering the drill bit.

8.3.1 Required Drilling Rate

The drilling rate required is attained by assuming the least efficient well path, which in section 8.1 is found to be a displacement in the horizontal plane by 13.61cm (5.36 in). This displacement results in an RC of 1.02m (3.35ft) and an exit angle of 30°.

Setting RC = 1.02m, $I_1 = 0°$ and $I_2 = 30°$ in Equation 5.3 results in a CL of 53.2cm (20.94in). The maximum allowed time spent drilling in the competition is 3 hours [52]. When aiming for 2 hours, a sufficient safety factor is included when estimating the required ROP. These assumptions result in an average ROP of 0.443cm/min (0.174in/min) required to complete the task within the time constraint.

8.3.2 Torque & RPM

Because the previous NTNU team did not conduct any drilling tests, this years team base its calculations on data acquired from testing in 2019. These test will have to be done again in Phase II because the team have made significant changes to the rig. This however, will not have a significant impact on the torque and RPM. Table 8.5 presents data from test drilling in 2019.

Table 8.5: Test data from drilling. Constant top drive velocity with increasing WOB.

Run	Time [min]	RPM	WOB [N]	Torque diff. [Nm]	Avg. ROP [cm/min]	Sufficient ROP
1	0.35	68	98	0.22	0.23	No
2	0.36	68	108	0.21	0.29	No
3	0.30	68	118	0.20	0.26	No
4	0.44	68	127	0.21	0.37	No
5	0.64	68	137	0.21	0.31	No
6	0.64	68	147	0.21	0.67	Yes

The sixth run in Table 8.5 reached required ROP with 147N WOB and a RPM of 68. This run resulted in a torque diff. of 0.21 (0.16 ft-lbs)Nm, such that the BHA has to handle at least this value. Taken into account the fact that the bit will increase in size from this test run, it is reasonable to require the BHA to handle at least 0.7Nm (0.52 ft-lbs) and 70 RPM.

8.3.3 Pressure on ROP and Torque

The 2019 Drillbotics team from NTNU used a pump for the hydraulic system and thus risked a significant effect on ROP and torque as a result of high pressure. This was tested during one of the test runs where WOB and top drive velocity were kept constant at 98N and 50RPM

respectively. No effect on ROP could be observed, most probably because ROP is difficult to remain constant. On the other hand, torque appeared to increase with increased pump velocity [27]. This should not be a challenge this year because the hydraulic system is controlled by tap water and not by a pump. However, this will be tested during Phase II.

8.3.4 Bit Tilt

To achieve a the desired deviated well path, the tilt of the drill bit is essential and is achieved by a bent housing in the BHA. The fixed bent housing angle has to be decided before manufacturing the component.

Dogleg severity is calculated using Equation 5.1 with ϕ = 30° and CL = 53.2cm as calculated in section 8.3.1. This will result in a DLS of 56.4°$/m$ (17.20 °$/ft$) and is used to calculate the bit tilt, θ with Equation 5.5.
With estimated lengths of the BHA, L_1 = 6.2cm (2.44 in.) and L_2 = 10cm (3.94 in.) illustrated in Figure 5.3, the maximum bit tilt angle required yields:

$$\theta = \frac{DLS(L_1 + L_2)}{2} = 4.57° \tag{8.2}$$

8.4 Drilling Hydraulics

The hydraulic system is essential in order to transport the rock cuttings out of the bore hole during drilling. Calculations related to the hydraulic system and its outputs is important to meet the requirements in the competition.

8.4.1 Hole Cleaning

Water from tap is used to flush the bore hole and therefore calculations are done with respect to hole cleaning being done with water as drilling fluid. For simplicity, the cuttings from the drilling process are assumed to be spherical.

Data acquired from previous years shows that the diameter of the cutting particles were assumed to be 2 mm (0.079 in.) in 2018 and 2019 [27]. Because the team in 2019 increased the bit diameter, the cutting diameter increased with 0.2mm from 2018 to 2019. A reasonable assumption would be to increase cutting diameter with additional 0.2mm this year as well, as a result of the further increase in bit diameter. Further calculations will therefore be done with a maximum cutting diameter of d_s = 2.4 mm (0.095 in.), but will be investigated further during Phase II. According to the guidelines, [52], the rock sample will be a in-homogeneous rock sample with different layers different densities. In Phase I, the team has assumed a cutting density of 2650kg/m^3. These parameters as well as others are listed in Table 8.1.

Table 8.6: Results of Hole Cleaning Calculations.

Parameters	Equations	BHA	DP
v_{sl} $[m/s^2]$	Equation 5.24	5.18	5.18
Re	Equation B.7	10525 (Turbulent)	148000 (Turbulent)
f	Figure 5.20	0.44	0.55
v_{sl} $[m/s^2]$	Equation 5.25	0.017	0.015
q [lpm]	Equation 5.26	0.24	1.93

Table 8.6 shows results from all calculations required to obtain the required flow rate value for sufficient hole cleaning. The flow rate is calculated with a transport ratio of 50%, which is the desired value to achieve. The required flow rate for sufficient hole cleaning is below 3 lpm (0.792 gpm) for the annulus outside both BHA and drill pipe.

8.4.2 Pressure Losses

To confirm whether or not the required flow rate for hole cleaning is sufficient, it is necessary to examine the pressure losses in the borehole. Equation 5.28 and Equation 5.33 is used to calculate the pressure drop in the system. Input for the equations is extracted from Table 8.1. The teams plan A is to use an aluminium rod with a diameter of 3.5 mm (0.138 in.). If the rod is not solid enough the team will try with aluminium and steel rod with a diameter of 4 mm (0.157 in.). The worst case for pressure losses is steel rod with 4 mm diameter. Therefore, this scenario is calculated and shown in Table 8.7. The worst case scenario with steel rod there is two different pipe roughness factors. ϵ_{dp} for the drill pipe is set to $1.3{\cdot}e^{-6}$. For the steel rod ϵ_{rod} it is set to $1.5{\cdot}e^{-5}$. These numbers are found in a table online [15]. Because there are two different roughness factors, it is necessary to use an estimation of the final ϵ_f. The approach is based on examination of the flow area percentage with respect to the surface area of the rod and the inside of the drill pipe. The flow area is calculated with Equation 8.3.

$$A_{flow} = 2\pi rh \tag{8.3}$$

Where A_{flow} is the flow area, r is the hydraulic radius of flow and h is the height of the drill string. The height, *h*, will be approximately equal for both rod and the drill pipe. Leaving *h* out of the formula for flow area yields the formula for the circumference of a circle. This formula yields that the fraction of flow around the rod is approximately 36.3% and the inside

of the drill pipe is 63.7%. The final ϵ_f to be used for the flow through the drill string will be $6.265 \cdot e^{-6}$. The results are presented in Table 8.7. The main pressure loss in the system will occur in the drill string because the rod is inside the drill pipe leaving a relative narrow area for fluid to flow. There will be a pressure loss of *2.514 bar (36.45 psi)* for the required flow of *3 lpm (0.792 gpm)*. This is not a problem because the pressure output of the tap is 7 bar (101.5 psi). For a flow of 5 lpm (1.32 gpm) the pressure drop will be approximately 7 bar which is the limit of the tap. For the two cases with an aluminium rod of diameter 4 and 3.5 mm (0.157 in. and 0.138 in.), the pressure drop for 3 lpm (0.792 gpm) is 2.340 bar (33.93psi) and 1.181 bar (17.12 psi), respectively.

Table 8.7: Pressure drop in bars for various flow rates and parts of the system.

Q[lpm]	ΔP_{dpi}	ΔP_{bhai}	ΔP_{dpann}	ΔP_{bhaann}	$\Delta P_{swivel+hose}$	ΔP_{nozzle}	ΔP_{tot}
1.5	0.604	3.618e-6	2.790e-6	4.111e-4	0.002	0.022	0.628
2	1.075	6.431e-6	4.851e-6	0.001	0.003	0.039	1.118
2.5	1.679	1.005e-5	7.580e-6	0.001	0.005	0.061	1.746
3	2.418	1.447e-5	1.091e-5	0.002	0.007	0.088	2.514
3.5	3.291	1.970e-5	1.486e-5	0.002	0.009	0.119	3.421
4	4.298	2.572e-5	1.941e-5	0.003	0.012	0.156	4.468
4.5	5.440	3.257e-5	2.456e-5	0.004	0.015	0.197	5.655
5	6.715	4.020e-5	3.032e-5	0.005	0.018	0.244	6.98

9 Electrical System and Instrumentation

To achieve an autonomous drilling rig, it is of great importance to have a capable electrical system and good communication between software and hardware. This section will cover the design taken from previous years, as well as the planned changes for this year's competition. The electrical system doesn't need to be changed according to the new guidelines given this year, but the new concept suggested by this years team requires a few changes for best possible functionality.

9.1 Hoisting System

The hoisting system will be made up of the same components as previously. with a main function of hoisting the rotary drilling system in a vertical direction. Hoisting the system down will apply Weight On Bit (WOB), and together with Revolutions Per Minute (RPM) this will result in a Rate of Penetration (ROP). A ball screw driven by an AC motor hoists the system up and down. A load cell is connected to the lower end of the ball screw, and is used to measure the WOB. The hoisting system is illustrated in Figure 9.1. The two most complicated, technical, and important parts of the system is the hoisting motor and the load cell.

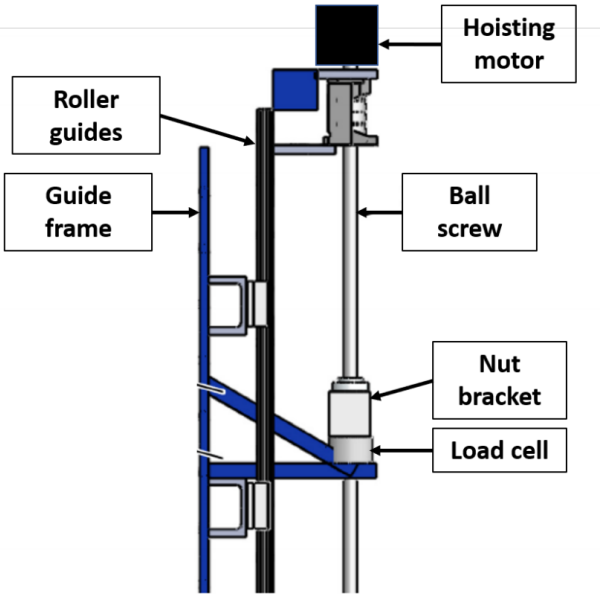

Figure 9.1: Hoisting system with components and their locations [47].

9.1.1 Hoisting Motor

The motor is unchanged from previous years. The motor is of type GST03-2M VBR 063C42 by Lenze and is powered by a motor drive of type E84AVTCE7512SX0. The gear ratio between the motor RPM and ballscrew RPM has previously been estimated to be around 1:9 [48]. The

motor has a maximum RPM of 3400, maximum output power of 0.75kW, and a maximum output torque of 45Nm [37]. The motor and driver has real-time measurements of motor states such as RPM, torque, and absolute position.

Figure 9.2: Hoisting motor from Lenze.

9.1.2 Load Cell

The load cell will be reused as it has been the last years, as it has proven to perform great. It is a TC4-AMP transducer by APE Transducer [61], and is visualized in Figure 9.3. As illustrated in Figure 9.1, the load cell is mounted between the nut bracket and the rig frame. This cell can measure the WOB by measuring the normal force propagating through the rotary system and ball screw when the drill bit tags the rock. The measured force can be presented as an output of voltage or current. Voltage seems like the better option out of the two for this case, since the travel distance of the signal is relatively small. The load cell is capable of voltage outputs between $[-10V, 10V]$, which converts to force measurements between $[-2500N, 2500N]$. The expected values from the drilling rig is well within this region of measurements. The measured force can be translated into WOB kg by Equation 9.1.

$$WOB = V\frac{F_2 - F_1}{g(V_2 - V_1)} - m_{offset} \tag{9.1}$$

Where V is the measured voltage, F_2 and F_1 are the maximum and minimum forces given by the range of the cell (*2500N* and *-2500N* respectively), V_2 and V_1 are the maximum and minimum voltages possible (*10V* and *-10V* respectively), and m_{offset} is a constant to cancel out the rotary system weight. With these measurements, the drill bit position can be estimated with by utilizing a Kalman filter and the orientational measurements from the IMU.

Figure 9.3: Load cell: TC4-AMP transducer by APE Transducer [61].

9.1.3 Pressure Transmitter

The system has a pressure sensor of the type PCE-28 by Aplisens A-S [6]. The sensor readings are less important than previous years as the water is only used for hole cleaning. The sensor is included to check for sufficient water flow throughout the drilling operation and detecting pump failure.

The sensor outputs current in the rang 4-20mA or voltage in the range 0-10V. The sensor can measure pressures in the range 0-100bar. The pressure is calculated from the current output of the sensor.

$$P = \frac{(I - I_{min})(P_{max} - P_{min})}{I_{max} - I_{min}} - P_{offset} \tag{9.2}$$

Where I is the output current, I_{max} and I_{min} are the maximum and minimum current outputs, P_{max} and P_{min} are the maximum and minimum measurable pressure, and P_{offset} is used for calibration.

9.2 Rotary System

Replacement of the PDM requires modifications to the existing rotary system. The bit rotation is now provided by a top drive motor in the new concept.

9.2.1 Top Drive Motor

The top drive motor from last year is replaced with an equivalent motor to the hoisting system. The previous top drive motor was replaced as the automation protocol limited the overall sampling frequency of the system and the motor had insufficient torque for some research experiments. The motor was acquired by a previous Drillbotics team but not integrated.

9.3 Azimuth Control System

This years concept has a azimuth control system. The system rotates the drill pipe such that the direction on the bent BHA can be controlled. A servo motor is connected to a hollow shaft gearbox with a 30:1 ratio.

9.3.1 Azimuth Control Motor

The motor connected to the gearbox is of type Moons SM0402AE4-KCD-NNV with a M2DV-1D82IP driver. The motor has an output power of 100W, rated speed of 3000RPM, and peak torque of 0.93Nm [46]. The motor relies on the high gear ratio of the hollow shaft gearbox to rotate the drill pipe. The motor has real-time measurements of RPM, torque, and position.

Figure 9.4: Azimuth control motor connected to the hollow shaft gearbox.

9.4 DAQ

Some of the sensor measurements values are transferred as a voltage or current signal. These values are then read by the DAQ so that the values can be used in the control system. The DAQ is of the type USB-6212 made by National Instruments. The DAQ has 16 analog inputs with a 16 bit measurement resolution. The maximum sampling frequency is 400kS/s. There are 2 analog outputs with a maximum update frequency of 250kS/s [32].

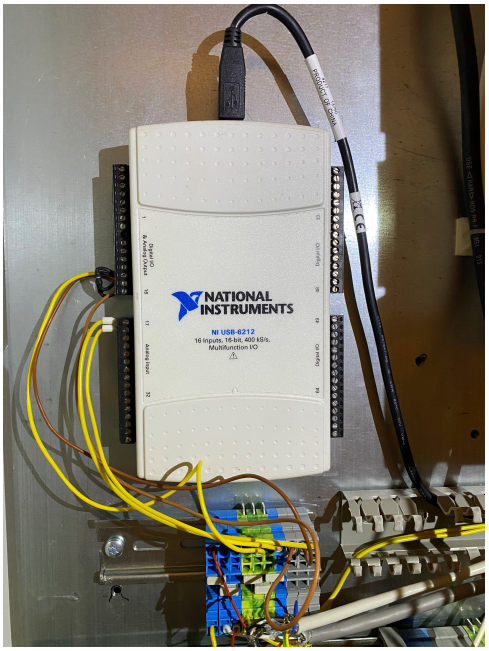

Figure 9.5: DAQ from National Instruments.

9.5 Sensor Card and Communication

The downhole IMU sensor card was developed by the 2018/2019 team [48]. A custom design was chosen due to size requirements to fit inside the BHA while allowing water flow to the PDM motor. Off-the-shelf IMU sensors small enough to fit inside the BHA with the required feature set proved difficult to find. The IMU chip has a microcontroller sampling data from the IMU sensor and a communication module capable of communicating with the control system computer over a serial USB connection.

The IMU sensor is of type ICM-20948 with 9-axis motion tracking from TDK [60]. The sensor has a accelerometer, magnetometer, gyroscope, and thermometer. Measurements from the 3-axis accelerometer, magnetometer, and gyroscope can be used to track sensor movement and orientation.

- **Accelerometer**
  - Acceleration in x-, y-, and z-axis
  - Output unit g
  - Configurable range $\pm$2g,$\pm$4g,$\pm$8g, or $\pm$16g
  - 16-bit ADC converter
  - Configurable low-pass filtration

- **Magnetometer**
  - 3-axis Hall-effect magnetic sensor
  - Output unit μT
  - 16-bit output resolution
  - Maximum output range $\pm 4900 \mu T$
- **Gyroscope**
  - Angular rate in x-, y-, and z-axis
  - Output unit dps (degrees per second)
  - Configurable range of ± 250, ± 500, ± 1000 or ± 2000dps

The microcontroller of type EMF32 Gecko (EFM32G210F128-QFN32) is made by Silicon Labs [36]. The microcontroller communicates with other components on the chip to source and send the data to surface. The microcontroller communicates with different component on the chip using the I2C-protocol. A complete list of all components on the PCB is shown in Table 9.1.

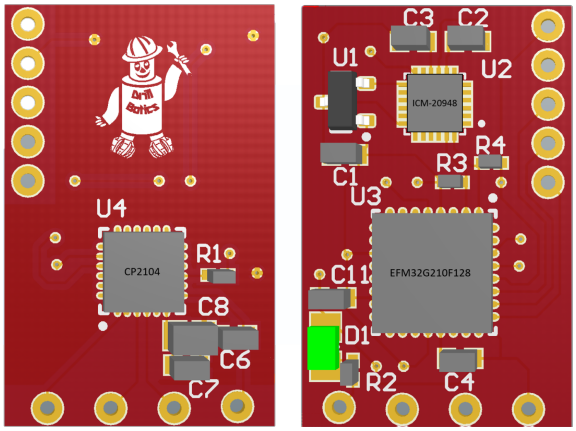

Figure 9.6: The sensor card with markings for the different components. The entire card is 21.6mm tall and 13.8mm wide. The illustration is from the original thesis describing the card [48].

Table 9.1: IMU components on the PCB

Name	Product Name	Details	Supplier
U1	EF3318AIDBZT	3.3V-1.8V DC/DC Converter	Texas Instruments
U2	ICM-20948	9-axis Motion Tracking	TDK Invensense
U3	EFM32G210F128	Microcontroller	Silicon Labs
U4	CP2104	USB-to-UART-Bridge	SIlicon Labs
R1-2	$1k\Omega$	Resistor	RS components
R3-4	$1k\Omega$	Resistor	RS components
DI	X	LED Diode	RS components
C1+C4-7+C9-12	C0603C105K9RACAUTO	$1.0\mu F$ Capacitor	RS components
C2-3	C0603C105K9RACAUTO	$0.1\mu F$ Capacitor	RS components
C8	C0603C105K9RACAUTO	$100\mu F$ Capacitor	RS components

I2C is unsuited for transferring data over longer distances. USB is a convenient serial interface found in the control system computer. The microcontroller does not support native USB output. An UART-to-USB converter is therefore used to covert UART output supported by the microcontroller to USB output supported by the control system computer. Data is transferred from the microcontroller to surface using an USB cable led along the outside of the drill pipe.

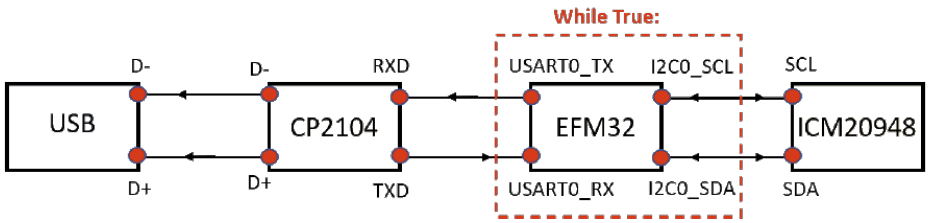

Figure 9.7: Communication structure between main components on the chip. The IMU sensor and the microcontroller communivates using the I2C interface. The microcontroller and the USB-to-UART chip communicates over an UART interface. The signal is transfered to surface using an USB interface. The illustration is from the original thesis describing the sensor [48].

The microcontroller is programmed to sample and transfer data at a fixed rate. A fixed sampling rate simplifies the control system implementation as it allows simple data synchronisation between multiple sensors.

A common issue for previous teams in the Drillbotics competition has been difficulties with

signal integrity from downhole to surface. This is mostly blamed on electromagnetic noise from the motors. Different from previous years, the USB cable will run on the outside of the drill pipe. To limit the effects of electromagnetic interference, a shielded USB cable will be used. The cable will be soldered directly to the microcontroller to limit signal degradation in connections. The sensor itself can also be shielded since magnetometer is not used for closed-loop control. The slip-ring is removed as it has been observed that it greatly affects the signal integrity and is not strictly necessary for this years implementation. The USB 2.0 interface has 4 conductors and will not be replaced as it would require a time consuming redesign of the chip.

9.6 Power Distribution

The removal of the pump motor and change of top drive motor means that all servo motors now uses 1-phase 230V. The pressure sensor for the hole cleaning water uses 24V DC power converted from 230V AC. The downhole sensor and DAQ is powered by an USB cable from the control system computer.

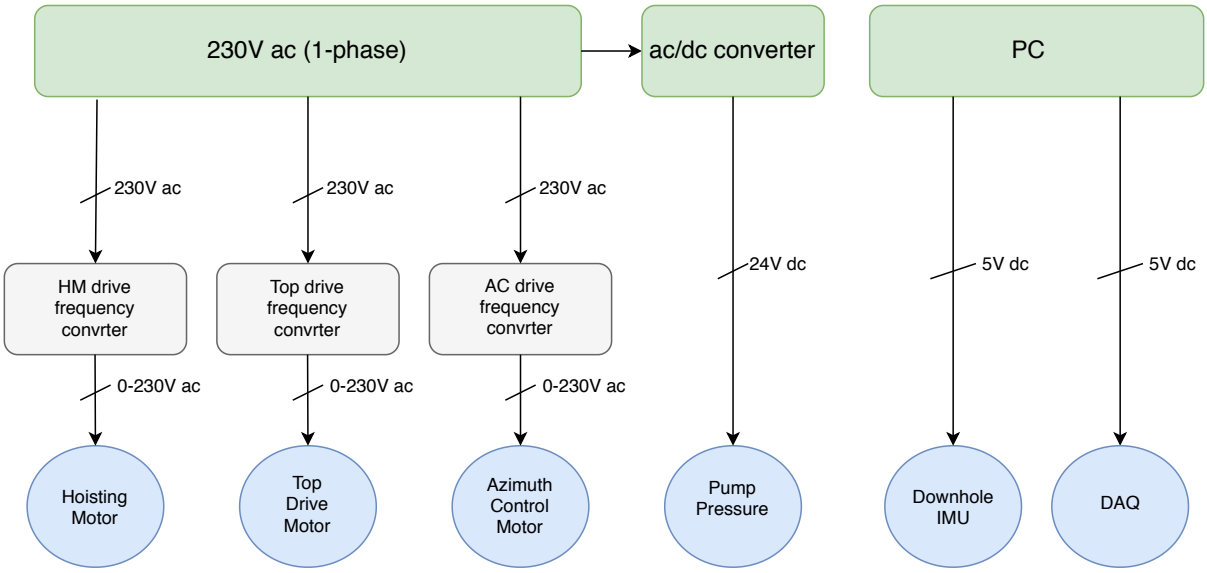

Figure 9.8: Power distribution diagram.

10 System Description and Control Design

Fully autonomous drilling relies on closed-loop control with states measured by sensors and system inputs to manipulate the states. Some states used for controlling the plant cannot be measured directly and must be estimated based on other states over time using observers. This section will give an overview of the planned implementation of the control system.

10.1 System Description

This section describes the states and inputs of the system and a model for expected bit movement in the inertial frame based on the mechanical properties of the rig.

10.1.1 System Inputs

There are 3 inputs to manipulate the states of the system. Each input is a servo motor.

- **Hoisitng motor.** As described in 6.2.1, the hoisting servo motor provides vertical motion using a ball screw. The motor is used in closed-loop control to manipulate WOB while drilling and moving the hoisting system in the inertial z-axis.
- **Top drive motor.** Rotates the rod on the inside of the drill pipe to transmit rotational energy to the drill bit. The motor controls RPM of the bit while drilling.
- **Azimuth control motor.** Changes the orientation of the drill pipe. The fixed BHA with a bent sub is rotated along with the drill pipe. Changing the orientation will therefore change the drilling direction. The motor will also be used to hold an orientation while drilling in a specific direction. The motor is connected to a hollow shaft gearbox.

The motors are controlled by providing an RPM input. RPM describes angular velocity and can be used in the system model when converted to radians per second.

Table 10.1: Inputs to the system.

Input	Variable	Unit
Hoisting	ω_{hm}	RPM
Top drive	ω_{td}	RPM
Azimuth control	ω_{ac}	RPM

10.1.2 System Measurements

The plant is controlled in closed-loop using measurements of system states. Directly measured states are denoted in table 10.2.

Table 10.2: System measurements.

Description	Variable	Unit
Hoisting motor RPM	ω_{hm}	RPM
Hoisting motor position	S_{hm}	Steps
Hoisting motor torque	T_{hm}	Nm
Top drive motor RPM	ω_{td}	RPM
Top drive motor position	S_{td}	Steps
Top drive motor torque	T_{td}	Nm
Azimuth control motor RPM	ω_{ac}	RPM
Azimuth control motor position	S_{ac}	Steps
Azimuth control motor torque	T_{td}	Nm
WOB	P_{wob}	N
DH 3-axis IMU Accelerometer	$\vec{a} = [a_x, a_y, a_z]$	g
DH 3-axis IMU Magnetometer	$\vec{m} = [m_x, m_y, m_z]$	μT
DH 3-axis IMU Gyroscope	$\vec{g} = [\dot{\psi}, \dot{\theta}, \dot{\phi}]$	dps

10.1.3 Control Objective

The objective is to drill a deviated well path based on 3 intermediate targets in the inertial x-, y-, and z-axis. The well path must be automatically generated based on the target points given prior to drilling. The system must thereafter be able to steer such that all 3 points are intersected as closely as possible by the well path. The points may vary in azimuth and inclination.

10.2 Plant Model

A simple model for position estimation is to assume that the drilling bit will have a build angle equal to the DLS. The movement of the bit will then equal the change in MD in the direction of the current bit orientation.

The azimuth control adjust yaw of the drill pipe. The yaw orientation in the top of the drill pipe is assumed to be equal to the yaw orientation in the frame of the bit. System inputs to the plant is hoisting speed as change in MD ($\dot{d}$) and speed of the azimuth control rotation ($\dot{\psi}_I$). Subscript I is the inertial frame and b is the frame of the center of the bit. Angular velocity in the frame of the bit can be written as:

$$\dot{\phi}_b = 0 \tag{10.1}$$

$$\dot{\theta}_b = DLS \cdot \dot{d} \tag{10.2}$$

$$\dot{\psi}_b = \dot{\psi}_I \tag{10.3}$$

The angular velocities can be written in vector form as the angular velocity in the frame of the bit.

$$\omega_b = \begin{bmatrix} \dot{\phi}_b \\ \dot{\theta}_b \\ \dot{\psi}_b \end{bmatrix} \tag{10.4}$$

The well path is generated in the inertial frame. The angular velocities of the bit must therefore be translated to the inertial frame. Translation of angular velocities from one frame to another is described in Equation 5.55. This specific translation can be simplified as the system only moves in pitch and yaw relative to the bit.

$$\omega_I = \frac{1}{cos(\theta)} \begin{bmatrix} \cos(\theta) & \sin(\phi) \cdot \sin(\theta) & \cos(\phi) \cdot \sin(\theta) \\ 0 & \cos(\phi) \cdot \cos(\theta) & -\sin(\phi) \cdot \cos(\theta) \\ 0 & \sin(\phi) & \cos(\phi) \end{bmatrix} \omega_b \tag{10.5}$$

By integrating the angular velocity the orientation can be obtained. The orientation of the bit in the inertial frame can be used to find the change in position using the rotation matrix described in Equation 5.54. The rate of change in MD will drive the movement of the bit at the same rate as the change in MD. The hoisting system movement in the inertial frame is only in the z-axis. The movement direction of the bit can be manipulated by changing the azimuth control orientation, allowing controlled movement in both azimuth and inclination.

$$\dot{p_I} = R_b^I \cdot \begin{bmatrix} 0 \\ 0 \\ \dot{d} \end{bmatrix} + \dot{R}_b^I \cdot \begin{bmatrix} 0 \\ 0 \\ d \end{bmatrix} \approx R_b^I \cdot \begin{bmatrix} 0 \\ 0 \\ \dot{d} \end{bmatrix} \tag{10.6}$$

Integrating the change in position yields the position of the bit in the inertial frame. The changes in the rotation matrix are very slow and approximated to be zero.

10.3 WOB Control

There are two considered approaches for controlling WOB. ROP is less of a consideration in this years competition so that the WOB control will be chosen based on experimental test results favoring movement predictability over maximum ROP.

- **Alternative 1.** Controlling WOB based on a setpoint and trying to maintain the reference using a PID-controller. The WOB is set from an experimentally obtained lookup table favoring movement predictability.
- **Alternative 2.** Controlling MD velocity based on a reference to maintain a certain ROP. This approach is considered because it allows the system model to be closer to a linear system since $\dot{d}$ can be replaced with a constant, greatly reducing the computational complexity of path generation and path reference control. The WOB will operate within a safe range where the velocity will be reduced if safety limits are exceeded.

10.4 Downhole Measurements

The competition guidelines require downhole data to be used for closed-loop control. The IMU sensor card measures acceleration, electromagnetic field strength and angular velocity in 3 DOF. Based on previous tests [48], angular velocity and electromagnetic field strength is highly susceptible to measurement noise.

Accelerometer data is expected to be the most useful downhole measurements, where the measurements mainly consists of the gravity vector aligned with the inertial z-axis and the high frequency vibrations while drilling. Roll and pitch of the sensor in the inertial frame can be estimated based on the gravity vector.

$$\hat{\phi}_I = \arctan(\frac{a_y}{a_z}) \tag{10.7}$$

$$\hat{\theta}_I = -\arctan(\frac{a_x}{\sqrt{a_y^2 + a_z^2}}) \tag{10.8}$$

Conveniently, yaw of the bit which is usually obtained by using magnetometer data is estimated to be equal to the yaw in the azimuth control system. The high frequency noise can be low-pass filtered, as the change of orientation is very slow compared to the sampling frequency. A conservative observer can be used to further improve the estimate at every time-step.

10.4.1 Sensor Translation

Because of size and BHA complexity, the IMU sensor cannot be placed close to the bit. The sensor will acquire all measurement data in its own frame. The model is based on the movement in the frame of the bit which differs from the frame of the sensor. Because the BHA is rigid, the orientation and position of the bit can be translated using rotation matrices and positional displacement.

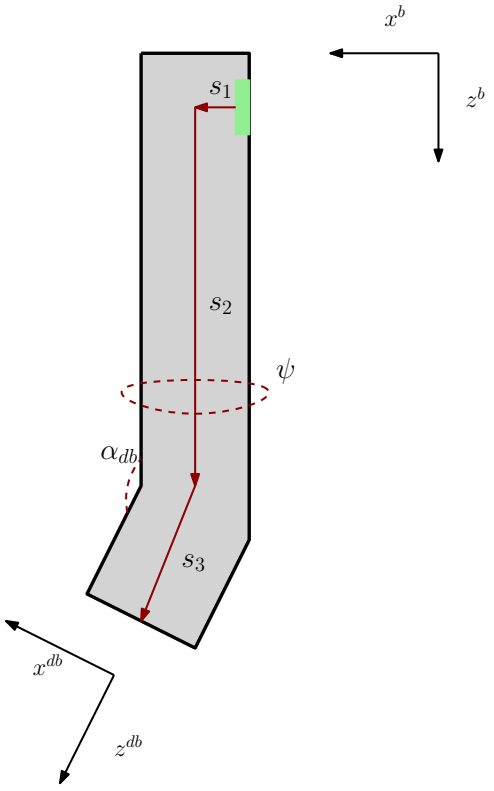

Figure 10.1: Translation from sensor to bit. The illustration is based on the 2019/2020 design report [5].

Based on the notation from the Figure 10.1, a rotation matrix from the sensor to the bit can be written as:

$$
\begin{aligned}
T_{db}^{b} &= T_{1}^{b} T_{2}^{1} T_{3}^{2} T_{4}^{3} T_{db}^{4} \\
&= \begin{bmatrix} 1 & 0 & 0 & s_1 \\ 0 & 1 & 0 & 0 \\ 0 & 0 & 1 & 0 \\ 0 & 0 & 0 & 1 \end{bmatrix} \begin{bmatrix} 1 & 0 & 0 & 0 \\ 0 & 1 & 0 & 0 \\ 0 & 0 & 1 & s_2 \\ 0 & 0 & 0 & 1 \end{bmatrix} \begin{bmatrix} cos\psi & -sin\psi & 0 & 0 \\ sin\psi & cos\psi & 0 & 0 \\ 0 & 0 & 1 & 0 \\ 0 & 0 & 0 & 1 \end{bmatrix} \\
&\quad \begin{bmatrix} cos\alpha_{db} & 0 & sin\alpha_{db} & 0 \\ 0 & 1 & 0 & 0 \\ -sin\alpha_{db} & 0 & cos\alpha_{db} & 0 \\ 0 & 0 & 0 & 1 \end{bmatrix} \begin{bmatrix} 1 & 0 & 0 & 0 \\ 0 & 1 & 0 & 0 \\ 0 & 0 & 1 & s_3 \\ 0 & 0 & 0 & 1 \end{bmatrix} \\
&= \begin{bmatrix} cos\alpha_{db}cos\psi & -sin\psi & sin\alpha_{db}cos\psi & s_1 + s_3 sin\alpha_{db}cos\psi \\ cos\alpha_{db}sin\psi & cos\psi & sin\alpha_{db}sin\psi & s_3 sin\alpha_{db}sin\psi \\ -sin\alpha_{db} & 0 & cos\alpha_{db} & s_2 + s_3 cos\alpha_{db} \\ 0 & 0 & 0 & 1 \end{bmatrix}
\end{aligned}
\tag{10.9}
$$

α_{db} is the fixed bend angle of the BHA relative to the center vertical line of the BHA. ψ is the orientation angle of the BHA relative to the initial orientation aligned with the inertial x-axis. The orientation of the drill bit can then be written as a rotation matrix.

$$
R_{db}^{b} = \begin{bmatrix} cos\alpha_{db}cos\psi & -sin\psi & sin\alpha_{db}cos\psi \\ cos\alpha_{db}sin\psi & cos\psi & sin\alpha_{db}sin\psi \\ -sin\alpha_{db} & 0 & cos\alpha_{db} \end{bmatrix} \tag{10.10}
$$

The displacement in position can also be extracted from the translation.

$$\Delta p = \begin{bmatrix} s_1 + s_3 sin\alpha_{db} cos\psi \\ s_3 sin\alpha_{db} sin\psi \\ s_2 + s_3 cos\alpha_{db} \end{bmatrix} \tag{10.11}$$

10.5 Position Estimation

Position estimation is described more extensively in section 11.4 where the estimation relies on a system model for movement based on the current orientation of the BHA measured by the IMU. The bit is assumed to move in the direction of the azimuth control orientation at the rate of change in MD position where DLS determines the angle build rate. Kalman filters are used for sensor fusion and state observation.

10.6 Reference Path Generation

There are two main ideas for generating the reference well path.

Alternative 1. Cubic Splines

Similar to the planned implementation in 2019/2020 [5], cubic splines using the MATLAB interpolation function will generate a smooth well path based on a set of points. The solution is easy to implement with a very low computational complexity. The path may not be optimal as it does not consider system behavior and rig characteristics. It is also challenging to enforce constraints for maximum inclination.

Alternative 2. Cost Function

Formulating the path generation as a quadratic optimization problem, similar to the optimal control algorithm in Equation 5.37. This approach allows the path to be generated based on the system model. Constraints can then be enforced such as maximum rate of change in yaw and maximum build angle. The cost function can be set to penalize deviations from the targets, deviations from the build rate of the model, and changes in the azimuth control. The system model is non-linear, meaning the problem may have multiple local optimums. This must be considered when solving the optimization problem. The time-steps between each potential inputs when generating the path is a trade-off between computational complexity and accuracy. This alternative is more complex but may yield significant control improvements.
The path will act as a guideline for the well path reference control so that the prediction horizon of the controller can be minimized. The prediction horizon may then only consider convergence

towards the reference path rather than having to include all remaining target points in the prediction horizon.

10.7 Well Path Reference Control

There are two main ideas for following the generated reference well path. Both approaches can have a time-step of multiple seconds as the movements of the azimuth controller and change in bit position are very slow. With a reference well path, the requirements for the prediction horizons of the controllers are greatly reduced. Deviations from the target points can be weighted higher than deviations from the reference well path to improve target homing capabilities.

Alternative 1. nMPC

nMPC is the non-linear version of the algorithm described in section 5.6.4. The algorithm finds the optimal set of inputs for a prediction horizon with the initial conditions being the current state. The system can then find the optimal set of inputs to reduce the deviations from the reference and targets. The non-linear optimization may have multiple local optimums and be non-convex, increasing the computational cost and solver complexity to consistently find a sufficiently good optimum.

Alternative 2. MPC

Similar to Alternative 1 with a simplified linearized model with a smaller computational cost. Smaller computational cost allows the time-steps to be smaller and the prediction horizon to be longer. The drawback is reduced model accuracy resulting in less accurate predictions. The movement model is non-linear and a linearized model might be too inaccurate to sufficiently estimate system behavior. A linearized system model may be formulated as a quadratic optimization problem which may also be convex. Convex quadratic problems can be solved multiple orders of magnitude faster than a non-linear problem as they have a single global optimum and has very efficient solvers.

Variable time-steps as described in section 5.6.4 can be used with both alternatives to considerably reduce the computational cost. Both alternatives can enforce state constraints.

10.8 State Machine

During autonomous operation, the system will operate in different modes called system states depending on the current task. The implementation of the system will have a set of 6 states.

State 1: Tag Rock

The inertial frame z-axis is defined to be 0 at the rock surface. To define the frame the bit is lowered until it tags the rock. The rock surface is detected by monitoring WOB where multiple consecutive measurements above a certain threshold is concidered a tag. The coordinate frame is then zeroized and the bit hoisted slightly up from the rock to allow the bit to start the rotation without having a torque spike.

State 2: Vertical Drilling

The competition guidelines [52] states that the KOP must be below 4 in. of vertical drilling. Because the BHA has a fixed bend, it will deviate from a vertical well path if the azimuth control is set in a fixed orientation. To drill vertically, the plan is to rotate the azimuth control slowly while drilling. This will create a vertical well path larger than the bit diameter until a pilothole of 4 in. is reached. Because the cable for the downhole sensor is not passed through a slip ring, the rotation direction has to be changed regularly to avoid cable wind-up. The WOB will be set conservatively to allow the azimuth controller to rotate. The hoisting movement and rotation of the azimuth controller are coordinated to avoid angle build. While rotating, there will be a maximum torque limit for the azimuth controller to avoid mechanical damage. Incident detections such as stuck pipe may be implemented if this proves to be a regular issue while testing. The system transitions to the next state when the system reaches a 4 in. MD.

State 3: Directional Drilling

After reaching 4 in. MD, the system reaches the KOP where the directional drilling state is initialized. Optimal control approaches described in section 10.7 uses a pre-planned well path as a reference. In this state, movement predictability is prioritized over maximal ROP. The parameters for WOB, azimuth control velocity, and hoisting velocity with the most predictable behavior must be experimentally obtained.

A PID-controller is used to maintain a WOB setpoint by moving the hoisting system. The azimuth control motor rotates the bit against the well path wall. To avoid excessive mechanical stress, the motor is regulated with a upper limited PID-controller where torque is measured through the gearbox. The state has continuous incident detection systems for events like stuck pipe and may jump directly to the abort state if critical state safety limits are exceeded.

State 4: Rock Exit

Once the bit is approaching the rock exit, based on the currently best position estimate, the autonomous system should be able to detect and stop the drilling operation automatically. This state would typically be initialized when the position of the bit is expected to be a few inches

from exiting the rock. If the bit exits trough the side or into an open space below the rock, the operation can be terminated by looking for a certain number of consecutive measurement below a threshold WOB value. If the bit exits into another material like wood or metal, this should be detectable by vibration data from the accelerometer or a sudden change in ROP.

State 5: Terminated

The drilling operation is ended either by rock exit or manual termination through the HMI. All motor movements are stopped and the system waits for manual input from the operator.

State 6: Aborted

Similar to the terminated state with the difference being that safety mode is activated. All manual control is overridden until the operator has disabled safety mode. This would occur if the operator presses the software emergency stop button or a critical incident has occurred like exceeding critical state safety limits.

Figure 10.2 shows all possible movements between the states.

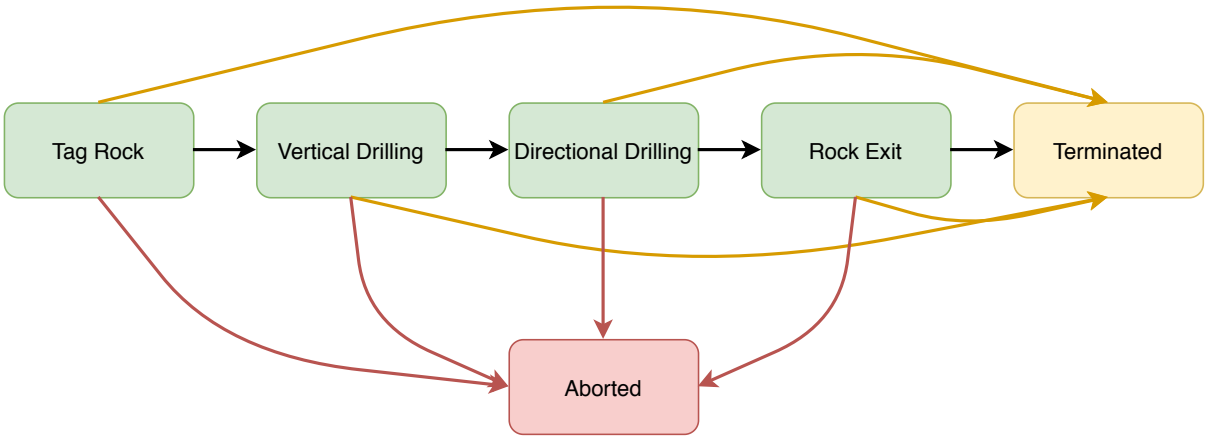

Figure 10.2: System state flow diagram.

10.9 Automation Protocols

To enable simpler integration of components, many PLCs and controllers for servo motors supports one or multiple industry protocols for communication and control. The main advantage of using such a protocol is to avoid using specific drivers or APIs for each component, which generally tend to have limited programming language support and documentation. A few common standards are EtherCAT, Ethernet/IP, Modbus, CANopen, PROFINET, and OPC.

Having multiple well established protocols makes it difficult to source components from different vendors all supporting the same standard. Ideally, all components uses the same standard

with some benefits being simple integration, improved stability, and accurate data synchronization.

10.9.1 Current Situation

The rig handed over from the 2019/2020 team had a total of five different communication protocols. The supported automation protocol of a new component have previously been and afterthought and integrating new hardware components has been a major time-sink. A goal this year was to unify the system to as few automation protocols as possible. The downhole sensor and DAQ both uses an USB interface were the downhole sensor communicates over a serial connection and the DAQ a specialized driver. These components will be used as in previous years because they are an integral part of the system and finding alternatives supporting a widespread industry standard is difficult and costly.

The hoisting system supports the Ethernet/IP protocol. The system uses a translation box described in section 10.9.8 between between the Ethernet/IP and Modbus TCP protocols. Modbus TCP is used because it has been the simplest protocol to implement in LabVIEW. The translation box maps the register values from the Ethernet/IP standard to the Modbus TCP standard such that the Ethernet/IP subnet is accessible from the control system computer. The top drive motor uses a different standard called CANopen. CANopen has proven to be more difficult to implement and control from LabVIEW than Modbus TCP and has currently the smallest sampling frequency in the system.

10.9.2 OSI Model

Most of the widespread standards communicate over an IP network implementation. This is mainly for convenience because every sensor can then be connected to a shared network, instead of directly to the receiver, using standardized widely available components. The backbone of these standards are the layered OSI model for network communication [68]. The purpose of the model is to abstract the functionality so that standards can be built on top of each other. Standards can then be used interchangeably without affecting the lower layers. Routers and switches relies on the first three layers, and implementations built from layer 4 and up can generally use standardized widely available networking components. Each layer serves a specific purpose.

Table 10.3: OSI model description. The table is based on the table found on Wikipedia [68].

	Layer	Function
7	Application	High-level APIs, resource sharing, remote file access
6	Presentation	Translation between service and application, encoding. Compression, encryption etc.
5	Session	Managing communication sessions
4	Transport	Transmission of segments on a network. Segmentation, acknowledgements etc.
3	Network	Structuring and managing multi-node network. Addressing, routing, traffic control
2	Data link	Reliable transmission between two physically connected nodes
1	Physical	Transmission and reception of raw bit streams over a physical medium

10.9.3 TCP and UDP

The TCP protocol is found in the transport layer of the OSI model [68]. Transmission Control Protocol (TCP) is a reliable standard for sharing data between applications. The protocol is responsible for establishing and terminating connections, data transfer, error detection, and flow control management among other features [69]. TCP is a reliable protocol because there has to be an open connection before data can be sent and the receiver confirms that data has been received by sending an acknowledgment. If the acknowledgment is not received by the sender within a timeout window, the sender will try to resend the data.

Acknowledging that data has been received is not always a requirement. Some data has little to no value if received after the intended time window. An example of this is when reading real-time sensor data with a high sampling frequency. For streams of data, User Datagram Protocol (UDP) is a more suitable choice. UDP does not use acknowledgments, reducing the overhead. Furthermore, there is no need for an established connection to pass data. Most standards use a combination of TCP and UDP, where TCP is used if reliability is a requirement.

10.9.4 Ethernet/IP

A widely available standard relying on the TCP and UDP standards is Ethernet/IP managed by ODVA [66]. Ethernet/IP uses the OSI model as it collapses the application (7), presentation (6), and session layer (5) into a Common Industrial Protocol (CIP) object [51]. This enables sensors and PLCs to be controllable using a standardized template file compatible with existing software. The standard is optimized for real-time control applications.

The main advantage of the Ethernet/IP standard is that it is widely adopted in sensors and

PLCs, making it feasible to source all components for a system with a single unified automation protocol.

10.9.5 Modbus TCP

An older but still widely available standard is Modbus [67]. Modbus was developed in the late 1970s and has for many years been the industry standard. Today, the age of the standard has started to show its shortcomings and fewer manufacturers offers Modbus support. Because of its wide adoption and easy implementation, Modbus is still one of the standards with the best software support and one of the few automation protocols with native support in both LabVIEW and MATLAB.

The version of Modbus designed to communicate over IP networks is called Modbus TCP. Instead of a configuration file, each manufacturer provides a list of registers that can be read and written to. Data are organized in coils and holding registers that can be read and edited to control the device or read sensor data.

10.9.6 Alternative Protocols

There are multiple protocols that could have been used to control the rig. Some common standards are:

- **EtherCAT.** Modern, widely available, IP based standard with a low hardware implementation cost for each component [65]. Ideal for hard real-time systems as synchronization is built directly into the standard. Similarly to Ethernet/IP it uses a configuration file provided by the manufacturer of the component.

  EtherCAT would have been a great choice if there were no existing components on the rig. However, replacing integrated and proven components in the system only to move to another standard was considered poor use of resources.

- **CANopen.** Common IP based protocol that uses object dictionaries to pass data between the nodes of the network [64].

  The handover top drive uses this protocol. The team from 2019 reported difficulties implementing this standard in the control system [48]. Other standards are therefore preferred.

- **PROFINET.** Another common IP based industrial standard. PROFINET is mainly targeted towards large scale industrial applications focusing on scalability of the network and easy integration [57].

Similary to EtherCAT, PROFINET would be a viable option if completely rebuilding the rig. Using PROFINET would require a unnecessary replacement of the hoisting motor with no major benefits compared to Ethernet/IP.

10.9.7 New Components

When acquiring new components automation protocol was carefully considered. Modbus TCP is preferred because of easy integration and proven software support. Ethernet/IP is already in use in the system. The protocol has worked reliably, making Ethernet/IP the second choice. The new top drive did not have a Modbus TCP option but will be integrated in the already existing EtherNet/IP subnetwork. The subnetwork relies on a translation box between the Modbus TCP network supported by the software and the Ethernet/IP network supported by the two motor controllers.

The azimuth control motor was chosen with integration as one of the most important considerations. The servo controller has native supports both Modbus TCP and Ethernet/IP. There are two options when integrating the motor:

- **Alternative 1.** Integrate the azimuth control servo motor using its native Modbus TCP support. Direct communication from the software but more difficult to synchronize with the data from the top drive and hoisting system.
- **Alternative 2.** Connect the servo motor to the Ethernet/IP network for better data synchronization but relying on translation between the two protocols similar to the top drive and hoisting motor.

10.9.8 Hilscher NT-100

The translation between the EtherNet/IP standard and Modbus TCP is handled by a real-time gateway of the type Hilscher NT-100-RE-EN [29]. The gateway maps the registers of the Ethernet/IP network and Modbus TCP subnetworks such that they can be read and written to across the subnetworks. Registers are mapped in the configuration software of the unit.

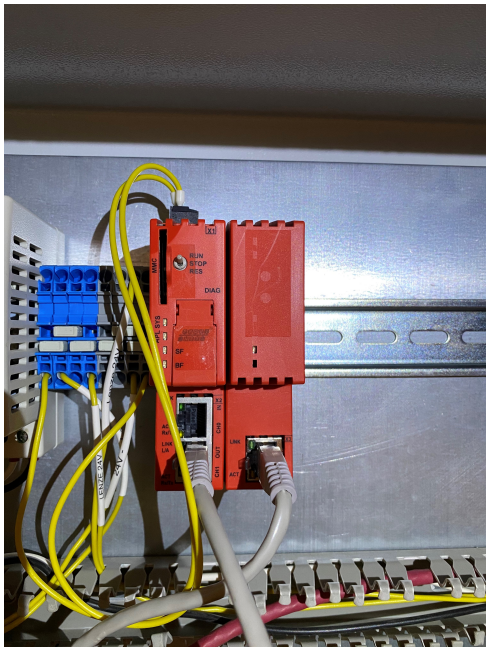

Figure 10.3: Gateway box from Hilscher.

10.9.9 System Protocol Structure

Using Alternative 1 in section 10.9.7, Figure 10.4 shows the overall automation protocol structure with the new components.

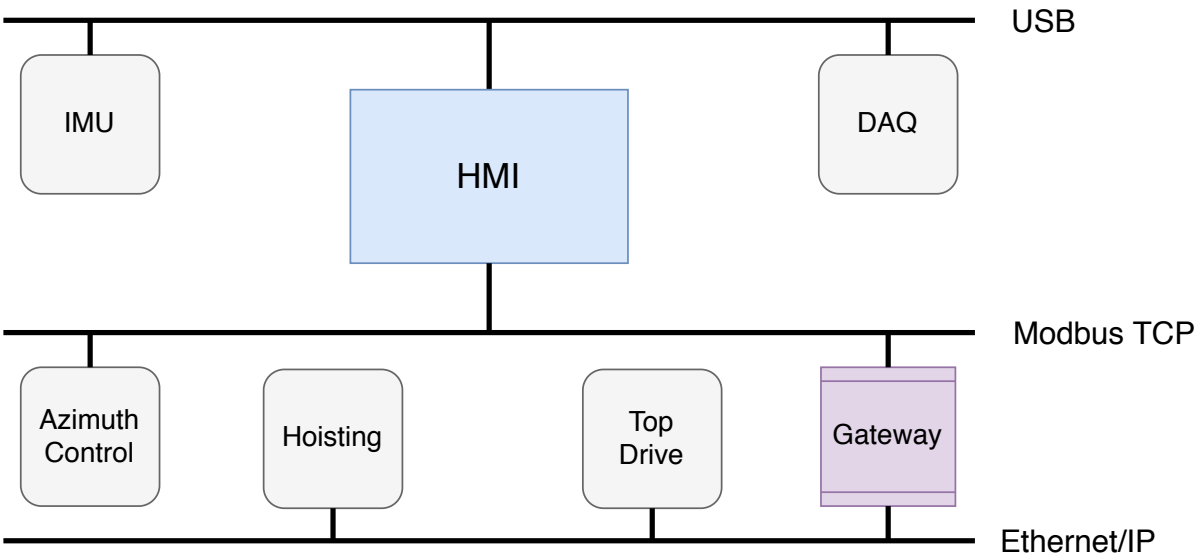

Figure 10.4: System protocol structure.

10.10 Software Integration

At the time of writing, the software environment for low-level hardware control is not decided. Previous teams has used LabVIEW to control hardware components. This year the control

system has to be more complex to enable steering and precise position estimation. The team will therefore make an effort to use Simulink instead of LabVIEW. The digital twin described in section 11 has to be implemented in Simulink as LabVIEW has very limited simulation capabilities. Another motivating factor is ease of development as cybernetics and petroleum students are used to MATLAB through other courses at NTNU. Using MATLAB and Simulink to control the rig is therefore ideal.

LabVIEW has some limitations compared to Simulink and MATLAB in regards to toolboxes and ease of development, while LabVIEW has better support for hardware components. Most notably, Simulink only supports hardware control in Modbus TCP slave mode. Because the rig has been used for other experiments related to research this fall, hardware support with Simulink is not yet tested. The translation box from Hilscher described in section 10.9.8 should support conversion from Ethernet/IP to Modbus TCP master but this is still not tested. The DAQ has been verified to work with Simulink. The team considers two alternatives:

- **Alternative 1.** Simulink controls the hardware components directly and reads sensor data using Modbus TCP communication. This is the preferred option to reduce complexity of the software control system. Realtime low-level control like PID controllers and all drilling incident detection are implemented directly in Simulink. This implementation is less complex but may be infeasible due to limited hardware support.
- **Alternative 2.** Low-level control and sensor data reading in LabVIEW while the high-level autonomous drilling control is implemented in Simulink. Data and control commands are passed using a Drilling API as described in section 10.11. This implementation allows more reuse of existing code and has better hardware support, but is more complex to implement and maintain.

Passing data and commands using a Drilling API is expected to introduce considerable latency. Low-level real-time control is sensitive to time delays, while high-level control is less sensitive to latency and can therefore be streamed. Using only LabVIEW would be tedious as all control implementations that has been tested in the digital twin would then need to be rewritten for the LabVIEW implementation.

10.10.1 Simulink

Simulink block diagram programming environment that is a part of the MathWorks ecosystem [41]. It supports system-level design and simulation with native support for MATLAB code. MATLAB algorithms can then be used directly in the control system design. Simulink has advanced modelling capabilities for continuous systems and has powerful toolboxes for optimization and control systems.

10.10.2 LabVIEW

LabVIEW is a systems engineering software for measurement and control applications [31] made by National Instruments. LabVIEW is optimized for easy hardware implementation using block diagrams. LabVIEW has extensive hardware support, especially with DAQs and sensors. National Instruments also make their own measurement components.

10.10.3 HMI

For non-autonomous operation, the system can be controlled using a GUI as the HMI. Depending on the chosen software environment, the HMI will be implemented in the same software environment as the low-level control. The GUI will allow the user to operate the rig using high-level commands with intuitive inputs. Both Simulink and LabVIEW have tools for creating advanced GUIs.

10.11 Drilling API

Drilling API support is a requirement for this years competition. After some research and consulting industry advisors, there seem to be no widely adopted openly available API for controlling drilling rigs. Some standards that were found but did not align with our requirements are:

- **NOVOS.** An industrial system to automate repetitive drilling activities marketed as an ”Reflexive Drilling System” [49]. The system can perform a series of actions instead of the driller having to execute the sequence manually.
- **DEAL.** Automated drilling assist system to aid the driller developed by mhwirth [44]. Software package to enable flexible and scalable implementation of automation functionality.
- **DrillTronics.** Software for drilling process control automation developed by Sekal to maximize productive time during drilling [56]. The software offers automatic safety mechanisms to react to drilling incidents.

10.11.1 OPC

Although there is no standardized API for drilling automation, different versions of OPC are widely adopted for proprietary control in the oil and gas industry. OPC is developed and maintained by the OPC Foundation to allow seamless interoperability between component manufacturers. OPC abstracts PLC specific protocols into device-specific requests. The latest standard is called OPC UA and is slowly gaining widespread adoption. OPC UA is therefore a sensible standard to develop a drilling API based on.

10.11.2 Planned Implementation

Because of limited technical resources in the team, the planned API implementation will be a set of simple high-level commands to control typical rig parameters. The intended end-user of this API will be scientists and industry partners wanting to do experiments on the rig without having to edit the control system itself. The API will use the OPC UA standard. The API will be designed as a prototype and foundation for future work.

11 Digital Twin

With such a complex control system implementation it is useful to run digital simulations of the rig to verify control system behavior. A digital twin is a virtual simulation of a physical system. The digital twin enables fast prototyping of the position estimation, well path generation, and reference path controllers. The digital twin can be designed to use the same control system implementation as the physical rig. Another advantage of the digital twin is that all states of the system is known and can be compared to state estimates.

Simulink is a part of MATLAB ecosystem designed for block diagram programming of simulations and digital twins. Physical systems can be described using ODEs and implemented in Simulink using predefined blocks and native MATLAB functions. Simulink is designed to simulate continuous time systems without the need for discretization.

The digital twin is based on the plant model described in section 10.2. The plant model and the physical rig are continuous time systems. The digital twin is therefore described with continuous time ODEs. The control system relies on sampled sensor measurements, so that the control system requires a discretized model. The current implementation only simulates bit movements and not ROP and WOB.

The inputs to the plant is the angular velocity from the azimuth controller and the movement velocity in MD denoted $\dot{\psi}_I$ and $\dot{d}$. Similar to the plant model, position and movements are described in the inertial frame.

11.1 Plant Simulation

To mimic physical plant behavior, the system is described using continuous time ODEs in a plant model. Drilling operations are stochastic processes and random noise is added to the processes to more closely represent physical rig behaviour while drilling. Ideally, the plant should respond equally to control inputs as the physical rig. In practice the plant simulation is based on an educated guess of physical rig behavior and control implementations must eventually be tested experimentally.

The plant simulation uses the inputs to the system to simulate bit movement based on the system plant model described in section 10.2. Angular velocity in the frame of the bit is described by the Equation 10.1, 10.2, and 10.3. The equations can be implemented using block diagrams and MATLAB functions in Simulink. The angular velocity in the inertial frame can be found using Equation 11.7. This equations is implemented as a MATLAB function taking the angular velocity in the frame of the bit and the current inertial orientation. The angular velocity in the

inertial frame is integrated to obtain the current orientation.

The change in position is driven by the change in MD that moves in the positive z-axis in the inertial frame. The movement of the bit is dependent on its current orientation in the inertial frame. The movement in MD is therefore multiplied with the rotation matrix described in Equation 5.54. This outputs the rate of change in position in the inertial frame that can be integrated to find bit position.
The block diagram for the plant simulation without added noise is shown in Figure 11.1.

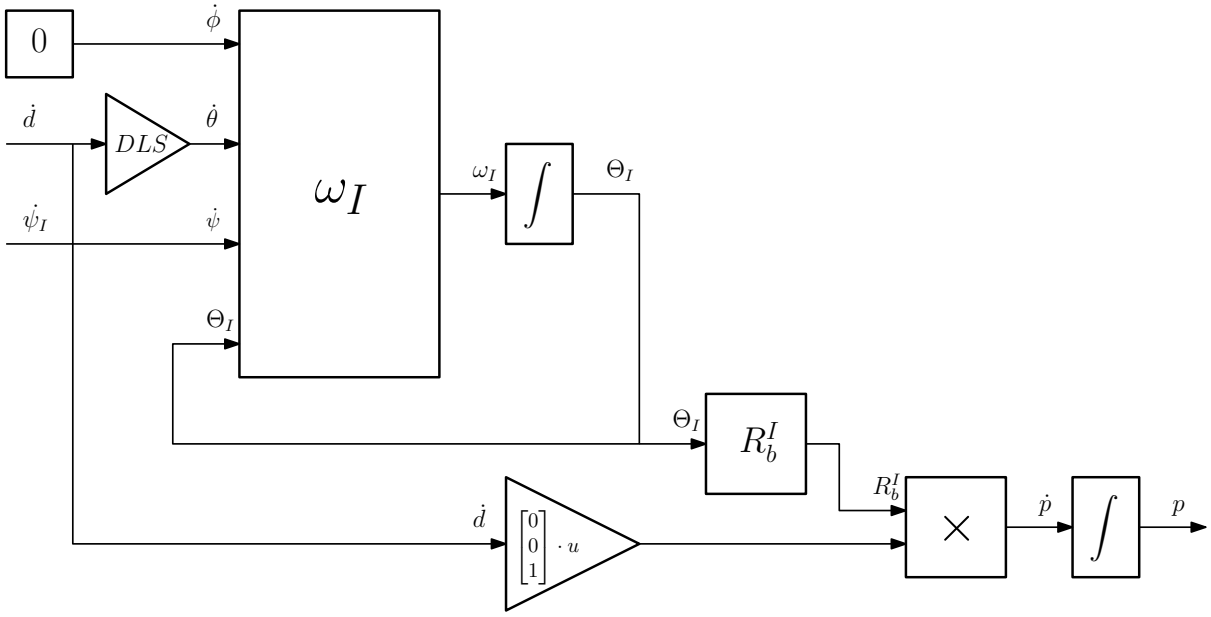

Figure 11.1: Diagram of plant model. The system takes in the inputs $\dot{d}$ and $\dot{\psi}_I$ and outputs the position of the bit in the inertial frame. Bit velocity, orientation, and angular velocity in the inertial frame can also be extracted.

11.2 Sensor Measurements

The physical rig has an array of sensors for closed-loop control. Sensor data is sampled at discrete time intervals. All measurements have some uncertainty and each measurement must be considered stochastic. Variance of the measurements varies greatly depending on the sensor. Measurement noise and uncertainty is simulated using random white noise added to the state from the plant simulation. Not all states can be measured directly, and states like position relies on estimates based on data from multiple sensors over time.

Sensors can be simulated by reading the states of the digital twin and adding noise to the measurements. A simulated IMU can be created by reading the digital twin orientation, position, and angular velocity. These states are sampled at discrete time intervals to mimic discrete sensor readings. Due to a lot of electromagnetic noise the magnetometer is currently not used

in the digital twin, although it is possible to simulate both uniform and non-uniform magnetic fields. The gyroscope is simulated, however the minuscule angular velocity of the bit orientation and noisy measurements makes obtaining useful data difficult. Accelerometer data is therefore expected to be the most useful data from the IMU.

Acceleration is measured in the frame of the sensor. The simulated accelereometer takes the current orientation in the inertial frame from the digital twin as input. The gravity is aligned with the z-axis in the inertial frame. A diagram of a simulated accelerometer is shown in Figure 11.2.

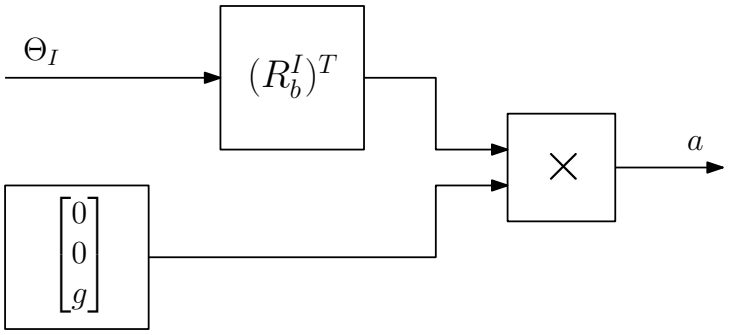

Figure 11.2: Diagram of the simulated IMU accelerometer. The diagram assumes that the sensor is located exactly at the bit, which is not the case. This can be corrected for using the rotation matrix in Equation 10.10. The rotation matrix is not included to reduce the complexity of the diagram.

The servo motors have sensors for position, torque, and angular velocity. For the purposes of the position estimation, only the hoisting speed and azimuth control angular velocity is required. For the physical rig, the angular velocity of the hoisting motor needs to be converted to rate of change in MD and the angular velocity of the azimuth control needs to consider the gearing ratio of the gearbox. For simplicity MD and angular velocity of the azimuth control is provided as direct inputs. The inputs are sampled at discrete time intervals to mimic the data provided by the servo motors.

11.3 Discrete Time Position Model

Measurements are sampled discretely and it is therefore impossible to track the states of the system exactly over time. To minimize the deviations between the plant simulation and its discrete implementation, the continuous time model must be discretized. A discretized model estimates the next state directly instead of describing the rate of change.

$$x[k+1] = f(x[k], u[k]) \tag{11.1}$$

The plant model relies on continuous time ODEs were the rate of change is obtained rather than the next state itself. The discrete model must therefore be implemented differently when using discrete values. Furthermore, some sensors will have a poor measurement of the rate of change from one sample to another. The plant has multiple servo motors where the position is accurately known while the velocity is a rough estimate. In discrete time it is possible to use the delta between two accurately known values to estimate angular velocity. If the sampling frequency is sufficiently high, Euler discretization is a close approximation of the continuous time system. Euler discretization approximates the definition of the derivative.

$$\dot{x} \approx \frac{x[k+1] - x[k]}{\Delta t} \tag{11.2}$$

Euler discretization has the drawback of having a limited stable range for fast dynamics. Since the sampling frequency of the sensors are very high compared to the movement in position, stability is not a concern. The main advantage of the Euler discretization is simple implementation. There are other more complex discretization algorithms with a larger stability range and closer approximation like Runge-Kutta based methods, however the high sampling frequency to movement ratio makes the differences minuscule for position estimation.

Euler discretization requires changes to the system model, as the state derivative is replaced by the state delta divided by the time-step. A set of discrete bit movement equations are obtained.

$$\hat{\phi}_b[k+1] = \hat{\phi}_b[k] = 0 \tag{11.3}$$

$$\hat{\theta}_b[k+1] = \Delta t \cdot DLS \cdot \dot{d}[k] + \hat{\theta}_b[k] \tag{11.4}$$

$$\hat{\psi}_b[k+1] = \Delta t \cdot \dot{\psi}_I[k] + \hat{\psi}_b[k] \tag{11.5}$$

Similar to Equation 10.4 in continuous time model, the angular velocities can be written on vector form. Angular velocity ω is the derivative of the orientation Θ.

$$\hat{\Theta}_b[k+1] = \begin{bmatrix} \hat{\phi}_b[k+1] \\ \hat{\theta}_b[k+1] \\ \hat{\psi}_b[k+1] \end{bmatrix} \tag{11.6}$$

Based on the bit movement, orientation in the inertial frame can be obtained.

$$\hat{\Theta}_I[k+1] = \frac{1}{cos(\hat{\theta})} \begin{bmatrix} \cos(\hat{\theta}) & \sin(\hat{\phi}) \cdot \sin(\hat{\theta}) & \cos(\hat{\phi}) \cdot \sin(\hat{\theta}) \\ 0 & \cos(\hat{\phi}) \cdot \cos(\hat{\theta}) & -\sin(\hat{\phi}) \cdot \cos(\hat{\theta}) \\ 0 & \sin(\hat{\phi}) & \cos(\hat{\phi}) \end{bmatrix} \hat{\Theta}_b[k+1] + \hat{\Theta}_I[k] \quad (11.7)$$

The new position after the time-step can then be estimated based on the estimated orientation in the inertial frame.

$$p_I[k+1] = \Delta t \cdot \hat{R}_b^I \cdot \begin{bmatrix} 0 \\ 0 \\ \dot{d} \end{bmatrix} + p_I[k] \quad (11.8)$$

The discrete model can make use of sampled data and be implemented in the control system.

11.4 Position Estimation

Following a reference path requires that the position of the drill bit to be known. Since the well path is deviated this can not be calculated directly from the MD. Measuring position directly with a high degree of accuracy is difficult. Using the discrete position model described in section 11.3 the movement of the bit can be estimated. The IMU data will be used to correct the current best estimate of the orientation, and the system model assumes that the bit moves in its current orientation at the rate of change in MD. IMUs tend to have difficulty measuring slow movements as the noise to movement ratio makes reading useful data difficult. Furthermore, electromagnetic noise and biases makes the magnetometer readings unreliable, gyroscopes will drift over time, and an accelerometer will measure vibrations from the drilling operation.

11.4.1 Accelerometer

Based on experiments from previous years [48], the most reliable and useful source of data from the downhole sensor is acceleration measurements. Pitch and roll can be estimated from the accelerometer data as described in section 10.4. A single sample of raw data from the accelerometer is severely affected by process noise in the form of vibrations.

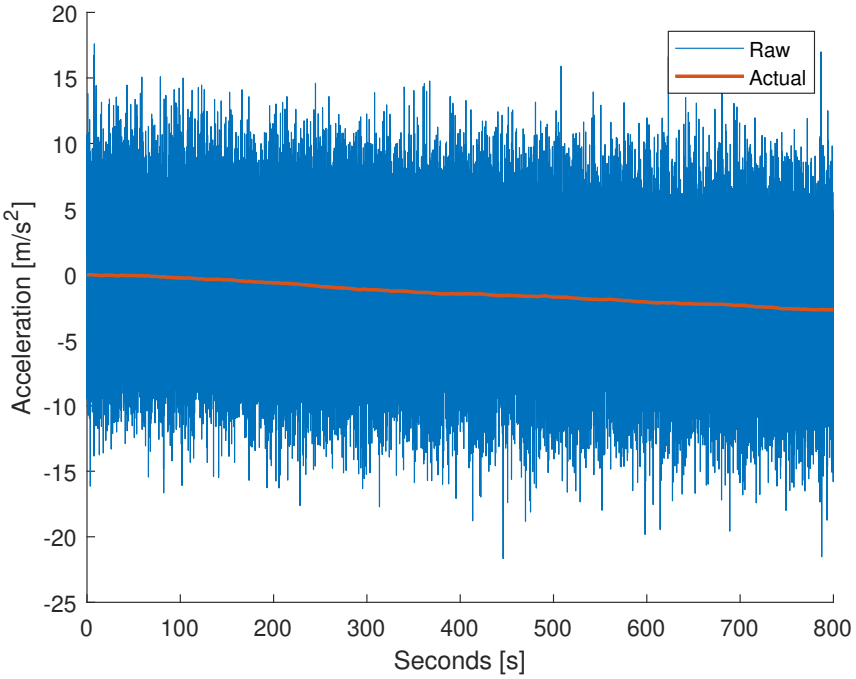

Figure 11.3: Raw and data from the digital twin for acceleration in the x-axis in the frame of the bit sampled at 100Hz. The noise is artificially added to more closely represent drilling vibrations. The mean of the raw acceleration follows the real value from the digital twin.

Process and measurement noise is high frequency. The rate of change in position is very slow compared to the noise. A simple way of obtaining a better estimate is to filter out high frequencies using a low-pass filter. The trade-off when using a low-pass filters is slower response. This will introduce a significant delay between change in state and the change in estimate. Moving the cutoff frequency of the filter to a larger frequencies introduces more noise while improving filter response.

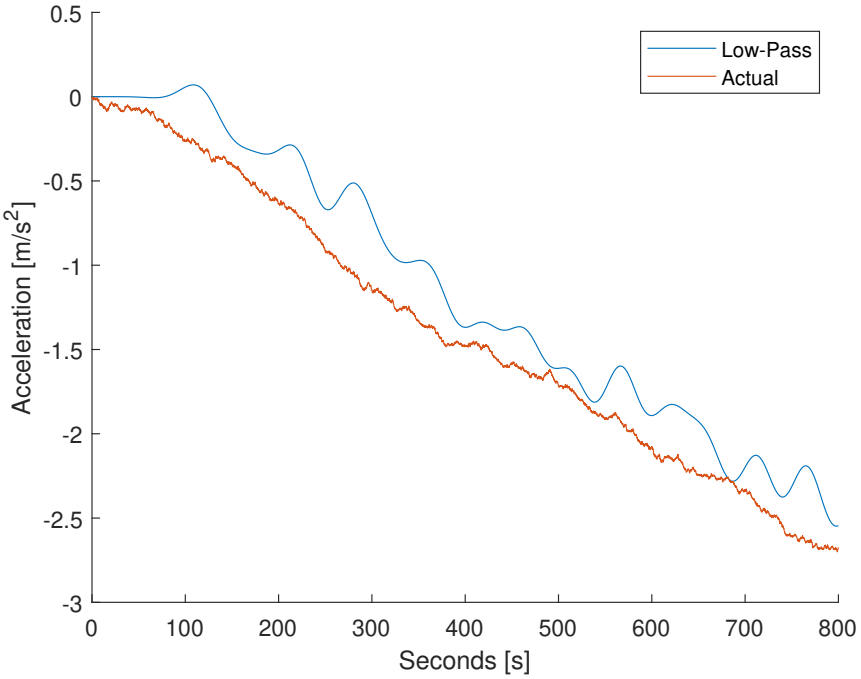

Figure 11.4: Low-pass filtered data with the same raw data as in Figure 11.3. Passband edge frequency is set to 0.02Hz and stopband edge frequency to 0.035Hz. The implemented filter is therefore a passband filter for low frequencies. Passband was chosen as the filter configurator for low-pass uses a legacy implementation in Simulink. Notice the difference in scale compared to the raw data plot. The trade-off when choosing passband and stopband frequency is response to noise. Lower frequency will have less noise but slower response.

Tuning the low-pass filter was done using a spectrum analyzer in Simulink. The spectrum analyzer was connected to the continuous time system for the simulated IMU to limit aliasing effects of the fixed rate sampling frequency of the simulated IMU. The filter must be tuned for the build rate with the largest feasible ROP such that the cutoff frequency can be set for the worst case scenario of the highest movement frequency.

11.4.2 Low-Pass Estimation

The acceleration data is used to calculate the estimated pitch and roll in the frame of the bit as described in Equation 10.7 and Equation 10.8. Combining multiple measurements, each with their own uncertainties and measurement noise further increase the variance. Even with a relatively good filtered estimate of the signal, the accumulated variance will significantly affect the reliability of the calculated roll and pitch.

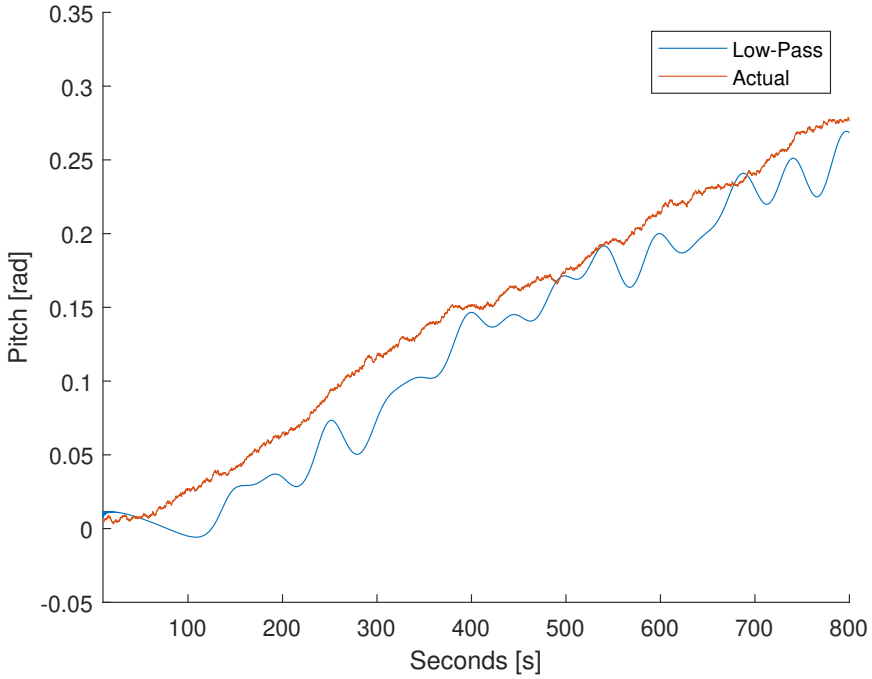

Figure 11.5: Low-pass filtered x-axis accelerometer data used for pitch calculation compared to the actual pitch value from the digital twin. Although the low-pass filtered value follows quite close to the actual pitch, using the pitch to estimate the position will cause significant deviations from the actual position of the bit.

Although the pitch in Figure 11.5 may seem to be a somewhat close approximation, pitch and roll is primarily used to estimate position as described in Equation 10.5. Using the estimated roll and pitch while maintaining the inertial yaw at 0 the position can be estimated as with the discrete time model.

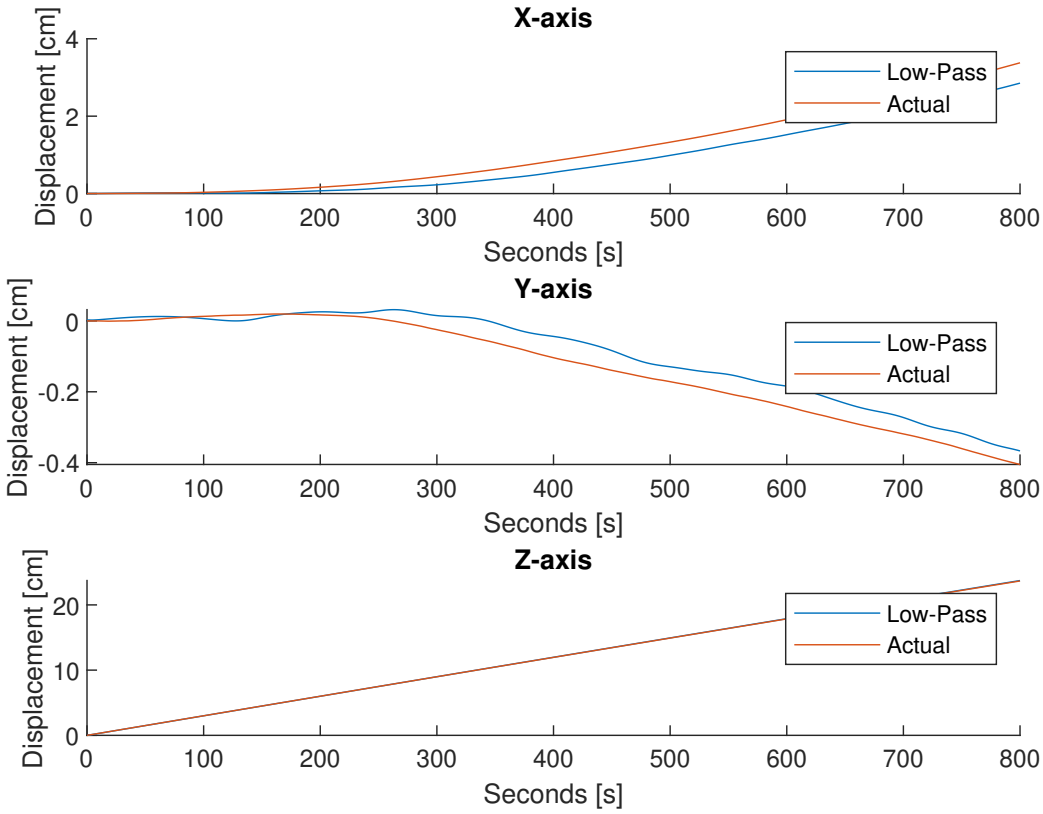

Figure 11.6: Position estimation based on low-pass filtered data with the azimuth controller locked in the x-axis orientation. Even with a duration of about one third of the expected drilling duration the position has already developed a significant deviation from the digital twin. X-axis is most affected due to slow convergence towards the actual system state with the orientation estimate.

11.4.3 Kalman Filtered Acceleration Estimate

A more accurate estimate of position can be obtained using a Kalman filters. As described in section 5.6.5 the Kalman filter finds the optimal estimate, meaning the estimate with the lowest covariance based on the available measurements and their covariances and a system model.

Orientation measurements are based on the noisy accelerometer data. The accelerometer should ideally only measure the gravity to be able to estimate pitch and roll. Based on the current best estimate of orientation in the inertial frame it is possible to model the gravity vector.

$$\hat{a} = (\hat{R}_b^I)^T \cdot \begin{bmatrix} 0 \\ 0 \\ g \end{bmatrix} \tag{11.9}$$

The gravity model acts as a conservative observer limiting the fluctuations over time compared to the high covariance accelerometer measurement. The raw accelerometer measurements are weighted based on a precalculated covarinace estimation from historical drilling data.

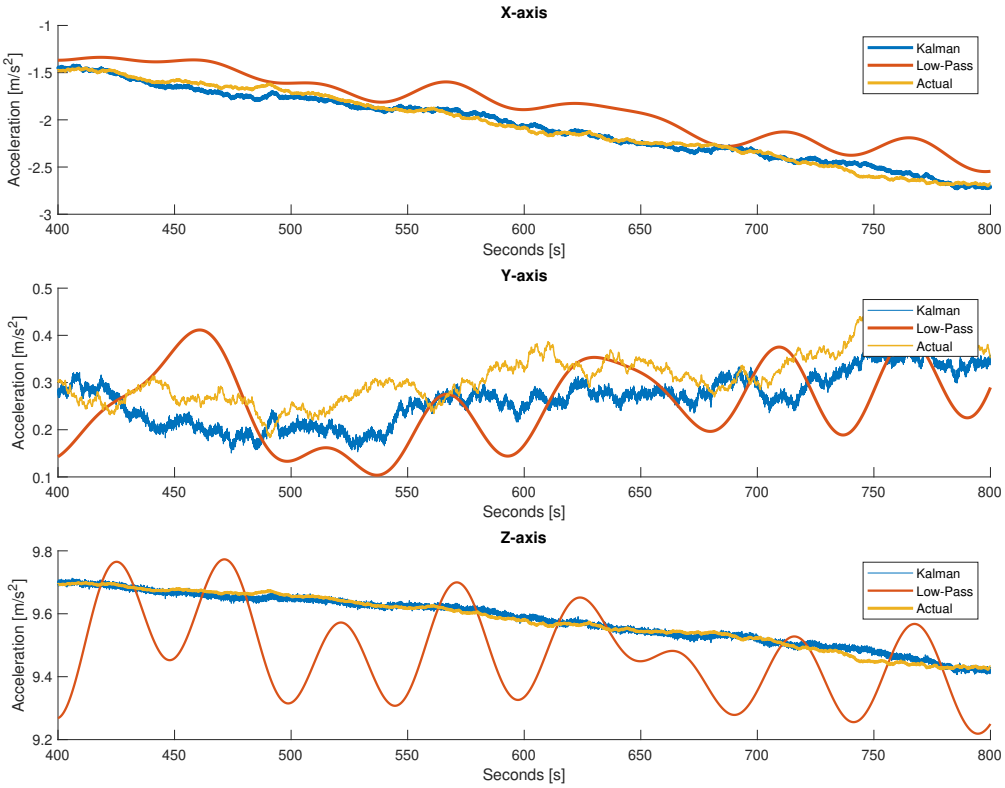

Figure 11.7: Kalman and low-pass filtered value together with the actual value from the digital twin. The Kalman filtered value follows the actual value more close than the low-pass filtered value. Time has been shifted to allow the low-pass filter to converge and give ideal comparable results. The Kalman filter has initial values and will have a much faster initial convergence.

As seen in Figure 11.7 the Kalman filter manages to follow the actual value more closely with less noise than the low-pass filtered estimate. If the model has a low covariance while the measurements has a high covariance, the Kalman filter will have a low-pass effect on acceleration measurements.

11.4.4 Kalman Filtered Orientation Estimate

Another Kalman filter is used to provide the best estimate of the current orientation. The Kalman filter for orientation uses the discrete model described in Equation 11.7. For the test to be more realistic, the build rate of the discrete model was intentionally set to have a smaller build rate of $2/3$ the plant model build rate. This simulates an imperfect model. Measurement

of roll and pitch comes from the output of the Kalman filtered acceleration values used in the acceleration to orientation Equation 10.7 and Equation 10.8. Yaw is assumed to be equal to the yaw of the azimuth control.

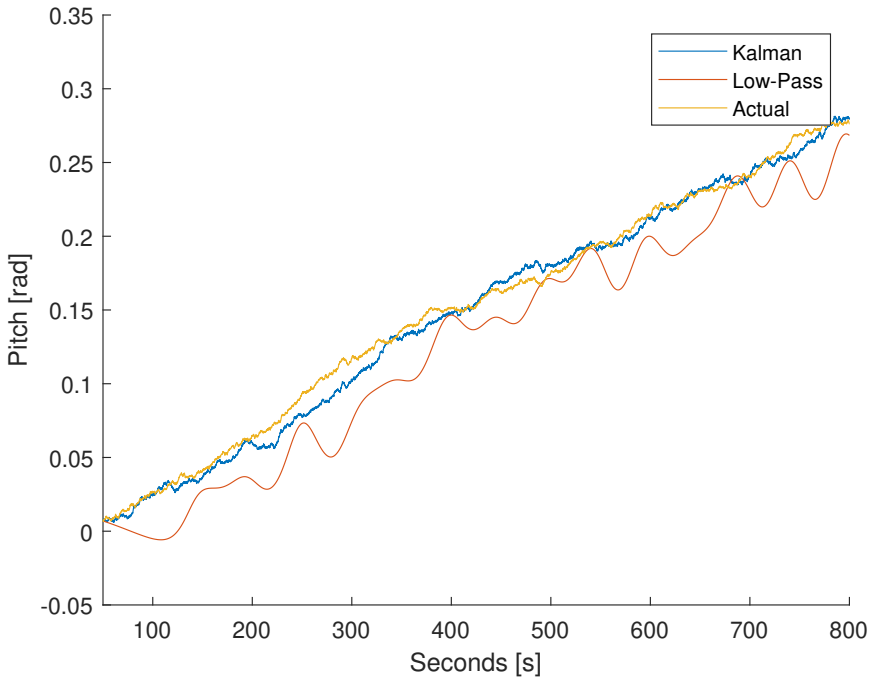

Figure 11.8: Kalman and low-pass filtered pitch with the actual value from the digital twin. The Kalman filter is generally a close approximation to the actual value. Deviations in orientation will over time result in an accumulating uncertainty in the position estimate.

The Kalman estimated orientation is used to estimate the change in position. The low-pass and Kalman filtered estimates are compared in Figure 11.9.

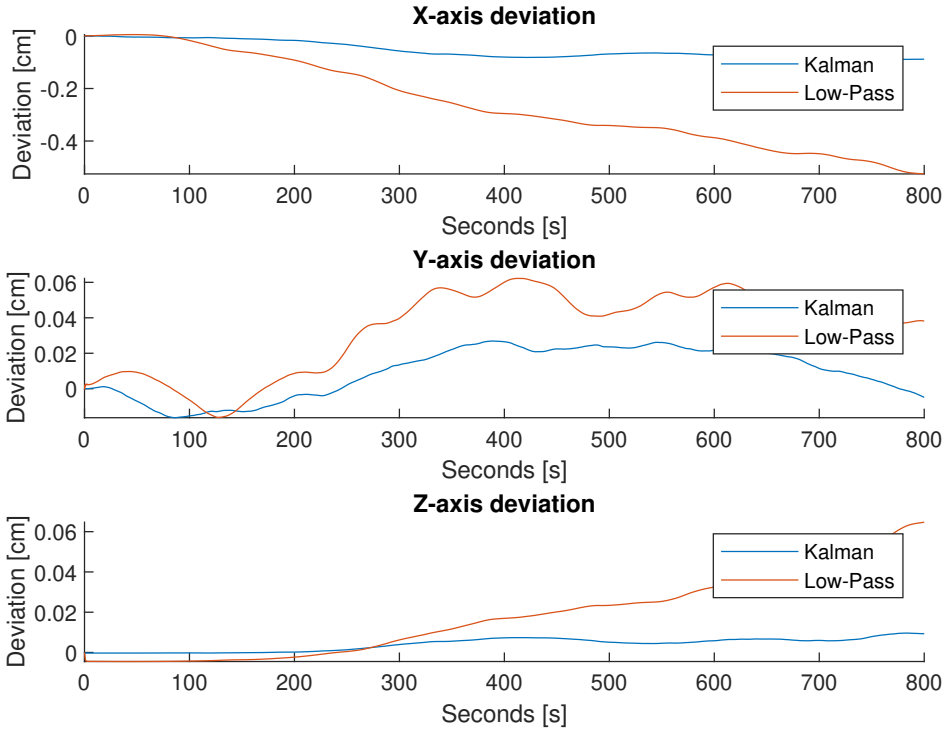

Figure 11.9: Deviations in position compared to the actual value from the digital twin. The Kalman filtered orientation value reduces the deviation in position significantly compared to the low-pass orientation estimate. Deviations will accumulate over time and must be kept as small as possible to accurately determine position throughout the drilling operation.

From Figure 11.9 it is clear that the Kalman filtered estimation has less accumulated deviation. The Kalman filter implementation will therefore be used to estimate the position used by the well path reference control. Reducing uncertainty in the position estimate is essential to intersect the target points in the rock accurately.

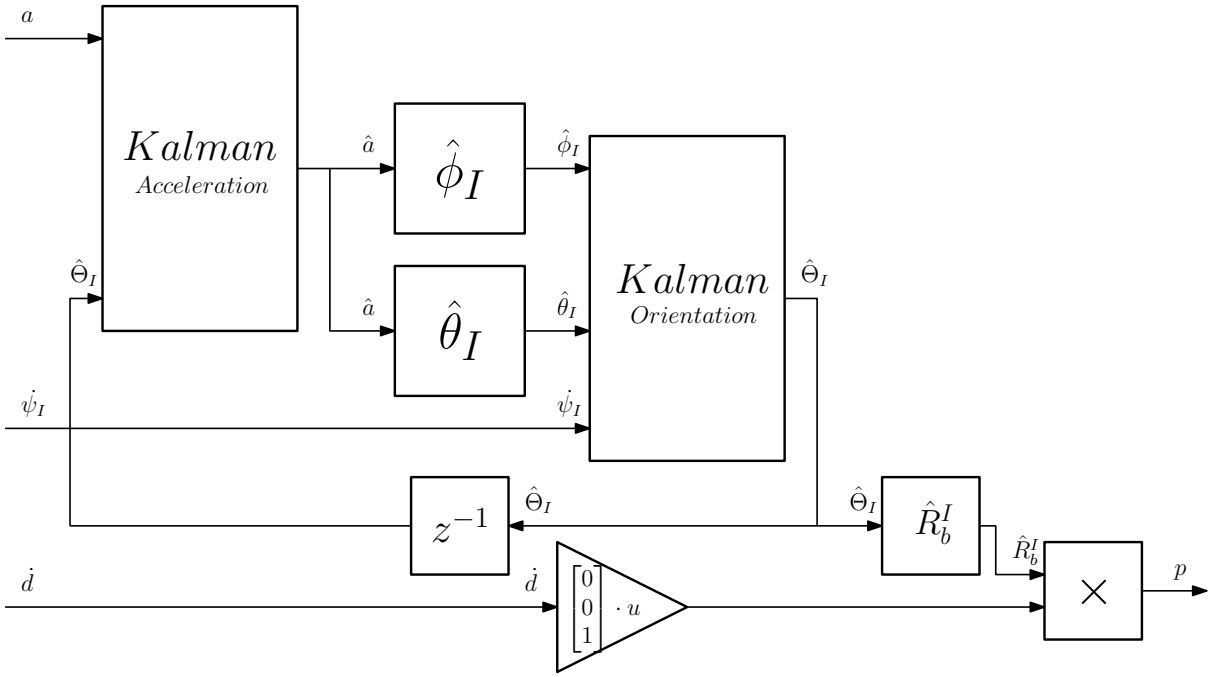

Figure 11.10: Kalman position estimate block diagram. Rotation from the frame of the sensor to the frame of the bit is not included to reduce complexity of the diagram. The acceleration filter acts as an observer to smooth out noisy raw acceleration data. The Kalman filter takes the current best estimate of the orientation and uses current measurement to correct. The model assumes that the gravity vector is of magnitude g in the z-axis direction. The position assumes that the bit moves in the direction of the current bit orientation.

Expected deviation of the estimate can be extracted from the Kalman filter. The covariance matrix described in Equation 5.43 contains the current variance of the best estimate. Variance is the square of the expected deviation from the true state value.

11.4.5 System State Simulation in Simulink

Simulink will try to accurately simulate the dynamics of the system using a solver. The ideal simulation is able to closely replicate the dynamics of the model while being reasonably computationally demanding. A common approach is to use a Runge-Kutta based solver [39]. These have the advantage of being able to adjust the time-step based on tolerances of simulation accuracy rather than having a fixed time-step. This is generally more computationally efficient since a fixed time-step has to be small enough to simulate the fastest dynamics of the model.

A drawback of using a variable step solver is that the simulation output of a non-continuous system may be inaccurate. A state based system may be non-continuous when the state is changed. By default the solver will not make an effort to find out when a state would have changed to reduce the computational cost. This is generally preferred since the solver is intended to replicate the model dynamics rather than the state machine, and a change of state may not affect the dynamics.

For applications where knowing the exact time a state is changed is a requirement for an accurate simulation it is possible to enable Zero-Crossing detection. The system tracking the well path position behaves differently when running with a variable step size compared to a fixed time-step. Running fixed step simulations is inefficient, so variable sized simulations are preferred.

Zero-Crossing detection will decrease the time-step when the input has changed sign after a time-step [40]. In the case of the well path logger, the intention is to log a point each time MD has moved a specific distance. The last saved point is held in a state logic with a state transition each time a length of MD is moved from the last log point. The drawback of this approach is that the simulation is more computationally demanding as it has to decrease the step-size more often. The result is that the system is able to save positions with an close to exact distance between them. This is not representative of a discrete time system, but the deviation will be minuscule as the position is frequently sampled and movement of the bit is slow. Compared to an operation on the physical rig, the logging would occur closely to the target value as the system movements are minuscule between each sample. With zero-crossing enabled in the variable step simulation the path logging closely resembles the output of a fixed step simulation or a physical rig.

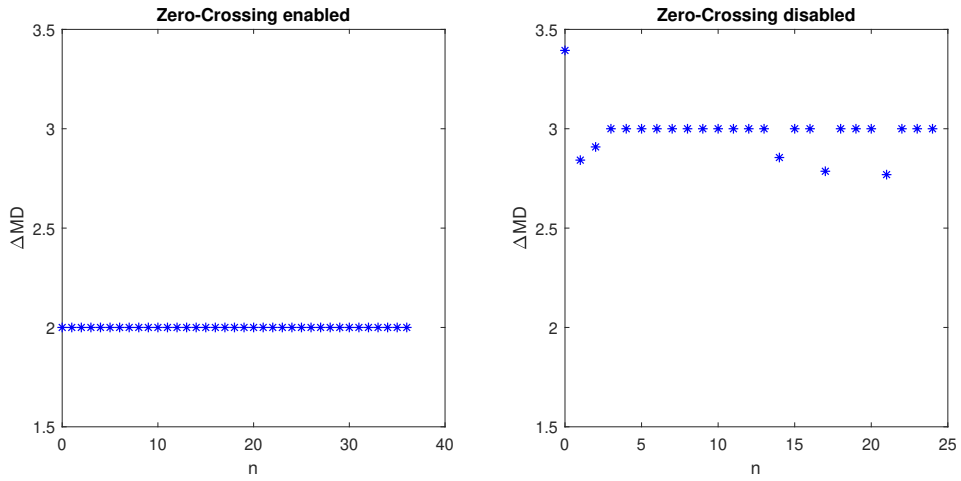

Figure 11.11: Difference in MD where the path logger set to log every 2cm of MD with and without Zero-Crossing detection. Notice also that there are fewer points overall without Zero-Crossing detection.

11.5 Future Improvements

Experimental data will enable the plant model to be tuned more closely to the physical rig. It is also possible to estimate the ROP using a digital twin, however this has a low priority for this years competition.

12 Finance

The Drillbotics Guidelines limits the budget of each team in the competition to 10,000 USD. Equipment and tools already present at the rig from previous years will not be included in the budget. Rig modifications are expected to account for the largest expenses this year. The budget does not consider salaries for everyone involved with the project. Even with modest salary estimates, the expense of salaries would far exceed the equipment costs.

12.1 Budget

The current budget status is presented in Table 12.1. All expenses excluding salaries for in-house personnel is included. The limited budget requires careful consideration to accomplish this year's setup and competition goals described in section 4. The team has allocated the majority of the budget for Phase II to be used on equipment and components for the mechanical and electrical system, rock samples for test drilling, and tools for assembling the system. All costs are presented in United States dollar (USD) based on the conversion rate a the time of the purchase, and the budget is based on the limit of 7,500 USD. So far, a total of 2,350.62 USD is spent, which leaves a net 5,148.38 USD for Phase II.

Table 12.1: Cost of items acquired for the drilling rig setup.

Component	Price per item (USD)	Quantity	Total Cost (USD)
Drill Chuck	43.42	1	43.42
Gearbox	626	1	626
Servomotor + Driver	602	1	602
Shipping Gearbox and Servomotor	135	1	135
Universal joints	27.41	2	54.82
Radial ball bearings	30.92	4	123.68
Drill pipes	2.57	110	282.7
Rods	1.1	120	132
Shipping drill pipes and rods	182	1	182
Generic drill bit 1	23	3	69
Generic drill bit 2	20	5	100
Total Cost (USD)			**$ 2,350.62**
Balance (USD)			**$ 5,148.38**

12.2 Funding

The guidelines state that:

Teams selected to advance to the second phase must limit the cost of the physical or virtual rig and materials to US$ 10,000 or its equivalent in other currencies. [52]

As a consequence from the pandemic virus Covid-19 that spread globally in 2020, the NTNU team is recommended from the administration at the university to keep the expenditures below 7.500 USD. However, should it be necessary, 10,000 USD would be fully covered by the collaboration between NTNU and BRU21.

A sponsorship has been established between the NTNU team and Lyng Drilling for the design of miniature drilling bits. Lyng Drilling is a Schlumberger company located outside Trondheim specializing in drill bit technology for the North Sea [25]. The company will provide expertise and assistance in the custom bit design process. Lyng drilling will manufacture the drill bit when the design is finalized. The collaboration is a major advantage for the team because the drill bit can be fully customized to fit the requirements of the competition and the mechanical concept of the rig.

12.3 Transport Expenses

Normally, the Drillbotics competition is held in Celle, Germany. A portion of the budget has therefore been allocated for travel expenses for the team members as well as expenses related to shipping of the rig. The cost of shipment of the drilling rig will be the biggest cost within the travel expenses. It is expensive to transport large mechanical structures from Norway to Germany because of customs regulations. Based on previous years budget, this is estimated to cost approximately 3,000 USD. The traveling crew from Trondheim are 4 team members and 4 professors. Round trip tickets are estimated to approximately 200 USD per person and result in a total of 1,600 USD. The total travel expenses for transport of personnel and rig ends up at a total of 4,600 USD.
However, with the ongoing Covid-19 situation, the location of competition is unknown but the team will assume that the competition will be held in Germany and acknowledge that this is subject to change.

13 Conclusion

The team has throughout Phase I made major progress towards participating in the 2021 Drillbotics competition. The drilling concept is changed from a PDM motor to a rotating rod transmitting torque from the top drive motor through the drill pipe to the drilling bit. The rig has been mechanically re-designed for the new concept. The rod concept allows for high inclination deviated drilling without the use of a downhole motor. With the new choice of drill pipe material, the system is able to build larger angles and meet the competition requirements.

A new BHA and hydraulic swivel has been designed to fit the new system. The concept of the hoisting system is unchanged from last years drilling rig. The hydraulic system was redesigned to be compatible with the rotating rod and bi-directional rotation. A bent sub angle of 4.57 ° is expected to build a predictable deviated well path where the orientation of the BHA can be controlled by the azimuth control system for directional drilling. The azimuth control system is an additional servo motor connected to a hollow shaft gearbox for orientating the drill pipe and bent sub. Controlling the orientation of the BHA throughout the drilling operation makes it possible to steer the bit in azimuth and inclination to intersect the target points.

The BHA was re-designed to fit the concept of a rotational rod. The BHA is given a more robust design to improve weak threads and components. The sensor housing is modified to allow for electrical conductors outside the drill pipe, and the bit connection to the BHA is changed to avoid sand problems. A custom bit has been designed in collaboration with Lyng Drilling. The bit design is currently being finalized for production early next year.

New servo motors has been acquired based on extensive research into automation protocols. All inputs and sensors are ready for integration into the system. The new control system has a more unified automation protocol structure than previous years which should reduce the time spent on hardware integration. A bit movement model has been created based on the mechanical characteristics of the rig. The model assumes that the bit moves in the direction of its current orientation with a build rate equal to the DLS. A digital twin has been developed to enable testing of position estimation, well path generation, and well path reference control. The digital twin is based on the system model. Inputs and measurements are simulated with artificial process and measurement noise.

14 Future Work

The concept of the mechanical design on the 2021 Drillbotics rig has been designed, finalized and presented in this report. All parts are ordered or under manufacturing, and should be present in the workshop at the start of Phase II. The next step is to assemble the rig with each new component, and ready it for testing and optimization.

Phase II will consist of testing and tweaking to enter the competition in June with the best possible system. Phase II will introduce challenges not yet considered, which has to be accounted for. The BHA is currently designed, but not yet tested in any matter. From testing results, the BHA will require tweaks and tuning to work as intended. The biggest pitfalls regarding this design will be the transmission section respectively with the connection between the rotating rod and the universal joint, the sensor housing and signal transferring, and the metal-to-metal connection between the bit sub and the bearing packer. The hydraulic swivel is currently designed, but not yet produced or tested. The biggest pitfalls regarding this design will be the seal around the rotating rod in which may lead to leakage near the gearbox. Measures to avoid this should be considered in Phase II.

A low-level hardware control system is yet to be implemented. The control system software will either be implemented in Simulink or LabVIEW depending on hardware support. Low-level control will have a high priority early in Phase II to allow for mechanical testing and drilling data acquisition. The downhole sensor must be programmed and integrated. The digital twin has currently no control system. This will be integrated in Phase II with a well path reference controller. nMPC and MPC control will be tested. The well path reference generator must be implemented such that the well path reference controller can have a shorter prediction horizon. Cubic spline and cost function will be tested in the digital twin with a well path reference controller. The control system of the digital twin will be used to control the physical rig where the digital twin is replaced with rig inputs and measurements. The modelled Kalman position estimate system will be tested while drilling in an attempt to replicate the simulated results in the digital twin.

References

[1] A.J. Adams et al. “The Barlow Equation for Tubular Burst: A mudded History”. In: *Society of Petroleum Engineers* (Mar. 6, 2018). URL: https://doi.org/10.2118/189681-MS.

[2] A.T. Bourgoyne Jr et al. *Applied Drilling Engineering*. 2nd ed. Society of Petroleum Engineers, 1991.

[3] B. Brechan et al. *Drilling, Completion, Intervention and PA - design and operations*. Department of Geoscience and Petroleum, 2017.

[4] H.E. Helle et al. *Design Report NTNU - Drillbotics 2018 Phase I*. Specialization Project. Department of Geoscience and Petroleum, 2018.

[5] J. Mannsverk et al. *Design Report NTNU - Drillbotics™ 2020 Phase I*. Specialization Project. Department of Geoscience and Petroleum, 2019.

[6] Aplisens. *Pressure Transmitter PCE-28*. URL: https://aplisens.com/pc-28.html. Accessed: 13.12.2020.

[7] A. Austin and J.H. Swannell. “Stresses in a pipe bend of oval cross-section and varying wall thickness loaded by internal pressure”. In: *International Journal of Pressure Vessels and Piping* 7.3 (1979), pp. 167–182. ISSN: 0308-0161. DOI: https://doi.org/https://doi.org/10.1016/0308-0161(79)90016-4. URL: http://www.sciencedirect.com/science/article/pii/0308016179900164.

[8] J.J. Azar and G. Robello Samuel. *Drilling Engineering*. PennWell Books, 2007.

[9] *Bosch Drill Chuck*. URL: https://no.rs-online.com/web/p/drill-accessories/6296409/.

[10] DSATS. *About DSATS*. URL: https://connect.spe.org/dsats/home. Accessed: 24.11.2020.

[11] ASM - Aerospace Specifications Metals Inc ed. *ASM Material Data Sheet*. URL: http://asm.matweb.com/search/SpecificMaterial.asp?bassnum=MA6061T6. Accessed: 05.10.2020.

[12] ASM - Aerospace Specifications Metals Inc ed. *ASM Material Data Sheet*. URL: http://asm.matweb.com/search/SpecificMaterial.asp?bassnum=MA7075T6. Accessed: 24.11.2020.

[13] Baker Hughes ed. *NAVI-DRILL MOTOR HANDBOOK*. 2002.

[14] Cat Pumps ed. *Data Sheet - 5CP Plunger Pumps*. URL: http://www.catpumps.com/%20products/pdfs/5CP6120_E.pdf. Accessed: 03.12.2020.

[15] Enggcyclopedia ed. *Absolute Pipe Roughness*. URL: https://www.enggcyclopedia.com/2011/09/absolute-roughness/. Accessed: 12.10.2020.

[16] Kruge ed. *Elastisitetsmodul og flytegrense R_e for stål (Temperaturavhengig)*. URL: https://www.kruge.no/mediabank/store/2/2586/Elastisitetsmodul-og-flytegrense-Re-for-stAxl-Temperaturavhengig.pdf. Accessed: 05.10.2020.

[17] MechaniCalc ed. *Column Buckling*. URL: https://mechanicalc.com/reference/column-buckling. Accessed: 30.09.2020.

[18] MechaniCalc ed. *Cross Section Properties*. URL: https://mechanicalc.com/reference/cross-sections#radius-of-gyration. Accessed: 30.09.2020.

[19] Micon Downhole Tools ed. *Positive Displacement Motors (PDM)*. URL: https://micon-drilling.de/Download/Catalog_PDM_EN.pdf. Accessed: 30.09.2020.

[20] Petrowiki ed. *Cuttings transport*. URL: https://petrowiki.org/Cuttings_transport. Accessed: 08.10.2020.

[21] Petrowiki ed. *Directional Deviation Tools*. URL: https://petrowiki.org/Directional_deviation_tools. Accessed: 29.09.2020.

[22] Schlumberger ed. "Drill bit cutting structure - Basic informatio"". Schlumberger private. -.

[23] Schlumberger ed. *Neyfor Turbodrill Handbook*. URL: https://connect.slb.com/~/media/Files/drilling/brochures/directional_drilling/neyrfor_spec_handbook.pdf. Accessed: 03.12.2020.

[24] Schlumberger ed. *PowerPak - Steerable Motor Handbook*. URL: https://www.slb.com/-/media/files/drilling/brochure/powerpak-handbook-br.ashx. Accessed: 30.09.2020.

[25] Kristoffer Fjeldvaer. *Lyng Drilling, a Schlumberger company*. URL: https://fosenindustri.no/medlemmer/lyng-drilling-a-schlumberger-company/.

[26] Maxon Group. *DCX 26L Specifications*. URL: https://www.maxongroup.com/medias/sys_master/root/8841087189022/EN-94.pdf. Accessed: 09.12.2020.

[27] M.U. Azam H.E. Helle and J.M. Montoza. *Design and Implementation of an Autonomous Miniature Drilling Rig for Directional Drilling*. Thesis. Department of Geoscience and Petroleum, 2019.

[28] Helsenorge. *How to prevent transmission*. URL: https://www.helsenorge.no/en/coronavirus/how-to-prevent-transmission/. Accessed: 14.10.2020.

[29] Hilscher. *Hilscher NT-100-RE-EN*. URL: https://www.hilscher.com/products/product-groups/gateways/for-the-control-cabinet-ip20/fieldbus-gateways/nt-100-re-enecsomb/?&techCats=10,13&techTypeMaster=1&techTypeSlave=1. Accessed: 09.12.2020.

[30] Hypoid. URL: https://5.imimg.com/data5/VT/DC/CF/SELLER-2308089/hypoid-gear-rotary-table.pdf.

[31] National Instruments. *LabVIEW*. URL: https://www.ni.com/en-no/shop/labview.html. Accessed: 03.12.2020.

[32] National Instruments. *USB-6212*. URL: https://www.ni.com/en-no/support/model.usb-6212.html. Accessed: 14.12.2020.

[33] Fridtjov Irgens. *Fasthetslære*. 7th ed. Tapir Akademisk Forlag, 2006.

[34] B.A. Foss J.G. Balchen T. Andersen. *Reguleringsteknikk*. Institutt for teknisk kybernetikk, 2016.

[35] Henning Johansen. *Aksler*. URL: https://materialteknologi.files.wordpress.com/2018/01/sb-aksler-kompendium.pdf. Accessed: 24.10.2020.

[36] Silicon Labs. *EMF32G Datasheet*. URL: https://www.silabs.com/documents/public/data-sheets/efm32g-datasheet.pdf. Accessed: 08.12.2020.

[37] Lenze. *Catalog GST GFL gearboxes with MD MH AC motors*. URL: https://download.lenze.com/TD/GST%5C%20GFL%5C%20gearboxes%5C%20with%5C%20MD%5C%20MH%5C%20AC%5C%20motors__v1-0__EN.pdf. Accessed: 08.12.2020.

[38] AZO Materials. *Beryllium Copper UNS C17200*. URL: https://www.azom.com/article.aspx?ArticleID=6326. Accessed: 24.11.2020.

[39] MathWorks. *MathWorks ode45*. URL: https://www.mathworks.com/help/matlab/ref/ode45.html. Accessed: 06.10.2020.

[40] MathWorks. *MathWorks Zero-Crossing Detection*. URL: https://www.mathworks.com/help/simulink/ug/zero-crossing-detection.html. Accessed: 06.10.2020.

[41] MathWorks. *Simulink*. URL: https://www.mathworks.com/help/simulink/. Accessed: 03.12.2020.

[42] MathWorks. *Understanding Kalman Filters: An optimal estimator algorithm*. URL: https://www.mathworks.com/videos/understanding-kalman-filters-part-3-optimal-state-estimator--1490710645421.html. Accessed: 07.10.2020.

[43] MathWorks. *Understanding Kalman Filters: Nonlinear state estimators*. URL: https://www.mathworks.com/videos/understanding-kalman-filters-part-5-nonlinear-state-estimators-1495052905460.html. Accessed: 08.10.2020.

[44] mhwirth. *Automation and Software*. URL: https://mhwirth.com/our-products/control-and-automation/automation-and-software/. Accessed: 20.10.2020.

[45] S. Menand (Armines/Ecole des Mines de Paris) — H. Sellami (Armines/Ecole des Mines de Paris) — C. Simon (DrillScan). *PDC Bit Classification According to Steerability*. URL: https://doi.org/10.2118/87837-PA. Accessed: 19.11.2020.

[46] Moons. *Moons SM0402AE4-KCD-NNV*. URL: https://www.moonsindustries.com/p/m2dv-series-ac-servo-motors/sm0402ae4-kcd-nnv-000004611170000217. Accessed: 09.12.2020.

[47] M.B. Nåmdal. *Design and Implementation of an Autonomous Miniature Drilling Rig for Directional Drilling*. Thesis. Department of Engineering Cybernetics, 2019.

[48] M.B. Nåmdal. *Design and Implementation of Instrumentation and Control System for an Autonomous Miniature Drilling Rig for Directional Drilling*. Thesis. Department of Engineering Cybernetics, 2019.

[49] NOV. *NOVOS Reflective Drilling System*. URL: https://www.nov.com/products/novos. Accessed: 20.10.2020.

[50] J.T. Gravdahl O. Egeland. *Modelling and Simulation for Automatic Control*. Norwegian University of Science and Technology, 2003.

[51] ODVA. *EtherNet/IP - CIP on Ethernet Technology*. URL: https://www.odva.org/wp-content/uploads/2020/05/PUB00138R6-Tech-Series-EtherNetIP.pdf. Accessed: 18.10.2020.

[52] Society of Petroleum Engineers (SPE) and Drilling systems Automation Technical Section (DSATS) ed. *Drillbotics™Guidelines*. URL: https://drillbotics.com/wp-content/uploads/simple-file-list/Guidelines/Guidelines-2021/2021-Drillbotics-Guidelines-v3.pdf. Accessed: 05.09.2020.

[53] Bonmach Q.D. *The difference between 3 rock drilling methods — Rotary drilling, DTH drilling, and Top Hammer drill*. URL: https://medium.com/@qdbonmach/the-difference-between-3-rock-drilling-methods-rotary-drilling-dth-drilling-and-top-hammer-efe5789a08e2. Accessed: 03.12.2020.

[54] S. Chen — R. Arfele — S. Anderle — J. Romero. *A new theory on cutter layout for improving PDC-Bit performance in hard-and transit-foramtion drilling*. URL: https://www.onepetro.org/download/journal-paper/SPE-168224-PA?id=journal-paper%2FSPE-168224-PA. Accessed: 15.11.2020.

[55] B. Brechan S. Hovda and P. Skalle. *Introduction to Drilling Engineering*. Department of Geoscience and Petroleum, Feb. 12, 2019.

[56] Sekal. *Introducing DrillTronics*. URL: https://sekal.com/products/drilltronics/. Accessed: 20.10.2020.

[57] Siemens. *Advantages with PROFINET*. URL: https://new.siemens.com/us/en/products/automation/industrial-communication/profinet/advantage.html. Accessed: 18.10.2020.

[58] Sintef. *Autonomous systems*. URL: https://www.sintef.no/en/autonomy.

[59] Bjørn A. Brechan — Anisa N. Corina — Tor B. Gjersvik — Sigbjørn Sangesland — Pål Skalle. “”Compendium TPG4215 Drilling Engineering””. University compendium. 2017.

[60] TDK. *TDK ICM-20948 Datasheet*. URL: https://invensense.tdk.com/wp-content/uploads/2016/06/DS-000189-ICM-20948-v1.3.pdf. Accessed: 08.12.2020.

[61] AEP Transducers. *TC4-AMP AEP Transducer*. URL: https://www.aep.it/prodotto/trasduttori-di-forza/tc4-amp/. Accessed: 24.11.2020.

[62] *Tungsten carbide*. Dec. 2020. URL: https://en.wikipedia.org/wiki/Tungsten_carbide.

[63] Göran Tuomas. *System for Water-Driven Downhole Hammer Drilling*. Jan. 2001. URL: https://www.onepetro.org/download/conference-paper/OTC-13097-MS?id=conference-paper%5C%2FOTC-13097-MS.

[64] Wikipedia. *CANopen*. URL: https://en.wikipedia.org/wiki/CANopen. Accessed: 18.10.2020.

[65] Wikipedia. *EtherCAT*. URL: https://en.wikipedia.org/wiki/EtherCAT. Accessed: 18.10.2020.

[66] Wikipedia. *EtherNet/IP*. URL: https://en.wikipedia.org/wiki/EtherNet/IP. Accessed: 18.10.2020.

[67] Wikipedia. *Modbus*. URL: https://en.wikipedia.org/wiki/Modbus. Accessed: 18.10.2020.

[68] Wikipedia. *OSI Model*. URL: https://en.wikipedia.org/wiki/OSI_model. Accessed: 18.10.2020.

[69] Wikipedia. *Transmission Control Protocol*. URL: https://en.wikipedia.org/wiki/Transmission_Control_Protocol. Accessed: 18.10.2020.

Appendices

A Summary of Equations

Table A.1: Summary of equations.

Calculated	Equation	Result	Reference
Dogleg Severity	$DLS = \frac{\pi}{Cl}$	$56.4°/m$	Equation 5.1
Course Length	$CL = \frac{RC\pi(I_2-I_1)}{180}$	$53.2cm$	Equation 5.3
Bit Tilt	$\theta = \frac{DLS(L_1+L_2}{2}$	$4.57°$	Equation 5.5
Maximum Allowable WOB	$F_{max,WOB} = \sigma_{cr}A$	Table 8.2 & 8.3	Equation 5.12
Burst Pressure	$P_{burst} = 2\frac{0.875\sigma_{yield}t}{OD\ SF}$	$385 \cdot 10^5 Pa$	Equation 5.13
Twist-Off Torque	$T_{max} = \tau_{max}\frac{\pi}{16}(OD^2 - ID^2)(OD + ID)$	Table 8.4	Equation 5.14
Twist-Off Limit rod	$M_s = \tau_s \cdot W_p$	$2.8Nm$	Equation 5.21
Axial Stress from Pressure	$\sigma_z^p = \frac{(\frac{ID}{OD})^2}{1-(\frac{ID}{OD})^2}p$	Figure 8.2 & 8.4a	Equation 5.18
Axial Stress from WOB	$\sigma_x^{WOB} = \frac{WOB}{A_{cs}}$	Figure 8.2 & 8.4a	Equation 5.19
Axial Stress from Bending	$\sigma_z^b = \frac{E}{RC}y$	Figure 8.3 & 8.4b	Equation 5.20
Comparative Stress	$\sigma_c = \sqrt{\sigma_b^2 + 3\tau_s^2}$	Figure 8.5	Equation 5.23
Laminar Slip Velocity	$v_{sl} = \frac{d_s^2 g(\rho_s-\rho_f)}{18\mu_f}$	Table 8.6	Equation 5.24
Slip Velocity	$v_{sl} = \sqrt{\frac{4(\rho_s-\rho_f)gd_s^2}{3f\rho_f}}$	Table 8.6	Equation 5.25
Flow Rate	$q = A_{cs}\frac{v_{sl}}{1-R_t}$	Table 8.6	Equation 5.26
Pipe Pressure Losses	$\Delta P_i = f_i\frac{L_i}{dh,i}\frac{\rho_f v_i^2}{2}$	Table 8.7	Equation 5.28
Bit Nozzle Pressure Loss	$\Delta P_{nozzle} = \frac{\rho_f q^2}{2A_n^2 C_d^2}$	Table 8.7	Equation 5.33

B Cuttings Transportation Derivation

To get sufficient hole cleaning, the buoyant force and viscous drag force caused by drilling fluid has to overcome gravitational force and slip velocity acting on the cutting particle. Slip velocity is caused by the weight of the solid particle given by Equation B.1.

$$W = -\rho_s \frac{\pi}{6} d_s^3 g \tag{B.1}$$

where $W[N]$ is the weight force, $\rho_s[kg/m^3]$ is the density of the solid particle and d_s is the solid particle diameter. The buoyant force acting on the particle is estimated with Equation B.2

where $F_b[N]$ is the buoyant force and $\rho_f[kg/m^3]$ is the density of the drilling fluid.

$$F_b = \rho_f \frac{\pi}{6} d_s^3 g \tag{B.2}$$

The vicous drag force is given by [20]:

$$F_d = 3\pi \mu_f d_s v_{sl} \tag{B.3}$$

where $\mu_f[Pas]$ is the fluid visocity and $v_s l[m/s]$ is the slip velocity. By applying Newton's first law of motion given in Equation B.4 to Equation B.1 B.2 and B.3, it can be solved for $v_s l$.

$$\sum F = W + F_b + F_d = 0 \tag{B.4}$$

$$v_{sl} = \frac{d_s^2 g(\rho_s - \rho_f)}{18\mu f} \tag{B.5}$$

Equation B.5 is also known as Stokes' law and is only valid for Newtonian fluids in laminar flow and Reynolds numbers below 0.1[2]. If $Re > 0.1$ the low regime has shear force given as [3]:

$$F_d = f \frac{\pi}{8} d_s \rho_f v_{sl}^2 \tag{B.6}$$

where f is an empirical friction factor found from Figure B.1. Here sphericity, Ψ, is set to be equal to 1 under the assumption of spherical cuttings. Reynolds number is calculated with Equation B.7, using estimated slip velocity from Equation B.5.

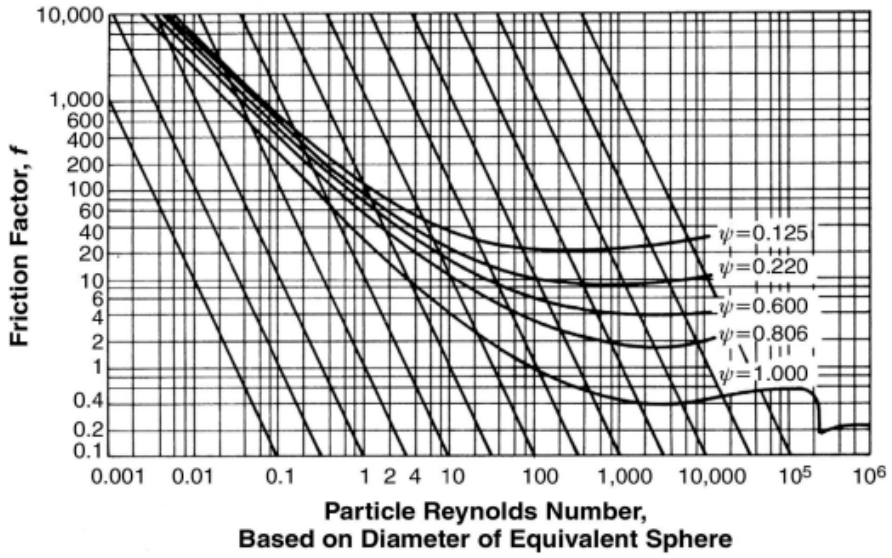

Figure B.1: Relationship between *Re* and f for settling particles in Newtonian fluids [2].

$$Re = \frac{\rho_f v_{sl} d_h}{\mu_f} \tag{B.7}$$

where d_h is the hydraulic diameter. For flow in annulus, area is given as:

$$d_h = OD_{hole} - OD_{DP/BHA} \tag{B.8}$$

and for flow inside pipe:

$$d_h = ID_{DP/BHA} \tag{B.9}$$

By using Equation B.4 with Equation B.6 as F_d, slip velocity of a particle in all flow regimes can be estimated as:

$$v_{sl} = \sqrt{\frac{4(\rho_s - \rho_f) g d_s^2}{3 f \rho_f}} \tag{B.10}$$

C MATLAB Scripts

C.1 Wellpath

```
figure(1)
run cube
set(findall(gca,'Type','Line'),'LineWidth',1.25);
set(gca,'FontSize',12)
X = [0 0];
Y = [0 0];
Z = [0 4];
n = 4000;
phi = linspace(-pi*15/180,pi*15/180,n);
z = linspace(4,24,n);
tm = 30*pi/180;
xmax = sqrt((1-cos(tm))/((1+cos(tm))))*(z(end)-z(1));
RC = ((z(end)-z(1))^2+xmax^2)/(2*xmax);
r = RC*(1-sqrt(1-((z-z(1))/RC).^2));
plot3(X,Y,Z,'b')
set(gca,'Zdir','reverse')
hold on
for i = 1:n
    x = r(i)*cos(phi);
    y = r(i)*sin(phi);
    plot3(x,y,zeros(1,numel(x))+z(i),'r')
```

```
end
xlim([-12 12])
ylim([-6 6])
zlim([0 24])
set(findall(gca,'Type','Line'),'LineWidth',1.25);
view(40,40)
xticks([-12 0 xmax 12])
xticklabels({'-12','0',num2str(max(x),3),'12'})
yticks([-6 0 max(y) 6])
yticklabels({'-6','0',num2str(max(y),3),'6'})
zticks([0 4 24])
title('Wellpath')
disp(['Horisontal displacement = ', num2str(xmax),' in'])
disp(['Radius of Curvature = ',num2str(RC*0.0254),' m'])
disp(['Inclination = ',num2str(tm*180/pi),'°'])
theta = linspace(0,tm,n);
x = RC*cos(theta)-RC;
z = RC*sin(theta)+4;
MD = 4*0.0254 + theta(end)*RC*0.0254;
CL = tm*RC*0.0254;
DL_angle = theta(end)*180/pi;


disp(['Measured depth = ',num2str(MD),' m'])
disp(['Dog leg angle = ',num2str(DL_angle),'°'])
disp(['Length of curved section = ',num2str(CL),' m'])
disp(['Dog leg severity = ',num2str(DL_angle/CL),' °/m'])
plot3(-x,x*0,z,'r')
```

C.2 Buckling

```
function [] = Buckling(E, ys)
%% Parameters
n = 990;
Conv = 0.0254;                          %           Converting
 ↪  in to meter
t = 0.049 * Conv;                       % [m]
OD = 3/8 * Conv;                        % [m]
ID = 3/8 * Conv - 2 * t;                % [m]
```

```
L = linspace(0.01,1,n);                    % [m]       Length DP,
 ↪  Length rock sample, Length Curvature, Remaining length
K = [0.5, 1/sqrt(2), 0.9, 2.1];            %           Effective
 ↪  length factor, K
g = 9.81;                                  % [m/s2]

%% Calculations
I = pi/64 * (OD^4 - ID^4);                 % [m4]      Second
 ↪  Moment of Area, I
A = pi/4 * (OD^2- ID^2);                   % [m2]      Cross
 ↪  Sectional Area, A
rg = sqrt(I/A);                            % [m]       Radius of
 ↪  gyration, rg

% Slenderness Ratio
SR = zeros(1,n);
for j = 1:n
   SR(j) = L(j)/rg;
end

% Critical Slenderness Ratio
SR_cr = zeros(1,length(K));
for j = 1:length(K)
    SR_cr(j) = sqrt((2*pi^2*E)/(K(j)^2*ys));
end

% Johnsons formula, sigma_cr
S_cr = zeros(n,length(K));
for j = 1:length(K)
    for k = 1:n
        S_cr (k,j) = ys - ((ys * K(j) * L(k))/(2 * pi * rg))^2
         ↪  * 1/E;
    end

end

% Eulers formula, F_cr
F_cr = zeros(n,length(K));
```

```
for j =1:length(K)
    for k = 1:n
        F_cr(k,j) = pi^2*E*I/(K(j)*L(k))^2;
    end
end

% Max WOB with different K values
WOB_max = zeros(n,length(K));
for j = 1:length(K)
    for k = 1:n
        if SR(k) <= SR_cr(j)
            WOB_max(k,j) = S_cr(k,j)*A/g;
        else
            WOB_max(k,j) = F_cr(k,j)/g;
        end
    end
end

%% Plot
plot(L, WOB_max(:,1), L, WOB_max(:,2), L,
 ↪  WOB_max(:,3),L,WOB_max(:,4));
hold on
set(gca,'FontSize',12);
xlabel('Length [m]', 'fontsize', 14)
ylabel('Max WOB [kg]', 'fontsize', 14)
title('Maximum allowable WOB vs Unsupported Length',
 ↪  'fontsize', 14)
legend('K=0.5', 'K=1/sqrt(2)', 'K=0.9','K=2.1')
grid on
xticks([0 0.1 0.2 0.3 0.4 0.5 0.6 0.7 0.8 0.9 1])


end
```

C.3 Pipe Bending

```
% Pipe bending
clear all
close all
```

```
clc
%% Parameters
OD_DP = 3/8*0.0254;             %m
t_DP = 0.049*0.0254;            %m
ID_DP = OD_DP -(2*t_DP);        %m
E_st = 196*10^9;                %Pa
E_al = 68.9*10^9;               %Pa
sigma_ys_st = 290*10^6;         %Pa
sigma_ys_al = 276*10^6;         %Pa
sigma_ys_fat_al = 96.5*10^6;    %Pa
n = 100;

sigma_x = 505*10^6;             %Pa
E_x = 71*10^9;                  %Pa

%% Calculations
RC = linspace(0,5,n);           %m
WOB = linspace(0,500,n);        %N
p = linspace(0,100,n);          %bar
A = pi/4*(OD_DP^2-ID_DP^2);     %m^2
y = OD_DP/2;                    %m
I = pi/64*(OD_DP^4-ID_DP^4);    %m^4
M = E_x*I./RC;                  %Nm
sigma_zb = M*y/I;               %MPa
sigma_zwob = WOB/A;             %MPa
sigma_zp = ((ID_DP/OD_DP)^2)/(1-(ID_DP/OD_DP)^2)*p*10^5;   %MPa

%% Plots
figure(1)
a = axes('units','normalized','position',[0.1 0.35 0.8
 ↪  0.6],'xlim',[0 5],'color','red','xtick',0:0.5:5);
plot(RC,sigma_zb,'k')
hold on
plot(p/20,sigma_zp,'b')
plot(WOB/100,sigma_zwob,'r')
ylim([1*10^5 1*10^10])
set(gca,'FontSize',12,'YScale','log')
set(findall(gca,'Type','Line'),'LineWidth',1.25);
```

```
legend('\sigma_z^b','\sigma_z^p','\sigma_z^{WOB}','fontsize',10,'location
ylabel('Stress [Pa]','fontsize',14)
grid on
set(gca,'xcolor','k')
xlabel(a,'Radius of Curvature [m]','Color','k','fontsize',14)
b = axes('units','normalized','position',[0.1 0.21 0.8
 ↪  0.000001],'xlim' ,[0 50],'color','b','xtick',0:10:100);
set(gca,'xcolor','b')
xlabel(b,'Pressure [bar]','Color','b','fontsize',14)
c = axes('units','normalized','position',[0.1 0.10 0.8
 ↪  0.000001],'xlim' ,[0 500],'color','b','xtick',0:50:500);
set(gca,'xcolor','r')
xlabel(c,'WOB','color','r','fontsize',14)

figure(2)
plot(RC,sigma_zb,'r',RC,sigma_zb*0+sigma_x,'k')
xlabel('Radius of Curvature [m]','fontsize',14)
ylabel('Stress [Pa]','fontsize',14)
title('Bending stress vs. Radius of Curvature','fontsize',14)
legend('\sigma_z^b','\sigma_{ys}','fontsize',12,'location','northeast')
set(gca,'FontSize',12)
set(findall(gca,'Type','Line'),'LineWidth',1.25);
grid on
ylim([0 10e8])
```

C.4 Stresses on rod

```
d = 0.004;                    %m
E_st = 196*10^9;              %Pa
E_al = 71*10^9;               %Pa
E_cb = 125*10^9;              %Pa
G_st = 74*10^9;               %Pa
G_al = 26.9*10^9;             %Pa
G_cb = 50*10^9;               %Pa
sigma_ys_st = 290;            %MPa
sigma_ys_al = 505;            %MPa
sigma_ys_cb = 965;            %MPa
sigma_us_st = 580;            %MPa
sigma_us_al = 310;            %MPa
```

```
n = 100;

RC = linspace(0,5,n);           %m
I = pi*d^4/64;                  %m^4

M_b_st = E_st*I./RC;               %Nm
M_v_st = G_st*I./RC;               %Nm

W_x = pi*d^3/32;
W_p = pi*d^3/16;

sigma_b_st = (M_b_st./W_x)/10^6;      %Mpa
sigma_v_st = (M_v_st./W_p)/10^6;      %Mpa
sigma_j_st = sqrt(sigma_b_st.^2+3*sigma_v_st.^2);


figure(1)
plot(RC,sigma_j_st,'b',RC,sigma_j_st*0+sigma_ys_st,'r')
hold on
legend('\sigma_c','\sigma_{ys}^{st}','fontsize',12,'location','NorthEast'
xlabel('Radius of Curvature [m]')
ylabel('Comparative Stress [MPa]')
title('Comparative  stress vs. Radius of
 ↪  Curvature','fontsize',14)
set(findall(gca,'Type','Line'),'LineWidth',1.25)
grid on
xlim([0.5 5])
ylim([0 10e2])

M_b_al = E_al*I./RC;               %Nm
M_v_al = G_al*I./RC;               %Nm

sigma_b_al = (M_b_al./W_x)/10^6;      %MPa
sigma_v_al = (M_v_al./W_p)/10^6;       %MPa
sigma_j_al = sqrt(sigma_b_al.^2+3*sigma_v_al.^2);  %MPa

figure(2)
plot(RC,sigma_j_al,'b',RC,sigma_j_al*0+sigma_ys_al,'r')
```

```
legend('\sigma_c','\sigma_{ys}^{al}','fontsize',12,'location','NorthEast'
xlabel('Radius of Curvature [m]')
ylabel('Comparative Stress [MPa]')
title('Comparative  stress vs. Radius of
 ↪  Curvature','fontsize',14)
set(findall(gca,'Type','Line'),'LineWidth',1.25)
grid on
xlim([0 5])
ylim([0 10e2])

M_b_cb = E_cb*I./RC;                    %Nm
M_v_cb = G_cb*I./RC;                    %Nm

sigma_b_cb = (M_b_cb./W_x)/10^6;        %MPa
sigma_v_cb = (M_v_cb./W_p)/10^6;        %MPa
sigma_j_cb = sqrt(sigma_b_cb.^2+3*sigma_v_cb.^2);    %MPa

figure(3)
plot(RC,sigma_j_cb,'b',RC,sigma_j_cb*0+sigma_ys_cb,'r')
legend('\sigma_c','\sigma_{ys}^{cb}','fontsize',12,'location','East')
xlabel('Radius of Curvature [m]')
ylabel('Comparative Stress [MPa]')
title('Comparative  stress vs. Radius of
 ↪  Curvature','fontsize',14)
set(findall(gca,'Type','Line'),'LineWidth',1.25)
grid on
xlim([0 5])
ylim([0 10e2])
```

C.5 Twist-off pipe

```
%% Parameters
OD_DP = 3/8*0.0254;             %m
t_DP = 0.049*0.0254;            %m
ID_DP = OD_DP -(2*t_DP);        %m
L_DP = 36*0.0254;               %m
E_st = 196*10^9;                %Pa
E_al = 71*10^9;                 %Pa
sigma_ys_st = 290*10^6;         %Pa
```

```
sigma_ys_al = 505*10^6;          %Pa
sigma_ys_fat_al = 96.5*10^6;     %Pa
OD_BHA = 1.42*0.0254;            %m
ID_BHA = 1.04*0.0254;            %m
L_BHA = 3.35*0.0254;             %m
n = 500;
WOB = linspace(0,500,n);         %N
A = pi/4*(OD_DP^2-ID_DP^2);      %m^2
p = 10;                          %bar
%% Calculations no bending
sigma_r0 = (((ID_DP/OD_DP)^2)/(1-(ID_DP/OD_DP)^2))*p*10^5;
sigma_theta0 = (((ID_DP/OD_DP)^2)/(1-(ID_DP/OD_DP)^2))*p*10^5;
sigma_z0 = WOB/A +
 ↪  ((ID_DP/OD_DP)^2)/(1-(ID_DP/OD_DP)^2)*p*10^5;

tau_max0 = sqrt((2*sigma_ys_al.^2-((sigma_z0-sigma_theta0).^2
 ↪  ...
    +(sigma_theta0-sigma_r0).^2+(sigma_r0-sigma_z0).^2))/6);
T_max0 =
 ↪  (tau_max0*(pi/16)*(OD_DP^2-ID_DP^2)*(OD_DP+ID_DP))*10^5;

plot(WOB,T_max0/10^5)
hold on
ylim([20 50])
xlim([0 500])
grid on
%% Calculations bending
RC = [2.13  1.64 1.32 1.01];          %m
r = [2.375 3.19 4 5.39].*0.0254;      %m
y = OD_DP/2;                          %m
I = pi/64*(OD_DP^4-ID_DP^4);          %m^4
for i = 1:length(RC)
    M = E_al*I./RC(i);
    sigma_r = (((ID_DP/OD_DP)^2-(ID_DP/(2*r(i)))^2)...
        /(1-(ID_DP/OD_DP)^2))*p*10^5;
    sigma_theta = (((ID_DP/OD_DP)^2+(ID_DP/(2*r(i)))^2)...
        /(1-(ID_DP/OD_DP)^2))*p*10^5;
```

```
    sigma_z = M*y/I + WOB/A +
     ↪  ((ID_DP/OD_DP)^2)/(1-(ID_DP/OD_DP)^2)*p*10^5;

    tau_max = sqrt((2*sigma_ys_al.^2-((sigma_z-sigma_theta).^2
     ↪  ...
        +(sigma_theta-sigma_r).^2+(sigma_r-sigma_z).^2))/6);
    T_max =
     ↪  (tau_max*(pi/16)*(OD_DP^2-ID_DP^2)*(OD_DP+ID_DP))*10^5;


    plot(WOB,T_max/10^5)
    hold on
    xlabel('Weight On Bit (WOB)  [N]')
    ylabel('Torque [Nm]')
    title('Twist-off torque vs. WOB','FontSize',14)
    legend('No bending stress', '2 3/8" Horizontal
     ↪  Displacement', '3.19" Horizontal Displacement', ' 4"
     ↪  Horizontal Displacement', '5.39" Horizontal
     ↪  Displacement', 'location','SouthWest')
end
```

D Power Consumption

D.1 Top Drive Motor

The Top Drive (TD) motor will be the same motor as the motor in the hoisting system. Its main purpose is to apply rotation and torque to the aluminum rod to the drill bit. The power consumption of the motor is due to this rotation and torque, as found by the following equations:

$$P = \frac{T\omega}{\eta} \tag{D.1}$$

$$\omega = \frac{2\pi N}{60} \tag{D.2}$$

Where $T[Nm]$ is the provided torque, ω is the angular velocity, N is the Revolutions Per Minute (RPM) and η is the motor efficiency.

The motor has a limitation in operational window of 3400 RPM and 45 Nm, and an efficiency of 90%. Given the motor operating at its limits, the power consumption calculated with Equation D.1 and D.2 is equal to 17.8 kW. These values will not be valid for the system on the rig,

where the torque is limited to 2.8 Nm by the rod. With a relative high rotational value of 700 RPM, this will result in a power consumption of **228 W.**

D.2 Hoisting Motor

The hoisting motor applies a rotation to the system that is translated into vertical motion by the ball screw. Equation D.3 can be used to calculate the torque provided by the hoisting motor

$$T = \frac{F \cdot l}{2\pi\epsilon} \tag{D.3}$$

where $T[Nm]$ is the torque, $F[N]$ is the force resulting from the weight of the rotary system, l is the lead of the ball screw, and ϵ is the efficiency of the motor. Equation D.4 gives the provided torque by the hoisting motor, given that the lead of the ball screw is 5mm, weight of the rotary system is estimated to 490 N, and $\epsilon = 90\%$:

$$T = \frac{F \cdot l}{2\pi\epsilon} = \frac{490 \cdot 0.005}{2\pi \cdot 0.9} = 0.433Nm \tag{D.4}$$

With $T = 0.433Nm$, Equation D.1 and D.2 can be used to estimate the power consumption of the motor at different RPMs. The results are given in Table D.1

Table D.1: Estimates of the hoisting motors power consumption at different RPM values.

Rotary Speed N [RPM]	Power Consumption P [W]
100	5.67
300	17
600	34
1200	68
2000	113
3000	170

D.3 Azimuth Motor

D.4 Electrical Miniature Motor

This years plan B solution has an EMM as power source. The chosen electrical miniature motor is able to provide a rotary speed of 70 RPM and a torque of 4.5 Nm as described in section 6.6.1. With these maximal performance values, the power consumption can be calculated with Equation D.1 and D.2. With a efficiency of 91% as given in Figure G.1, the power

consumption of the EMM is estimated to be **36.25 W**.

D.5 Computer

The computer used to control the system of the NTNU Drillbotics rig is a OptiPlex 7440 AIO from Dell. This model is listed with a maximum power consumption of 200 W. This is a relatively powerful computer, and is not expected to operate under maximum performance. It is of that reason reasonable to assume a power consumption of **100 W**.

E BHA components

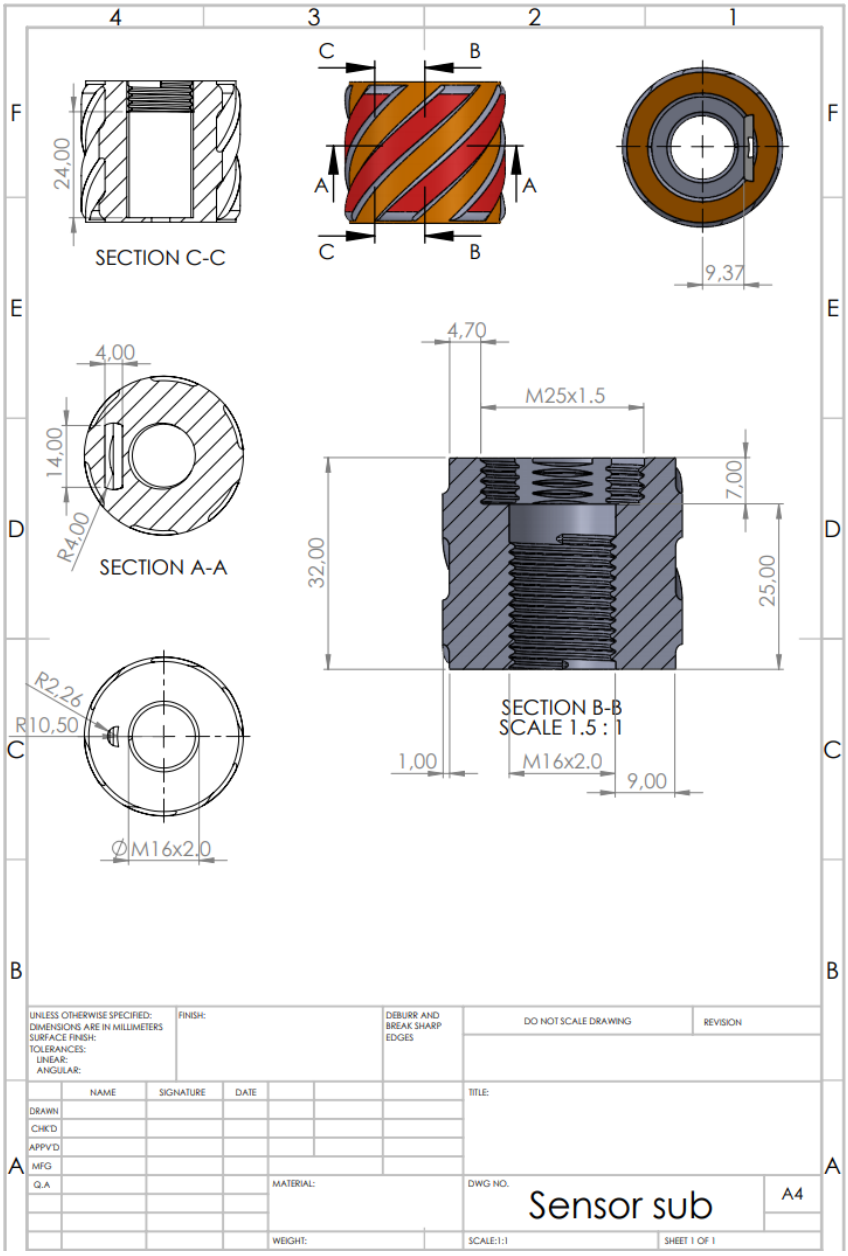

Figure E.1: Sensor housing/Upper stabilizer.

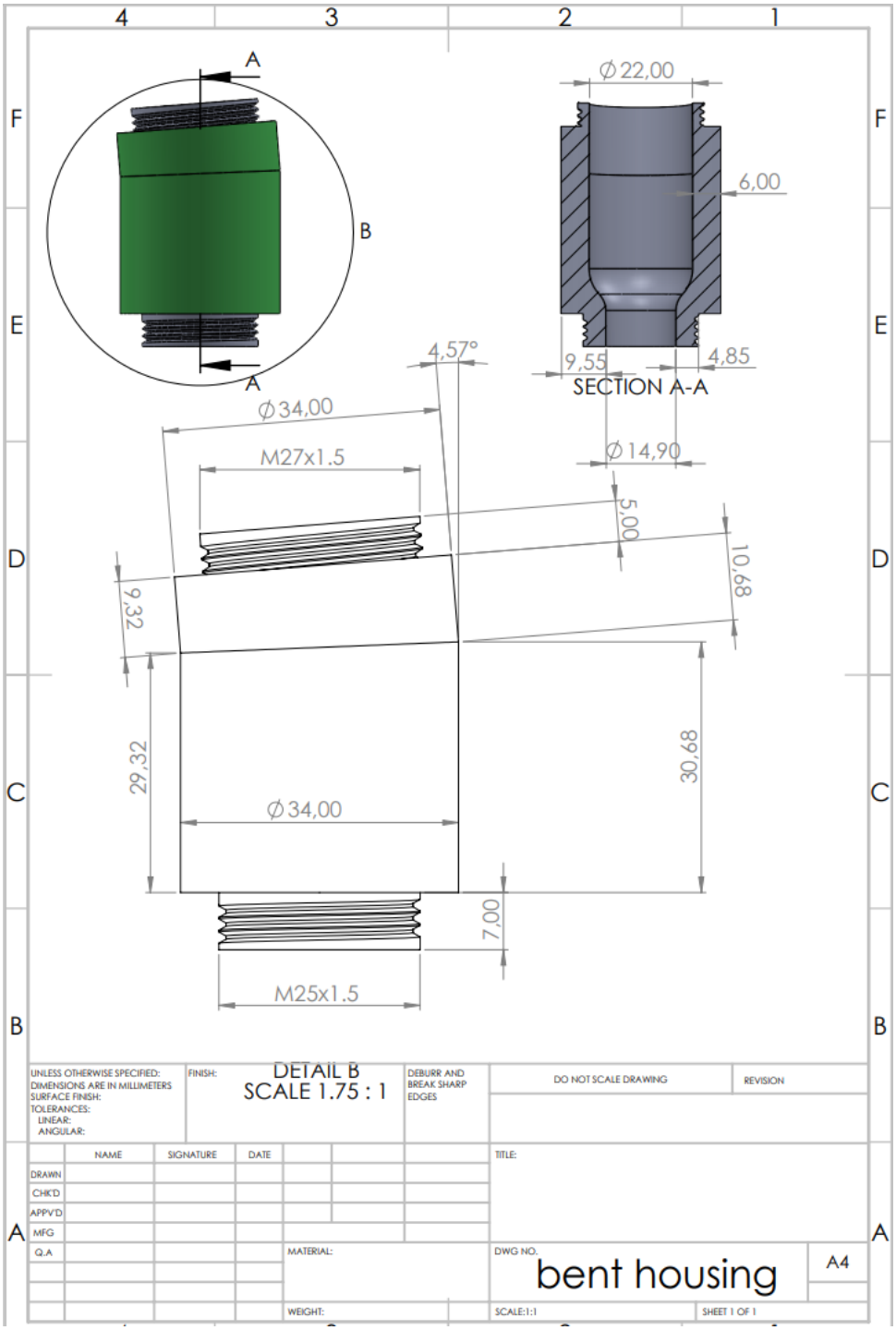

Figure E.2: Bent housing.

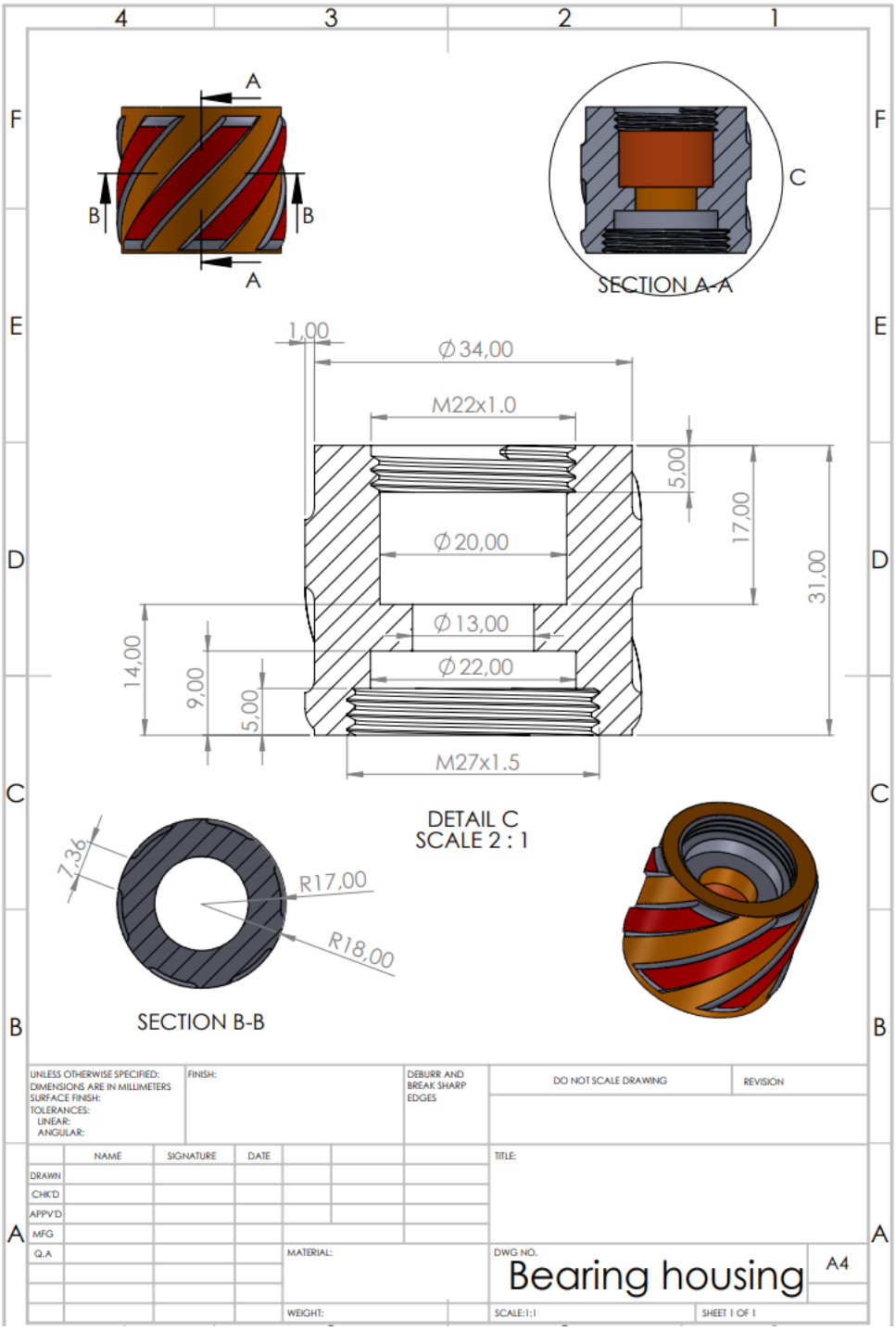

Figure E.3: Bearing Housing.

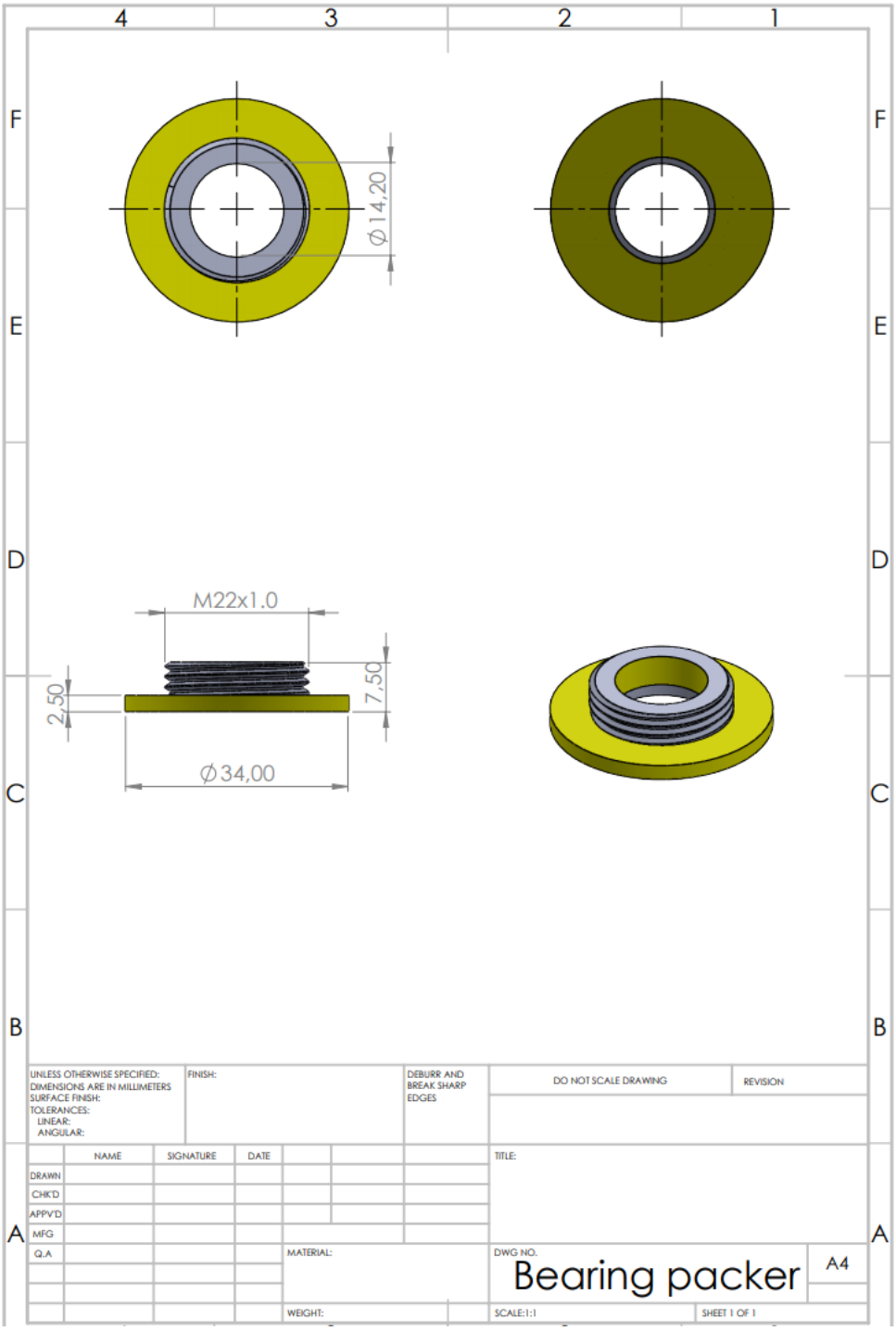

Figure E.4: Bearing Packer.

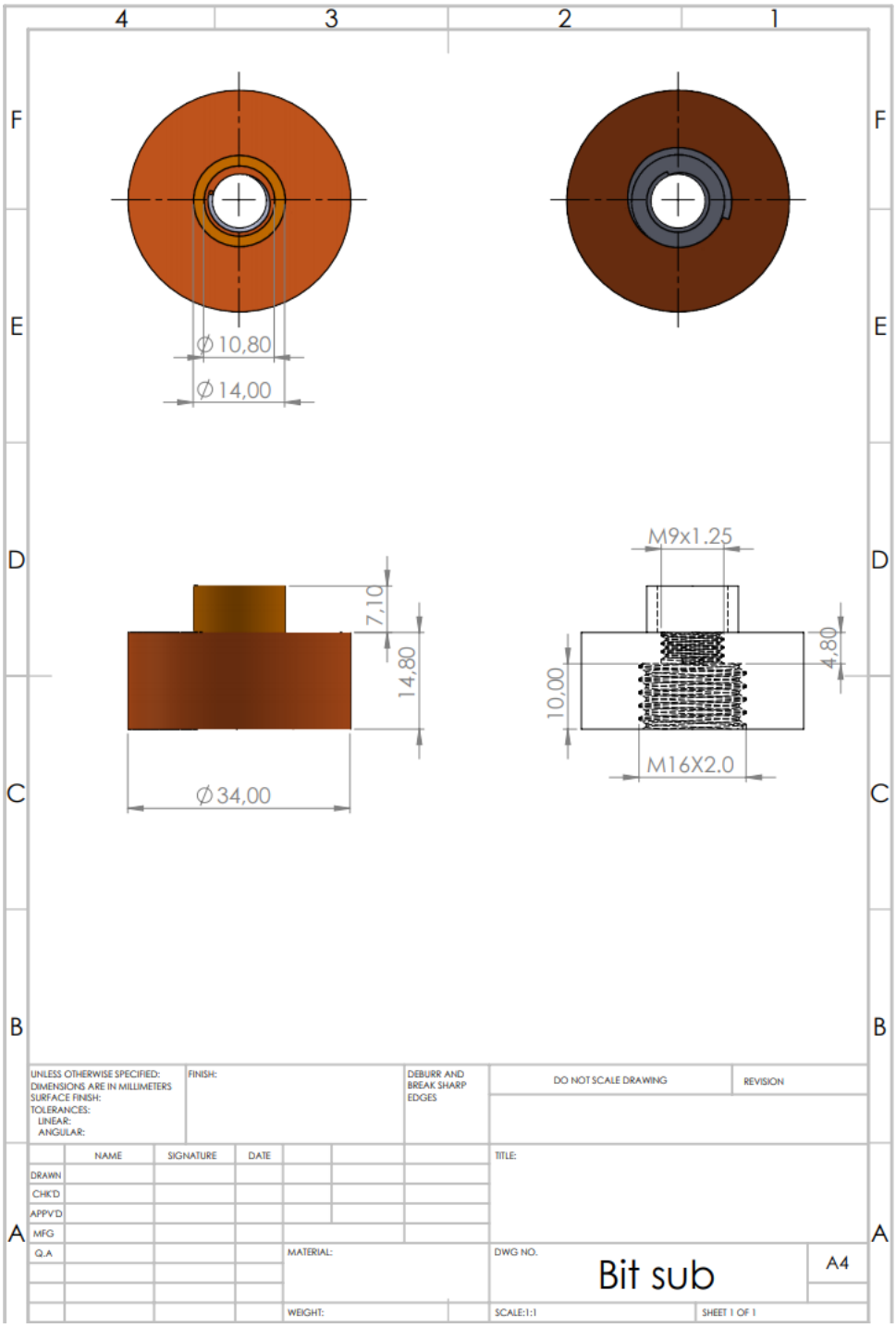

Figure E.5: Bit sub.

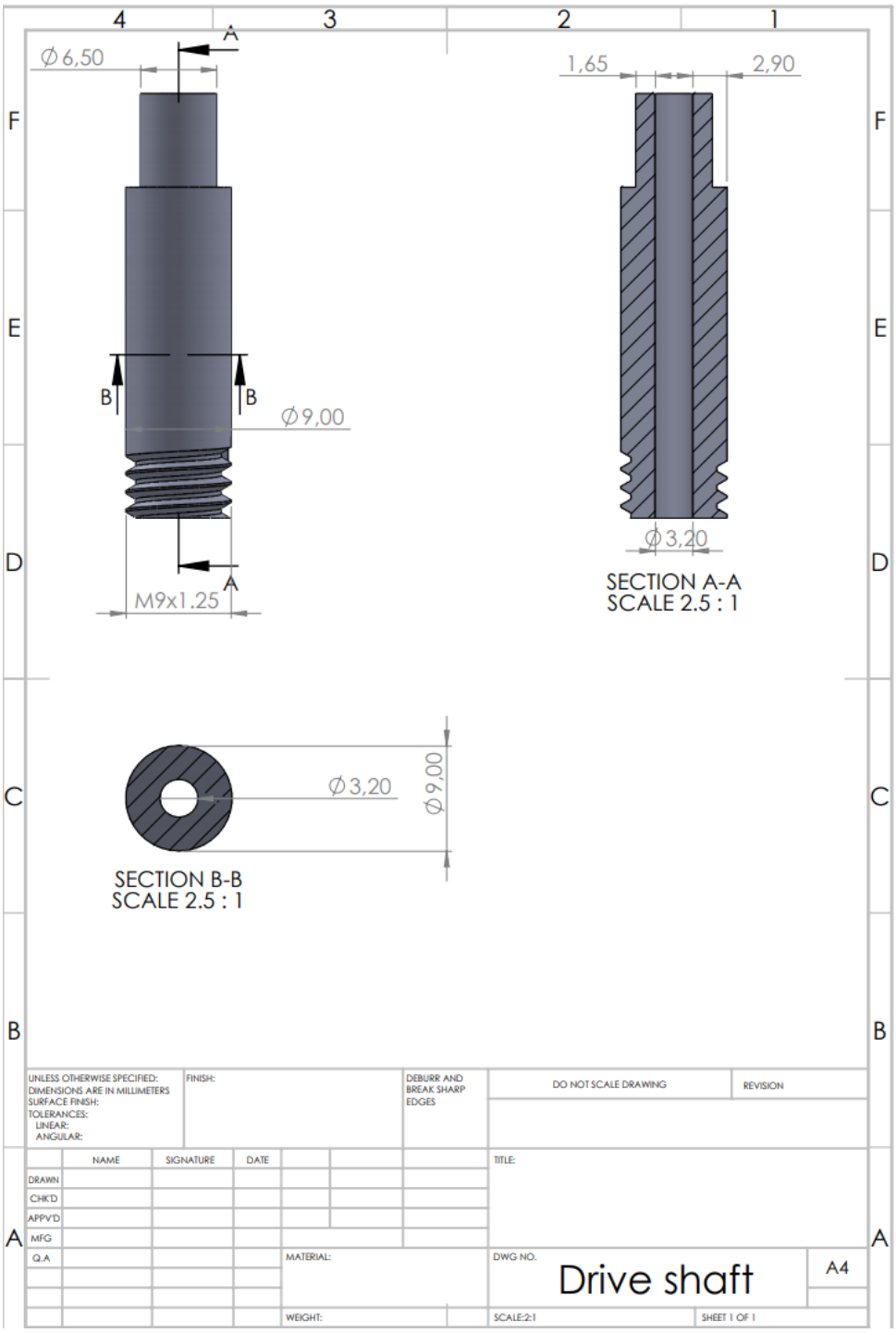

Figure E.6: Drive shaft.

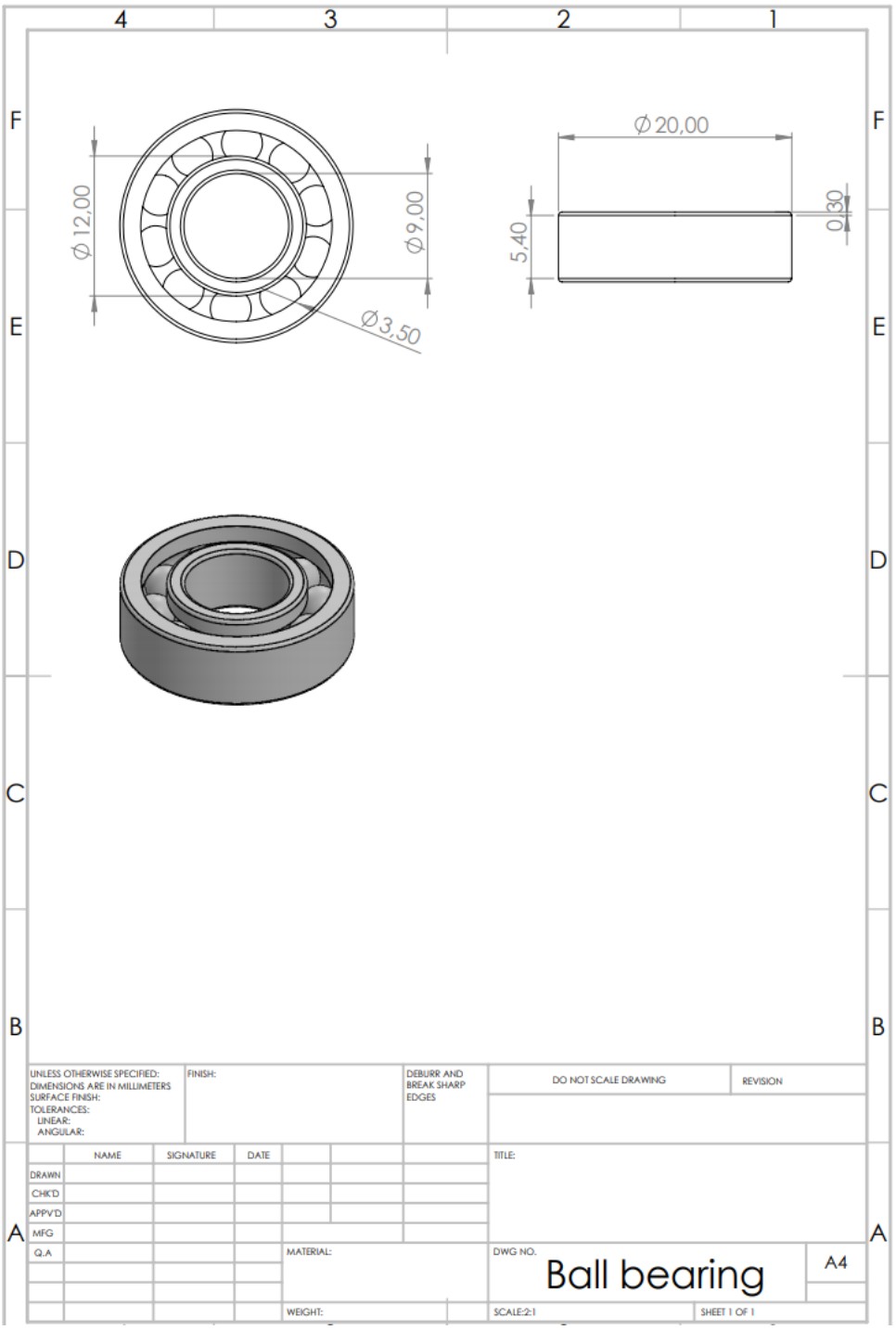

Figure E.7: Ball bearing.

F Hoisting and Top Drive motor Specifications

GST helical gearboxes

Technical data

Dimensions

GST□□-2M VBR

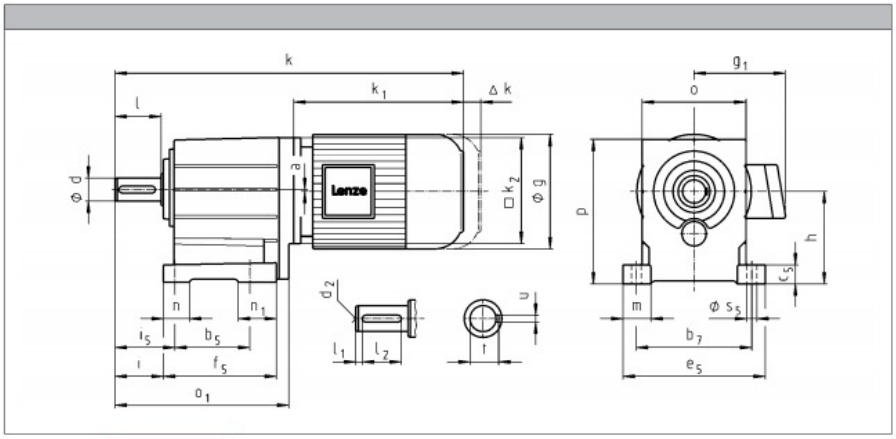

		063C42	071C11	071C13 071C31	071C32	071C33	071C42	080C13 080C33
g		123			139			156
g_1	MDEMAXX MDSMAXX	100			109			150
	MDEMABR MDSMABR	107			118			132
k_1	MDEMAXX MDSMAXX	187			207			224.5
k_2				120				145
Δ k	MDEMABR MDSMABR	40			52			73
	MDFMAXX				128			
	MDFMABR	170			165			183
					k			
GST03		329			349		349	
GST04		371			391			413
GST05		401			421			443
GST06		427			447			469
GST07								525

	a	h[1)]	o[1)]	p[1)]
GST03	2	65	90	101
GST04	0	80	100	132
GST05	1	100	115	158.5
GST06	2	125	145	198
GST07	3	160	180	251

	d k6	d_2	l	l_1	l_2	u	t	i	i_5	o_1	b_5	b_7	c_5	e_5	f_5	m	n	n_1	s_5
GST03	14 20	M5 M6	28 40	4 5	20 28	5 6	16 22.5	34 46	40 52	127 139	60	91	11	105	84	20			6.6
GST04	20	M6	40	5	28	6	22.5	43	53	174	76	105	18	129	112	24.5	20	36	9
GST05	25	M10	50	4	40	8	28	53	66	214	90	125	23	155	139	32.5	26	49	11
GST06	30	M10	60	6	45	8	33	64	79	243	106	160	28	196	157	38	35	52	13.5
GST07	40	M16	80	7	63	12	43	84	104	302	130	200	34	247	196	48.5	45	66	18

Gearbox size		GST03	GST04	GST05	GST06	GST07	GST09	GST11	GST14
Max. torque	[Nm]	45	○ 73	172	375	710	1623	2848	5920
Ratio range		2.6 - 59	1.6 - 45	1.6 - 335	2 - 435	2 - 417	2 - 412	4 - 412	4 - 412
Dimensions									
Solid shaft	[mm]	14 x 28 20 x 40	16 x 32 20 x 40	20 x 40 25 x 50	25 x 50 30 x 60	30 x 60 40 x 80	40 x 80 50 x 100	60 x 120	80 x 160
Flange	[mm]	120 140 160	120 140 160	120 140 160 200	160 200	200 250	250 300	300 350	350 400

Figure F.1: Hoisting and Top Drive motor Specifications[37].

G EMM Specification Chart

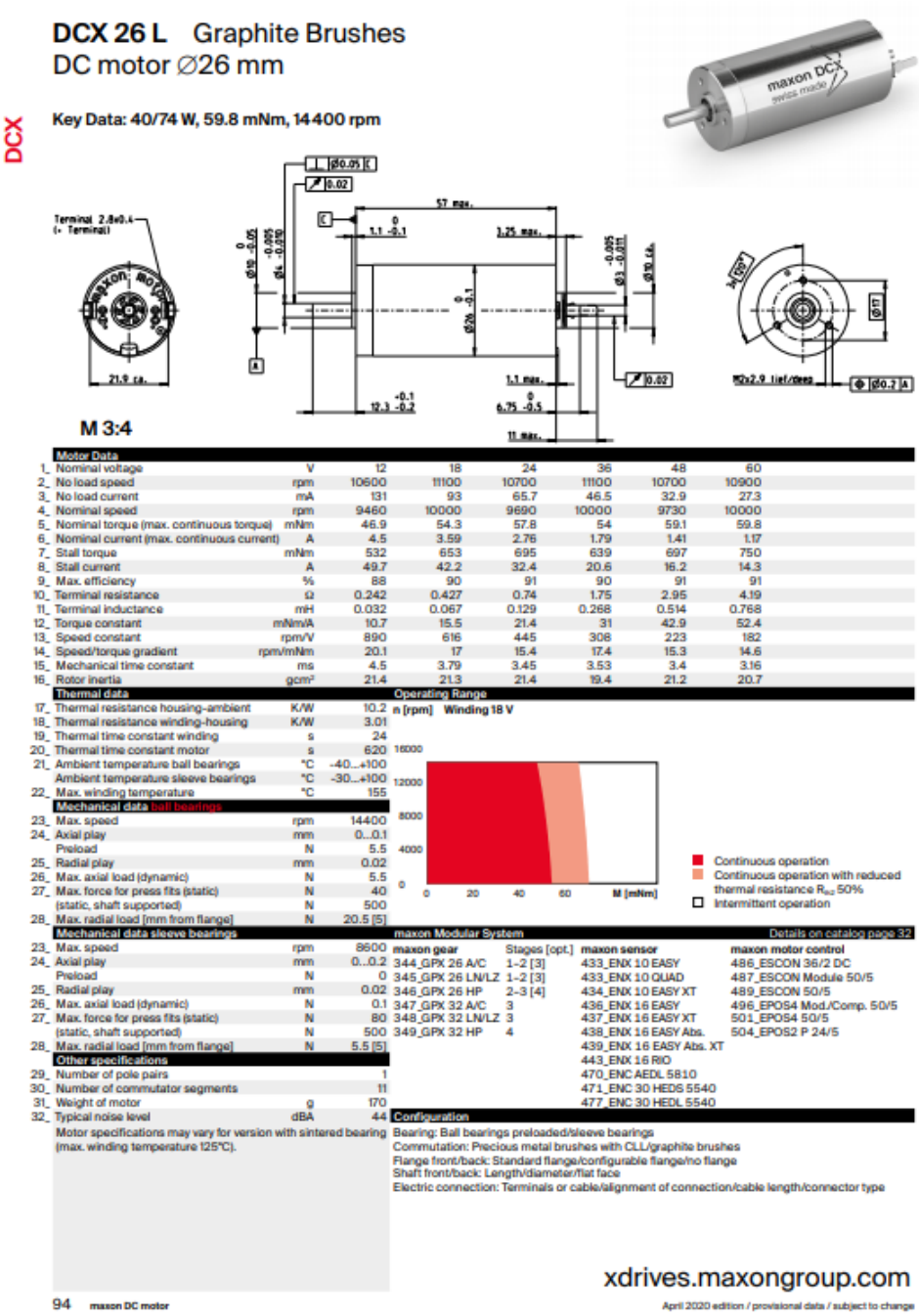

DCX 26 L Graphite Brushes
DC motor ∅26 mm

DCX

Key Data: 40/74 W, 59.8 mNm, 14400 rpm

M 3:4

Motor Data							
1_ Nominal voltage	V	12	18	24	36	48	60
2_ No load speed	rpm	10600	11100	10700	11100	10700	10900
3_ No load current	mA	131	93	65.7	46.5	32.9	27.3
4_ Nominal speed	rpm	9460	10000	9690	10000	9730	10000
5_ Nominal torque (max. continuous torque)	mNm	46.9	54.3	57.8	54	59.1	59.8
6_ Nominal current (max. continuous current)	A	4.5	3.59	2.76	1.79	1.41	1.17
7_ Stall torque	mNm	532	653	695	639	697	750
8_ Stall current	A	49.7	42.2	32.4	20.6	16.2	14.3
9_ Max. efficiency	%	88	90	91	90	91	91
10_ Terminal resistance	Ω	0.242	0.427	0.74	1.75	2.95	4.19
11_ Terminal inductance	mH	0.032	0.067	0.129	0.268	0.514	0.768
12_ Torque constant	mNm/A	10.7	15.5	21.4	31	42.9	52.4
13_ Speed constant	rpm/V	890	616	445	308	223	182
14_ Speed/torque gradient	rpm/mNm	20.1	17	15.4	17.4	15.3	14.6
15_ Mechanical time constant	ms	4.5	3.79	3.45	3.53	3.4	3.16
16_ Rotor inertia	gcm²	21.4	21.3	21.4	19.4	21.2	20.7

Thermal data		
17_ Thermal resistance housing-ambient	K/W	10.2
18_ Thermal resistance winding-housing	K/W	3.01
19_ Thermal time constant winding	s	24
20_ Thermal time constant motor	s	620
21_ Ambient temperature ball bearings	°C	-40...+100
Ambient temperature sleeve bearings	°C	-30...+100
22_ Max. winding temperature	°C	155

Mechanical data ball bearings		
23_ Max. speed	rpm	14400
24_ Axial play	mm	0...0.1
Preload	N	5.5
25_ Radial play	mm	0.02
26_ Max. axial load (dynamic)	N	5.5
27_ Max. force for press fits (static)	N	40
(static, shaft supported)	N	500
28_ Max. radial load [mm from flange]	N	20.5 [5]

Mechanical data sleeve bearings		
23_ Max. speed	rpm	8600
24_ Axial play	mm	0...0.2
Preload	N	0
25_ Radial play	mm	0.02
26_ Max. axial load (dynamic)	N	0.1
27_ Max. force for press fits (static)	N	80
(static, shaft supported)	N	500
28_ Max. radial load [mm from flange]	N	5.5 [5]

Other specifications		
29_ Number of pole pairs		1
30_ Number of commutator segments		11
31_ Weight of motor	g	170
32_ Typical noise level	dBA	44

Motor specifications may vary for version with sintered bearing (max. winding temperature 125°C).

Operating Range

n [rpm] Winding 18 V

Continuous operation
Continuous operation with reduced thermal resistance R_{th2} 50%
Intermittent operation

maxon Modular System Details on catalog page 32

maxon gear	Stages [opt.]	maxon sensor	maxon motor control
344_GPX 26 A/C	1-2 [3]	433_ENX 10 EASY	486_ESCON 36/2 DC
345_GPX 26 LN/LZ	1-2 [3]	433_ENX 10 QUAD	487_ESCON Module 50/5
346_GPX 26 HP	2-3 [4]	434_ENX 10 EASY XT	489_ESCON 50/5
347_GPX 32 A/C	3	436_ENX 16 EASY	496_EPOS4 Mod./Comp. 50/5
348_GPX 32 LN/LZ	3	437_ENX 16 EASY XT	501_EPOS4 50/5
349_GPX 32 HP	4	438_ENX 16 EASY Abs.	504_EPOS2 P 24/5
		439_ENX 16 EASY Abs. XT	
		443_ENX 16 RIO	
		470_ENC AEDL 5810	
		471_ENC 30 HEDS 5540	
		477_ENC 30 HEDL 5540	

Configuration

Bearing: Ball bearings preloaded/sleeve bearings
Commutation: Precious metal brushes with CLL/graphite brushes
Flange front/back: Standard flange/configurable flange/no flange
Shaft front/back: Length/diameter/flat face
Electric connection: Terminals or cable/alignment of connection/cable length/connector type

xdrives.maxongroup.com

94 maxon DC motor

April 2020 edition / provisional data / subject to change

Figure G.1: EMM Specifications [26].

H Azimuth Control Chart

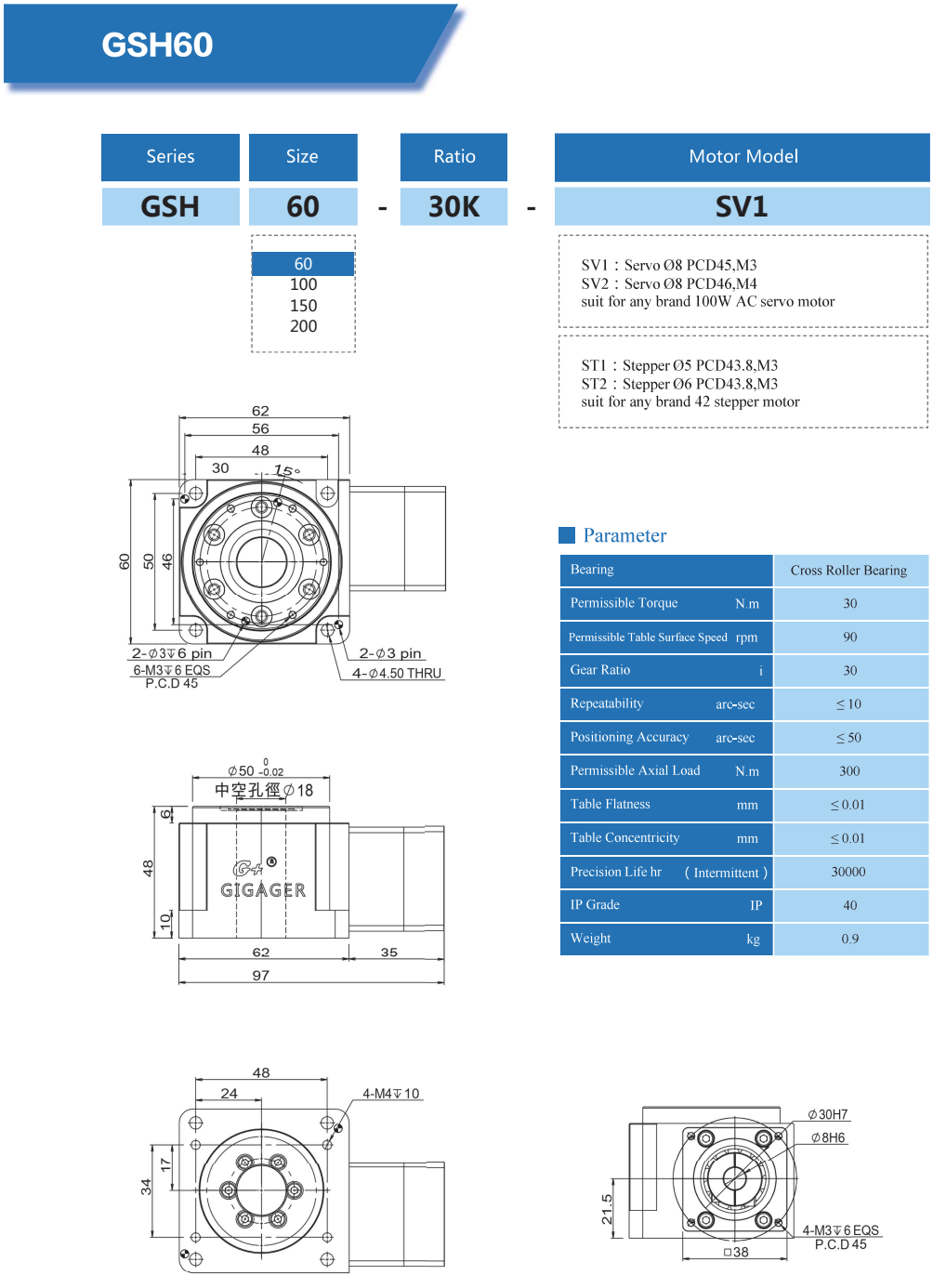

Figure H.1: Hollow shaft gearbox.

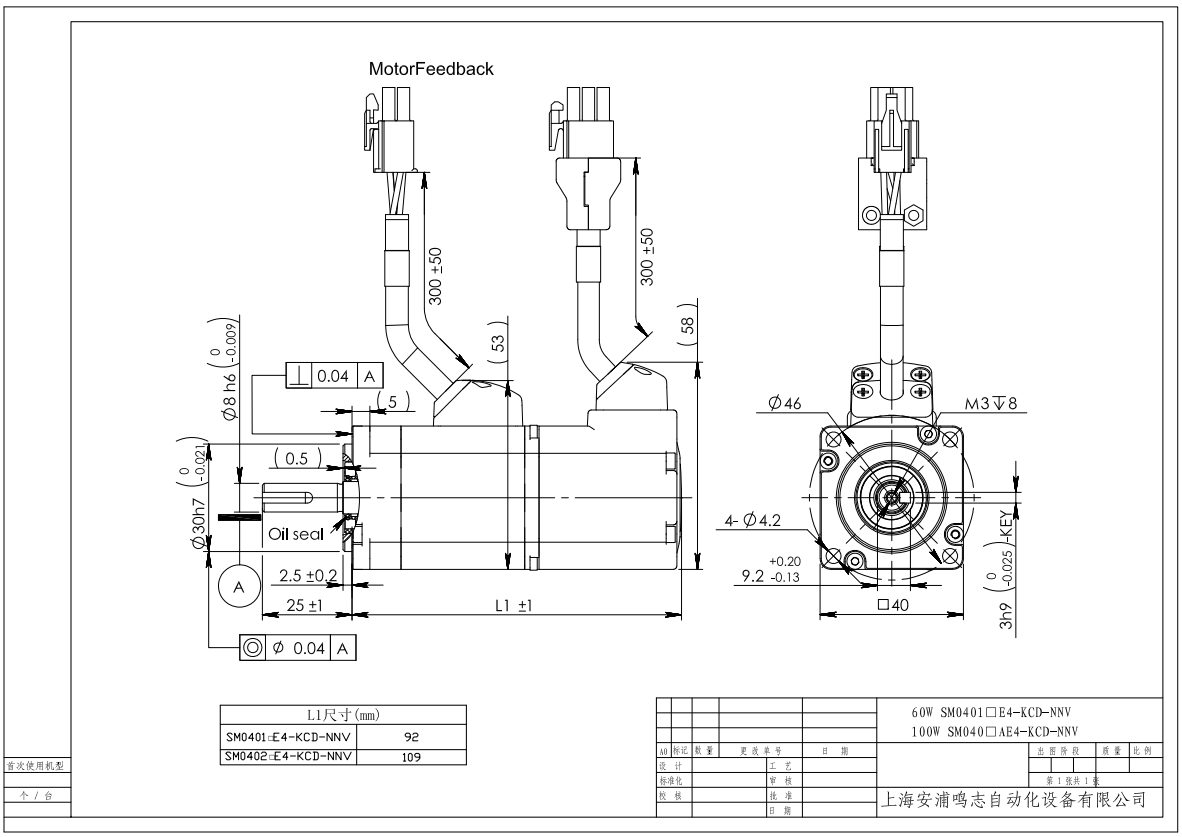

Figure H.2: Azimuth control motor.

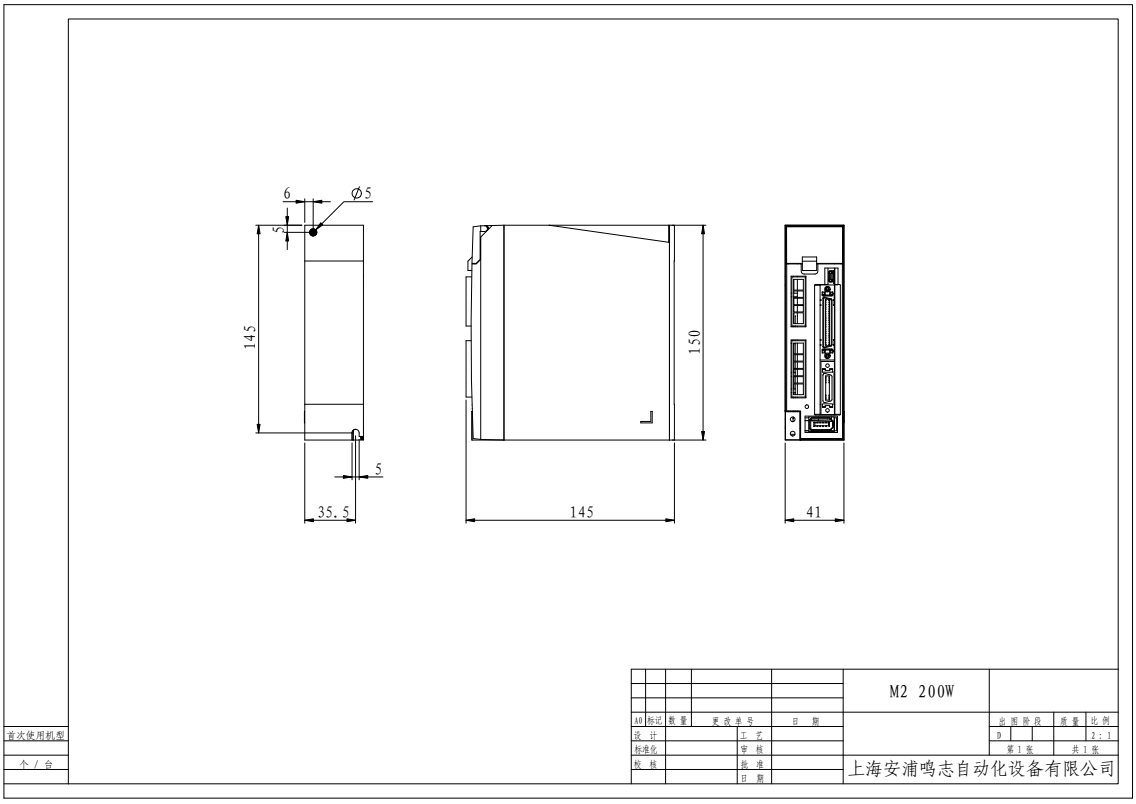

Figure H.3: Azimuth control driver.

NTNU

Norwegian University of
Science and Technology